Constraints on a Minimal Hidden Photon with Kaluza-Klein Excitations in Large Extra Dimensions

ROY, SABYASACHI

Constraints on a Minimal Hidden Photon with Kaluza-Klein Excitations in Large Extra Dimensions

Sabyasachi Roy

A Thesis presented for the degree of
Doctor of Philosophy

Institute for Particle Physics Phenomenology
Department of Physics
University of Durham
England

September 2012

Dedicated to

Bobo and Bunny

Constraints on a Minimal Hidden Photon with Kaluza-Klein Excitations in Large Extra Dimensions

Sabyasachi Roy

Submitted for the degree of Doctor of Philosophy
September 2012

Abstract

The major purpose of this work is to combine the minimal-hidden-photon model with Large Extra Dimensions (LED). This involves confining the Standard-Model photon to a 3-brane, whilst allowing the hidden photon and graviton to occupy the higher-dimensional bulk. After integrating out the extra dimensions both the hidden photon and graviton obtain a tower of massive Kaluza-Klein (KK) modes. The Standard-Model photon obtains no KK modes, in accordance with experiment.

The work begins with a discussion of the minimal hidden photon without KK modes, including the current constraints. In most cases existing constraints are simply quoted or rederived, but for some experiments original constraints are produced. For example new constraints from atomic spectra are produced. Significant modifications are also made to the published constraint from the SN1987a energy-loss experiment. This means properly accounting for the plasma mass of the electron, and also accounting for the modification of the kinetic-mixing parameter in a plasma. Finally constraints are produced for the minimal-hidden-photon model with KK modes.

Declaration

The work in this thesis is based on research carried out at the Institute for Particle Physics Phenomenology, Department of Physics, University of Durham, England.

Aspects of this thesis are based on the following published work:

- Chapter 9.1 is based on Joerg Jaeckel and Sabyasachi Roy, *Spectroscopy as a test of Coulomb's law: A probe of the hidden sector*, Phys. Rev. D **82**, 125020, (2010);
- The argument in Appendix F is based on one by B. Batell and M. Pospelov. This material was previously presented in Joerg Jaeckel and Sabyasachi Roy, *Spectroscopy as a test of Coulomb's law: A probe of the hidden sector*, Phys. Rev. D **82**, 125020, (2010);

The remainder of the research described in this thesis was carried out in collaboration with the author's supervisor Joerg Jaeckel, and also Christopher Wallace.

Unless stated in this declaration or referenced in the text this thesis is all the work of the present author.

No part of this thesis has been submitted for any other degree or qualification.

Acknowledgements

I would like to thank my supervisor Joerg Jaeckel for for his direction, tuition, and most of all tolerance.

I would like to thank Chris Wallace for his contribution to the present work and for proofreading my thesis.

I would like to thank office mates for invaluable support in academic and practical matters, particularly Daniele Galloni (who also provided excellent proofreading), and Mark Rodgers.

Finally I would like to thank the people at Trevelyan College, who were very good to me during my admittedly brief visits.

This work was funded by an STFC studentship.

Contents

List of Figures

List of Tables

1 Introduction

The Standard Model (SM) of particle physics has been extremely successful. For example it describes three known fundamental forces (quantum chromodynamics, electromagnetism, and the weak force), explains particle masses through the Higgs mechanism, makes Fermi's weak force renormalizable by introducing the proper mediating gauge bosons (W^+, W^- and Z), and successfully predicts the anomalous magnetic moment of the electron to an extremely high precision.

However there exist problems with the SM. For example it does not incorporate the fourth known force of gravity, contains no acceptable dark-matter candidate, and inaccurately predicts the anomalous magnetic moment of the muon. There also exists a large difference between the electroweak and Planck scales (the so-called hierarchy problem).

Particle physics is now generally concerned with trying to understand and rectify these problems, constructing new theories which attempt to be more fundamental and complete. These are generally referred to as Beyond-the-Standard-Model (BSM) theories.

One such approach extends spacetime itself to encompass so-called "extra dimensions", in an attempt to solve the hierarchy problem. For example the paradigm of Large Extra Dimensions (LED) purports that the large 4-dimensional Planck mass M_{pl} is not the true Planck mass. The true higher-dimensional Planck mass M_* is in fact much smaller, and close to the electroweak scale. The large M_{pl} is in fact an effective parameter, made to look large because of the large volume of extra dimensions [1, 2] (see Chapter 3.2).

Another common BSM strategy is to extend the SM gauge group of $SU(3) \times SU(2) \times U(1)$. The simplest such modification is to multiply by another $U(1)$. This is often suggested from a top-down perspective, as many string compactifications predict additional gauge symmetries, in particular $U(1)$ factors. However independent of this top-down motivation it is possible to envisage other scenarios in which there exist undiscovered gauge factors. This is phenomenologically allowed, as long as these extra gauge factors interact with the SM feebly enough to have avoided detection. Such extra gauge factors could explain observed phenomena that is not commensurate with the SM. For example in certain regions of parameter space a hidden $U(1)$ could function as a dark-

matter candidate [3], and in Chapter 10.1.1 it is shown that the hidden $U(1)$ could explain the discrepancy between the SM prediction for the anomalous magnetic moment and the experimentally-observed value [4].

This work considers a particular combination of both varieties of extension. The extension of gauge group is simply the multiplication by a hidden-$U(1)$ factor, which supplies the model with a hidden photon. It is further assumed that extra dimensions are present, specifically Large Extra Dimensions (LED) (see Chapter 3.2). The graviton and hidden photon are allowed to propagate through these extra dimensions, resulting in a tower of Kaluza-Klein (KK) modes for both particles. The model is essentially a toy one, and hence simple assumptions are generally made. For example it is assumed that the hidden photon is the only hidden-sector particle. That is, other gauge factors or matter content are not considered. This is denoted the "minimal" hidden-photon model. Furthermore several simple geometrical assumptions are made (see Chapter 4.1).

The central aim of this thesis is to use data from current experiments to produce constraints for the hidden-photon model which includes KK modes.

1.1 Thesis outline

Chapter 2 outlines the minimal-hidden-photon model without KK modes, including current experimental constraints. Chapter 3 briefly reviews the paradigm of extra dimensions before expounding the particular choice of extra-dimensional paradigm, which is that of Large Extra Dimensions (LED). Chapter 4 combines the minimal-hidden-photon model with LED, which results in a tower of KK modes for the hidden photon and graviton. Chapter 5 demonstrates how to derive constraints for the hidden-photon KK model. Chapter 6 considers problems which could be caused by ultraviolet (UV) divergences. Chapter 7 discusses the effective perturbative parameter, which is crucial in the case of virtual production. Chapter 8 shows how to properly account for hidden-photon reabsorption through scattering or decay and how this results in an upper boundary for constraints. Chapters 9 - 16 consider constraints for the hidden photon, first for the non-KK model and then for the KK model. The work concludes in Chapter 17.

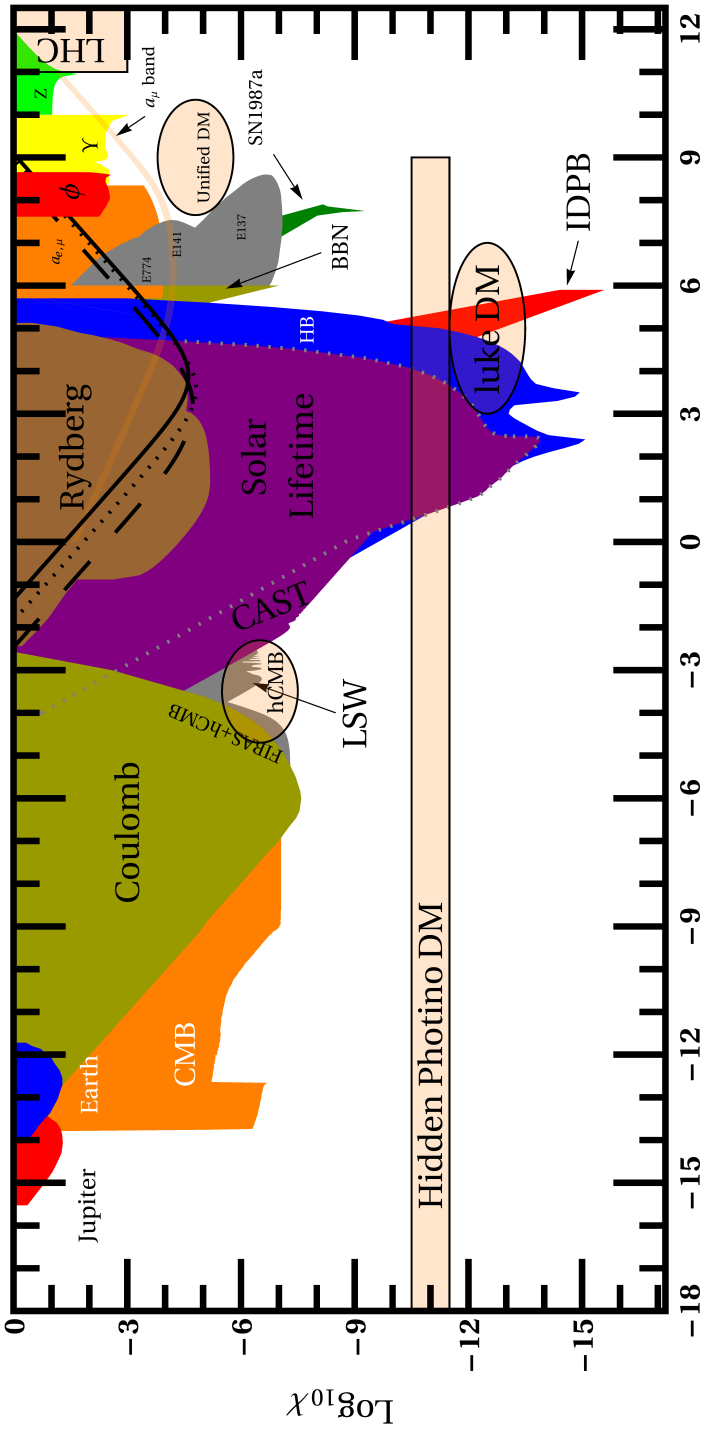

Figure 1: Summary plot of the current constraints on the hidden photon without KK modes (compilation adapted from [5–8]). See the text for details.

2 The hidden photon

A generic feature of BSM theories is the prediction of new particles. For example a pseudoscalar particle named the axion has been proposed to solve the Strong CP problem [9]. Many theories predict minicharged particles (MCPs), which are essentially particles with very small electric charges [10–12].[1] This work is specifically concerned with the hidden photon, which is the particle associated with a hidden-sector $U(1)$.

2.1 The low-energy-effective hidden-photon Lagrangian

This section discusses the generic low-energy-effective Lagrangian for the hidden photon. From a top-down perspective this is generally obtained by integrating out higher-energy degrees of freedom. Alternatively it is possible to envisage some other scenario in which the hidden photon is present at lower energies. Either way this effective Lagrangian is given by [15, 16]

$$\mathcal{L} = -\frac{1}{4}F_{\mu\nu}F^{\mu\nu} - \frac{1}{4}X_{\mu\nu}X^{\mu\nu} + \frac{1}{2}\cos^2\chi\, m_X^2\, X_\mu X^\mu - \frac{1}{2}\sin\chi F_{\mu\nu}\, X^{\mu\nu}, \quad (2.1)$$

where $F_{\mu\nu} = \partial_\mu A_\nu - \partial_\nu A_\mu$ is the SM-photon field strength, $X_{\mu\nu} = \partial_\mu X_\nu - \partial_\nu X_\mu$ is the hidden-photon field strengths, m_X is the hidden-photon mass, and χ is the "kinetic-mixing" coupling constant.

The final term is allowed because both $F_{\mu\nu}$ and $X_{\mu\nu}$ are individually gauge invariant. It connects the SM and hidden sectors via the kinetic-mixing parameter χ. This mixing term is the source of extra physical effects predicted by the hidden-photon model. The kinetic-mixing parameter χ has a mass dimension of zero and therefore is a renormalizable coupling. This means that it is not suppressed by any higher-mass scales and should be observable at lower energies, even if it is very small.

Fundamental high-energy theories may make specific predictions for the parameters m_X, χ. For example string theories predict values in the range

[1] Several of the hidden-photon constraints are actually modifications to constraints for other BSM particles. For example the atomic-spectral constraints in Chapter 9 use a method originally constructed to constrain MCPs [13], and SN1987a energy-loss constraints were first produced for axions [14].

$10^{-12} \lesssim \chi \lesssim 10^{-3}$ [17–19]. However from the point of view of low-energy-effective theory, χ and m_X are simply free parameters. The only restriction is that, for a given m_X, χ must be small enough to be consistent with current experimental non observation of the hidden photon.

The non-zero mass m_X is necessary for the theory to be consequential. If the hidden photon was massless then it would be physically indistinguishable from the SM photon. The theory would therefore have no experimentally-measurable effects. On the other hand if $m_X \to \infty$ then the hidden photon becomes impossible to excite, and ceases to be an effective physical degree of freedom. Therefore there are only non-trivial physical effects for intermediate values of m_X. In Chapter 9.1.1 this is shown specifically for the Coulomb potential. However this is a general feature of the hidden-photon effect in all experiments, and can be seen from the constraints in Figure 1. These all die off in the limits $m_X \to 0$ and $m_X \to \infty$, and are strongest in the region $m_X \sim E$, where E is the energy scale of the given experiment.

2.2 Hidden-photon oscillations

This section discusses the key phenomena of SM-photon $\longleftrightarrow$ hidden-photon oscillations. Like neutrino oscillations, this is caused by a misalignment between the interaction and propagation eigenstates.

The fields (A, X) appearing in the Lagrangian Equation (2.1) are not interaction eigenstates, because of the kinetic-mixing term. It is often useful to transform to the basis of interaction eigenstates, (A_I, X_I), where the kinetic-mixing term is absent. X_I is physically decoupled from the SM photon A_I and therefore has no interactions with the SM. The elimination of the kinetic-mixing term is achieved by the definitions [20]

$$A_I = \cos\chi A, \quad X_I = X - \sin\chi A. \tag{2.2}$$

The Lagrangian now becomes

$$\begin{aligned}\mathcal{L} &= -\frac{1}{4}F_{\mu\nu}F^{\mu\nu} - \frac{1}{4}\left(X_{I\mu\nu} + \sin\chi F_{\mu\nu}\right)\left(X_I^{\mu\nu} + \sin\chi F^{\mu\nu}\right) \\ &\quad + \frac{\sin\chi}{2}\big(X^I_{\mu\nu} + \sin\chi F_{\mu\nu}\big)F^{\mu\nu} + \frac{\cos^2\chi}{2}m_X^2\big(X^I_\mu + \sin\chi A_\mu\big)\big(X_I^\mu + \sin\chi A^\mu\big) \\ &= -\frac{1}{4}F^I_{\mu\nu}F_I^{\mu\nu} - \frac{1}{4}X^I_{\mu\nu}X_I^{\mu\nu} + \frac{1}{2}m_X^2\big(\cos\chi X^I_\mu - \sin\chi A^I_\mu\big)\big(\cos\chi X_I^\mu - \sin\chi A_I^\mu\big)\,. \end{aligned} \tag{2.3}$$

There are now non-diagonal mass terms. Hence the interaction eigenstates are not propagation eigenstates. The propagation eigenstates are obtained by transforming to a new basis [20]

$$\begin{pmatrix} A_P \\ X_P \end{pmatrix} = U \begin{pmatrix} A_I \\ X_I \end{pmatrix} , \tag{2.4}$$

where the orthogonal matrix

$$U = \begin{pmatrix} \cos\chi & -\sin\chi \\ \sin\chi & \cos\chi \end{pmatrix} \tag{2.5}$$

diagonalises the mass squared matrix. The propagation eigenstate X_P has mass m_X, and the propagation eigenstate A_P is massless.

It is possible to assume without loss of generality that a SM-photon interaction eigenstate A_I is produced at $t = 0$ and $z = 0$, and travels in the z direction. It then propagates as a linear combination of the two propagation eigenstates

$$\begin{aligned} A_I(t,z) &= \cos\chi\, A_P\, e^{i\omega(t-z)} + \sin\chi\, X_P\, e^{i\left(\omega t - k_{X_P} z\right)} \\ &= e^{i\omega(t-z)} \left(\cos\chi\, A_P + \sin\chi\, X_P\, e^{i\left(\omega - k_{X_P}\right)z}\right) , \end{aligned} \tag{2.6}$$

where $m_{A_P} = 0$ has been used to set $k_{A_P} = \omega$.

There is now a non-zero probability for oscillations into an X_I at (t, z);

$$P_{A_I \to X_I} = |\langle X_I | A_I(t,z)\rangle|^2 = 4\sin^2\chi\cos^2\chi\sin^2\left(\frac{(\omega - k_{X_P})z}{2}\right). \tag{2.7}$$

These oscillations have key observable effects in many experiments.

For example in light-shining-through-a-wall experiments (LSW) [19, 21–25, 25–27] the SM photon is able to oscillate into a hidden photon, which can then oscillate into an experimentally-detectable SM photon on the other side of the wall.

Furthermore in Chapter 12.2 it is shown that a plasma environment modifies these oscillations. This results in a modified effective kinetic mixing χ_{eff} (see Equation (12.13)), which dies off in the limit $m_X \to 0$ and is maximised at the resonance peak $m_X = m_\gamma$. This strongly affects astrophysical and cosmological constraints.

2.3 Current constraints in the non-KK model

This section briefly describes the experiments used for obtaining constraints, referring to the summary plot for the non-KK model (Figure 1).

- "Jupiter", "Earth" constraints:
  The hidden photon causes perturbations to the predictions of Maxwell's laws. These can be searched for in the planetary magnetic fields of Earth and Jupiter [28], leading to constraints. The large length scales involved translate into small-mass scales $m_X \sim (10^{-15} - 10^{-12})$ eV.

- "CMB" (Cosmic-Microwave-Background) constraints:
  The hidden photon contributes a positive effective neutrino number [29, 30]. However CMB, large-scale structure (LSS) and supernova (SN) data combined suggests an effective neutrino number slightly less than 3, $N_\nu^{eff} = 2.9^{-1.4}_{+2.0}$ [31]. The hidden photon is therefore inconsistent with these observations and must have a suitably small abundance, which produces the constraint.

- "Coulomb" constraints:
  In similar fashion to the "Jupiter", "Earth" constraints, these involves a modification to the electromagnetic force. In the static limit there is a Yukawa-like perturbation to the standard Coulomb potential (see Equation (9.1)). A Cavendish-type experiment tests the Yukawa-like perturbation [32] by searching for a potential difference between a charged outer sphere and uncharged inner sphere. Non-observation of this potential difference results in a constraint. The experiment occurs at length scales of around 1 metre, which translates into mass scales $m_X \sim 0.1$ μeV.

- "LSW" (light-shining-through-a-wall) constraints:
  These experiments [19, 21–25, 25–27] operate on a simple principle. A produced SM photon can oscillate into a hidden photon, which can traverse a macroscopic physical boundary and then oscillate into an experimentally-detectable SM photon on the other side. A constraint is obtained by imposing that the predicted hidden-photon signal is larger than the ex-

perimental background of SM-photon events.[2]

- "Solar-lifetime" constraints:
  Solar hidden photons can escape from the sun and contribute to energy loss. If this energy loss is too large (around equal to that caused by SM photons) then it becomes impossible to construct a solar model which allows the sun to survive to the present day [33–35]. In Chapter 12.2 the published constraint [35] for the non-KK model is rederived, and in Chapter 12.3 constraints for the KK model are produced.

- "CAST" (CERN-Axion-Solar-Telescope) constraints:
  Solar hidden photons can oscillate into SM photons and be detected by CAST. A constraint is obtained by imposing that the hidden-photon effect is larger than the experimental background [35]. In Chapter 13.2 the published non-KK constraint is rederived, and in Chapter 13.3 constraints for the KK model are produced.

- Atomic-spectral constraints:
  This is another test of the Yukawa-like perturbation to the Coulomb potential (see Equation (9.1)), this time using atomic spectra. The length scales involved are much smaller than those in the lab experiments of the "Coulomb" constraints, and this translates to a much larger-mass scale $m_X \sim 10$ keV. The brown region labelled "Rydberg" is the combined set of constraints arising from measurements of the Rydberg constant [7,8,36]. In Chapter 9.1 original constraints for the non-KK model are derived, and these are shown as the black lines in Figure 1. The black-dashed line is from the Lamb shift in atomic hydrogen. The black-dotted line is a combined constraint from the $1\,s_{1/2} - 2\,s_{1/2}$ and $2\,s_{1/2} - 8\,s_{1/2}$ transitions in atomic hydrogen. The solid-black line is the constraint obtained from the Lamb shift in hydrogen-like helium ions. In Chapter 9.2 it will be shown that no KK-model constraints can be produced from atomic spectra, or

[2]The very similar "laser-polarization" experiments are currently being conducted. The basic idea is that virtual production of hidden photons can cause a polarization-dependent refractive index (dichroism). This results in a phase shift of linearly-polarised light, turning it into elliptically-polarised light [6]. Lack of observation of this phase shift produces a constraint.

from any virtual-production experiments (see Chapter 6).

- "HB" (Horizontal Branch) lifetime constraints:
  These are similar to the solar-lifetime constraints, but this time the astrophysical object is a HB star [3]. The temperature scales are around an order of magnitude larger than in the sun, and this leads to constraints at slightly larger masses. The densities are also a couple of orders of magnitude larger so hidden-photon production is more efficient, and the constraint is slightly stronger. In Chapter 14.1 the published non-KK constraint is rederived, and in Chapter 14.2 constraints for the KK model are produced.

- "BBN" (Big-Bang-Nucleosynthesis) constraints:
  The hidden photon can cause distortions to predictions of BBN [3, 37]. These constraints only cover a small region of parameter space in the non-KK model, and would produce very weak constraints in the KK model. The BBN constraint is therefore not treated in detail.

- "IDPB" (Intergalactic-Diffuse-Photon-Background) constraints:
  Hidden photons produced in the early universe can survive to the present day. Decay emits SM photons, which contribute to the current IDPB. A constraint is imposed by imposing that the hidden-photon contribution is larger than the experimental value [3]. In Chapter 15.1 the published constraints for non-KK model are rederived, and in Chapter 15.2 constraints for KK model are produced.

- "$a_{e,\mu}$" constraints:
  Here $a = (g-2)/2$, where $(g-2)$ is the anomalous magnetic moment of a particle. The hidden photon causes a deviation to the anomalous magnetic moment for each particle. A constraint is obtained by imposing that this deviation is larger than the "uncertainty" associated with this quantity [4]. This "uncertainty" parametrises the current lack of knowledge of the quantity, and is essentially the combination of both experimental and theoretical errors (see Equation (9.5)). In Chapter 10.1 the published constraints for the non-KK model are rederived. Hidden-photon production is virtual and, similarly to the atomic spectral case (see Chapter 9.2),

constraints for the KK model are not produced (see Chapter 10.2).

- Fixed-target constraints "E137", "E141", "E774":
  The fixed-target experiments involve firing an electron beam at a thick target, causing hidden photons to be emitted through bremsstrahlung. The hidden photon then has to pass through a shielding wall, before decaying to a detectable e^+e^- pair. Imposing that the number of these events is larger than the observed background constrains the hidden photon [38].[3] In Chapter 11.1 the published constraints for the non-KK model are rederived, and in Chapter 11.2 constraints for the KK model are produced.

- "SN1987a" constraints:
  Hidden photons produced in the supernova can escape and contribute to energy loss. If this effect is too large then the supernova cools too quickly and the observed extended neutrino burst of $\sim 5-10$ seconds can not occur, constraining the hidden photon [14,38]. In Chapter 16.1 constraints for the non-KK model are derived, and in Chapter 16.2 constraints for the KK model are produced.

- "Υ"-decay constraints:
  This is a collider experiment. The data is taken from the BABAR search [42], where an electron beam and positron beam are collided. The products include an Υ meson ($b\bar{b}$). This can decay to $\gamma + X$, with the subsequent decay of $X \to \mu^+ + \mu^-$. The detected signal is $\gamma + \mu^+ + \mu^-$. A constraint is obtained by imposing that the predicted hidden-photon effect is larger than the observed background.

  There exist non-KK constraints from other collider experiments, for example those from ϕ decay at DAΦNE [43].

  In the KK model no significant constraints are obtained from collider experiments. This is simply because colliders detect the hidden photon by searching for a narrow resonance peak. In the KK model the total hidden-

[3] Recently new fixed-target constraints have been constructed from past electron beam dump experiments at KEK [39, 40] and Orsay [40, 41]. However these only penetrate a small sliver of extra parameter space, and therefore are not explicitly considered in this work.

photon effect is given by summation over hidden-photon KK modes, which have masses which are generally quite closely spaced (see Chapter 5). Hence any resonance peak from the non-KK model is smoothed out in the KK model, the hidden-photon effect is undetectable, and no constraints are obtained. Collider experiments are therefore not treated in detail.

- "Z"-boson-mass constraints:

  The hidden photon causes a tree level modification to the Z-boson mass. A constraint is obtained by imposing that this modification is greater than the current uncertainty in the Z-boson mass [44]. This is a virtual-production experiment (see Chapter 6), so no constraints are obtained in the KK model (see Chapters 9.2 and 10.2). Therefore Z-boson-mass constraints are not treated in detail.

The central aim of this thesis is to produce constraints for the hidden-photon KK model. These KK modes have a minimum mass scale of ~ 10 meV, which is imposed by table-top constraints [45, 46] (see Chapter 3.2.1). There are several constraints which occur at hidden-photon mass scales smaller than that of the lowest possible KK mode, and hence no KK modes can be excited within them. Hence these experiments do not produce constraints in the KK model, and not treated in detail. Specifically these are the "Earth", "Jupiter", "CMB", "Coulomb", and "LSW" experiments.

The orange translucent regions in Figure 1 are not actually constraints. These are regions in which the hidden photon could explain observed phenomena [19]. For example in the "lukeDM" region the hidden photon could function as lukewarm dark matter [3], in the region "UnifiedDM" the hidden photon can act as a mediator to GeV-scale hidden-sector dark matter [47, 48], and in the "Hidden Photino DM" region the SUSY partner to the hidden photon could function as dark matter [49]. In the region "hCMB", the hidden photon could be used to provide the early universe with a larger effective number of neutrinos, which would in turn explain data from the Sloan Digital Sky Survey and Lyman-alpha forests [50, 51]. In Chapter 10.1.1 the "a_μ band" is derived. In this region the hidden photon could explain the discrepancy between the SM prediction for a_μ and the experimental value [4].

2.4 Summary of Chapter 2

The minimal-hidden-photon model is a BSM model with a hidden-$U(1)$ factor. It is "minimal" because there is only a single hidden gauge factor and no hidden matter content. This model has practical applications.

The low-energy-effective Lagrangian is generically given by Equation (2.1). There are two new parameters in this model; the hidden-photon mass m_X, and the kinetic-mixing parameter χ. Hidden-photon effects disappear in the limits $m_X \to 0$ and $m_X \to \infty$, and are strongest in the region $m_X \sim E$, where E is the energy scale of a given experiment.

The interaction and propagation eigenstates of this model are misaligned, with leads to SM-photon $\longleftrightarrow$ hidden-photon oscillations. This causes key observable effects in many experiments.

3 Extra dimensions

The essential idea here is that spacetime is extended to include more dimensions. When observing from a low-energy perspective these extra dimensions are effectively integrated out. This results in particles obtaining a tower of Kaluza-Klein (KK) modes.

In order to observe the physical effects of the KK modes for non-SM particles, these KK modes must have masses $\lesssim 1$ TeV. However for agreement with current data SM particles must have masses $\gtrsim 1$ TeV, or perhaps have no KK modes at all. Therefore there must be a fundamental difference between SM and non-SM particles. More specifically there must be some fundamental difference in the way that SM and non-SM particles experience the spacetime geometry.

3.1 The braneworld paradigm

This situation can be realised within the "braneworld" paradigm, which originates from string theory. Here there exists a D-dimensional "bulk", with lower-dimensional sub-surfaces called "branes" [52].

In the original string theory formulation SM particles are represented by open strings and can only travel along dimensions longitudinal to the brane. Gravitons are represented by closed strings and can travel along dimensions both transverse and longitudinal to the brane, and are therefore free to travel throughout the bulk.

This work does not use string theory, but rather an effective field theory inspired by the braneworld scenario. Here particles are no longer represented by strings. However the essential braneworld features are applied by hand. SM particles are confined to the brane and gravitons can propagate throughout the bulk. The model contains another non-SM particle, the hidden photon, which is allowed to travel throughout the bulk.

The desired asymmetry between SM and non-SM particles has now been obtained. These two categories of particle experience the spacetime geometry differently and have different KK modes.

The non-SM particles alone travel through the transverse dimensions. It is therefore possible to allow some or all of these dimensions to be large $\gtrsim 1/\text{TeV}$.

When these larger dimensions are integrated the non-SM particles obtain KK modes with masses $\lesssim 1$ TeV, which can be tested using current data.

SM particles are now confined to the longitudinal dimensions. If some of the longitudinal dimensions are extra dimensions then these must be small $\lesssim 1/\text{TeV}$. When these are integrated out the SM particles obtain KK modes with masses $\gtrsim 1$ TeV, which do not conflict with current data.

This work only considers experimental data with mass scales $\lesssim 1$ TeV, so these longitudinal extra dimensions actually leave no significant signature. It is therefore just simpler to assume that longitudinal extra dimensions do not exist. Hence it is imposed that all extra extra dimensions are transverse to the brane. The brane is now the observable $(3+1)$-dimensional world.

3.2 Large Extra Dimensions (LED)

The model uses a particular example of the braneworld paradigm; Large Extra Dimensions (LED) [1, 2].[4]

This model is inspired by one observation: that the gravitational force is much weaker than SM forces. This results in extremely weak constraints on the gravitational force. It is therefore possible to have graviton KK modes with masses $\lesssim 1$ TeV, which are compatible with current experimental data. This makes it physically possible to have so-called "large" extra dimensions, with sizes $\gtrsim 1/\text{TeV}$.

The LED attempts to solve the hierarchy problem by claiming that M_{pl} is only an effective 4-dimensional Planck scale. It is related to the true higher-dimensional Planck scale M_* by the extra-dimensional volume [1, 2]. This relation can be straightforwardly derived by considering the Einstein-Hilbert action. In 4 dimensions this is given by

$$S = \frac{M_{pl}^2}{2} \int R\sqrt{-g}\, d^4x\,, \tag{3.1}$$

where R is the Ricci scalar and g is the determinant of the metric tensor. The

[4] An alternative braneworld scenario is that of warped extra dimensions [53, 54]. In this scenario the electroweak scale is suppressed relative to the Planck scale by an exponential "warping factor", which is dependent on the extra-dimensional curvature and radius. McDonald and Morrissey [55] derive constraints on a hidden-$U(1)$ factor in this scenario.

full extra-dimensional action is given by generalising this,

$$S = \frac{M_*^{2+n}}{2} \int R\sqrt{-g}\, d^4x\, d^n y\,, \tag{3.2}$$

where $\vec{y}$ are the extra-dimensional coordinates. Integrating out the extra dimensions therefore produces the conditions

$$M_{pl}^2 = M_*^{2+n}\, V_E\,, \tag{3.3}$$

where V_E is the extra-dimensional volume. If V_E is large enough then M_* can be reduced significantly, putting in anywhere in the region $1\,\text{TeV} \lesssim M_* \lesssim M_{pl}$ [56].

The extra-dimensional geometry is weakly constrained, so there is a large range of possible geometries. However this is a toy model, so it is appropriate to assume a simple geometrical configuration. This is chosen to be a toroidal compactification where all extra dimensions have the same radius R_T. Hence $V_E = (2\pi R_T)^n$, where n is the number of extra dimensions.

3.2.1 Constraints on extra-dimensional mass parameters

Gravitons can propagate through transverse extra dimensions, resulting in a tower of massive KK modes for the graviton (this will be discussed further in Chapter 4.1.2). Each massive KK mode causes a Yukawa-like modification to the gravitational potential.[5] Considering just the contribution for the lowest mass KK graviton mode, [45, 46]

$$V(r) = -\frac{G\, m_1 m_2}{r}\left(1 + \frac{8n}{3} e^{-\frac{r}{R_T}}\right), \qquad r \gtrsim R_T\,, \tag{3.4}$$

where R_T gives the length scale of deviation.[6]

Hoyle et al. provide the most recent table-top constraints [46], and find no perturbation to Newton's Law at the 95 % confidence level. R_T is therefore constrained as follows. The magnitude of the perturbative term has to be much smaller than the magnitude of the original potential, in order to agree with

[5] In very similar fashion the massive hidden photon causes a Yukawa-like modification to the Coulomb potential (see Chapter 9.1).

[6] In the region $r \lesssim R_T$ the gravitational potential should once again follow a power law, but this time in the full higher-dimensional space; $V(r) \sim 1/r^{n+1}$. However experiments have not reached the length scale r at which the power-law potential is observable. Hence it is possible just to use Equation (3.4).

n	m	M_*
1	> 10 meV	$> 2 \times 10^5$ TeV
2	> 10 meV	> 2 TeV
3	> 0.35 keV	> 1 TeV
4	> 0.13 MeV	> 1 TeV
5	> 4.4 MeV	> 1 TeV
6	> 47 MeV	> 1 TeV

Table 1: Allowed values of the mass parameters m and M_* for different numbers of extra dimensions n. m is both the mass of the lowest KK mode and the mass separation of KK modes. M_* is the proper higher-dimensional Planck scale. For $n = 1, 2$ the effective lower limit comes from the parameter m. For $n = 3, ..., 6$ the effective lower limit comes from the higher-dimensional Planck scale M_* [56]. Constraints only need to be produced for allowed values of m.

non observation of deviation to the inverse square law. Hence the exponential term must be small. Therefore $r \gtrsim R_T$ for all probed value of r. With this approach [46] rules out $R_T \gtrsim 2 \times 10^{-4}$ metres at the 95% confidence level. Therefore the KK-mass parameter is limited to the region $m \gtrsim 10$ meV.

Note that, because of the factor $8n/3$, the constraints on R_T are actually weakly dependent on n. However this dependence is logarithmic and only a small range of $1 \leq n \leq 6$ is considered. Hence this effect is extremely small and can be neglected to a good approximation.

A lower limit for M_* can also be imposed. This must be $\gtrsim 1$ TeV to agree with current experimental data. This lower limit is rather coarse, with a precision of around an order of magnitude.

Hence there is a lower limit for each of the mass parameters m, M_*. However these parameters are not independent, but are linked through the relation in Equation (3.3). Therefore for each value of n only one of these lower limits is effective. This is shown in Table 1.

For $n = 1, 2$ it is the lower limit for m which is effective, and the allowed values of M_* are actually pushed up from the lower limit of 1 TeV. For $n = 2$,

M_* is only pushed up by a factor of 2. This is inconsequential as a factor of 2 is well within the precision of the original lower limit for M_*. However in the case of $n = 1$, M_* is pushed up by around five orders of magnitude. This could cause difficulties with respect to the hierarchy problem, as M_* is now around five orders of magnitude larger than the electroweak scale. However this work is mainly concerned with hidden-photon constraints and not strongly concerned with the hierarchy problem, so this does not cause any serious difficulty.

For $n = 3, ..., 6$ the lower limit for M_* is effective, and the allowed values of m are pushed up above the lower limit for m of 10 meV. This is physically consequential as constraints are only obtained for these larger values of m.

3.3 Summary of Chapter 3

This chapter discusses the paradigm of extra dimensions. At the most basic level this is the extension of spacetime to include more than the currently-observed $(3 + 1)$ dimensions. When observing from a low-energy perspective the extra dimensions are effectively integrated out. This results in particles obtaining a tower of KK modes.

The model uses a "braneworld" scenario, specifically that of Large Extra Dimensions (LED). All SM particles are confined to the brane, and do not obtain KK modes. Non-SM particles, specifically the graviton and hidden photon, are allowed to travel throughout the bulk. These particles do obtain KK modes.

The model is a toy one, therefore it is appropriate to assume a simple configuration for the bulk geometry. The brane corresponds to the observable $(3+1)$-dimensional world, and all extra dimensions are transverse to the brane. Furthermore it is assumed that all extra dimensions are of equal length, and are toroidally compactified.

There are two extra-dimensional mass parameters m and M_*, where m is the KK-mass parameter, and M_* is the proper higher-dimensional Planck mass. An upper limit is obtained on the extra-dimensional size R_T from table-top experiments [45, 46], and this translates to a limit $m \gtrsim 10$ meV. A lower limit of $M_* \gtrsim 1$ TeV is imposed, for fit with current experimental data [56]. However the parameters m and M_* are not independent, but are linked through Equation (3.3). Therefore, for any n, only of of these two lower limits is effective. The

allowed values of m and M_* for each n are shown in Table 1.

4 Hidden photons in Large Extra Dimensions

This chapter combines the minimal-hidden-photon model with LED. In this scenario the hidden-photon KK modes automatically become massive, and therefore physically observable. The masses in this scenario emerge naturally from the geometry, without the need for an additional Higgs or Stueckelberg mass term. This work does not consider such an additional Higgs or Stueckelberg mass term. However this is an obvious possibility for further work. That scenario would have two mass parameters as well as the kinetic-mixing parameter, and the corresponding constraints would be in a three-dimensional parameter space.

4.1 Derivation of KK modes

Integrating out the extra dimensions produces a tower of KK modes for the hidden photon and graviton.

It will be shown that this process also creates new scalar particles. However these are completely physically decoupled.

4.1.1 The KK model without gravitation

It is simpler to first consider the minimal-hidden-photon model without gravitation, and then introduce gravitation at a later stage. The gravitation-less Lagrangian is effectively 0^{th}-order in the gravitational coupling $1/M_{pl}$. The effects of gravitation will be included later by expanding the Lagrangian to 1^{st} order in $1/M_{pl}$.

Without extra dimensions or gravitation the minimal-hidden-photon Lagrangian is given by

$$\mathcal{L} = -\frac{1}{4}F_{\mu\nu}F^{\mu\nu} - \frac{1}{4}X_{\mu\nu}X^{\mu\nu} - \frac{\sin\chi}{2}F_{\mu\nu}X^{\mu\nu}. \tag{4.1}$$

This Lagrangian is extended to n extra dimensions in the following way,

$$\mathcal{L} = -\frac{1}{4}\hat{F}_{\mu\nu}\hat{F}^{\mu\nu}\delta(\vec{y}-\vec{y}_{SM}) - \frac{1}{4}\hat{X}_{MN}\hat{X}^{MN} - \frac{\sin\chi}{2}\hat{F}_{\mu\nu}\hat{X}^{\mu\nu}\delta(\vec{y}-\vec{y}_{SM}), \tag{4.2}$$

where higher-dimensional fields are written with a hat ($\hat{}$) superscript. The bulk coordinates are $x^M = (x^\mu, y^a)$, with $\mu = 0,1,2,3$, $a = 1,2,.....n$. Note

that the SM-photon gauge field is dependent only on the brane coordinates ($A^\nu = A^\nu(x^\mu)$), but the hidden-photon gauge field is dependent on the full bulk coordinates ($X^N = X^N(x^M)$).

The SM brane is located at y_{SM} in the extra dimensions, and can in general be a dynamical coordinate. However it will be found that the low-energy Lagrangian is actually independent of this coordinate, and therefore that the theory is not sensitive to any higher-energy brane dynamics.

There are two separate physical assumptions in the extended Lagrangian Equation (4.2). The first one is empirically justified, whereas the second is model dependent.

The first physical assumption imposes that the SM photon is trapped on the brane. This is the source of the $\delta(\vec{y} - \vec{y}_{SM})$ factor which accompanies each SM contribution in the Lagrangian Equation (4.2). The justification for this is that SM particles are not observed to have KK modes at currently-accessible energies, and therefore the theory must not predict such KK modes. Therefore the SM photon has no Fourier mode expansion, and the gauge field is a function of the brane coordinates only. Furthermore the SM-photon gauge field components along the extra-dimensional directions are zero; $A_a = 0$, which implies $F_{\mu a} = 0$ and $F_{aa} = 0$. Note that the last equality is also true by the antisymmetry of the field tensor.

Overall this means that the higher-dimensional contractions $F_{MN}F^{MN}$ and $F_{MN}X^{MN}$ collapse to $F_{\mu\nu}F^{\mu\nu}$ and $F_{\mu\nu}X^{\mu\nu}$, which are the factors written in Equation (4.2). The hidden photon field is allowed to have non-zero components along the extra dimensions, so $X_a \not\equiv 0$, and $X_{ab} \not\equiv 0$ for $a \neq b$. Hence the full contraction $X_{MN}X^{MN}$ is used.

The higher-dimensional SM-photon gauge field is then given by

$$\hat{A}_M(x^\mu) = \left(\frac{m}{2\pi}\right)^{\frac{n}{2}} A_\mu(x^\mu)\,, \tag{4.3}$$

where the appropriate normalisation factors are included.

To understand the second assumption it should be noted that the presence of the SM brane actually breaks the higher-dimensional Lorentz invariance. Therefore the most general form of the higher-dimensional hidden-photon kinetic term

is actually given by

$$\begin{aligned}\mathcal{L} \quad =& -\frac{1}{4}\left(c_1\hat{X}_{\mu\nu}\hat{X}^{\mu\nu} + c_2\hat{X}_{ab}\hat{X}^{ab} + 2\sqrt{c_1c_2}\hat{X}_{\mu a}\hat{X}^{\mu a}\right) \\ & -\frac{1}{4}\left(d_1\hat{X}_{\mu\nu}\hat{X}^{\mu\nu} + d_2\hat{X}_{ab}\hat{X}^{ab} + 2\sqrt{d_1d_2}\hat{X}_{\mu a}\hat{X}^{\mu a}\right)\delta\left(\vec{y}-\vec{y}_{SM}\right) . \quad (4.4)\end{aligned}$$

The term with coefficients c_i, $i = 1, 2, 3$ are the ordinary hidden-photon kinetic terms, now modified to include possible Lorentz-invariance. The terms with coefficients d_i, $i = 1, 2, 3$ now also include the possibility of the hidden photon being localised to the brane. The third assumption of Equation (4.2) is therefore that the Lorentz-breaking and brane localising terms for the hidden photon are negligibly small, that is $c_1 \gg c_2, c_3, d_i$, and $c_1 \sim 1$. This is not a strongly justified assumption and is therefore model dependent. Further work should explore the cases when these extra terms are non-negligible.

It is now necessary to completely specify the bulk geometry. Simple geometrical configurations are assumed, as is appropriate for a toy model. For example it is assumed that the longitudinal and transverse dimensions can be separately factorised

$$M_{\text{bulk}} = M_{\text{longitudinal}} \times M_{\text{transverse}} . \quad (4.5)$$

The longitudinal dimensions are now equivalent to the visible (3+1)-dimensional world. At 0^{th}-order in $1/M_{pl}$ this is simply the Minkowski manifold M_4. The extra dimensions are now transverse to the brane.

It is further assumed that the geometry of each extra dimension is itself factorisable, and that each extra dimension is compactified on a circle. Overall,

$$M_{\text{bulk}} = M_4 \times S_1 \times S_2 \times ....S_n . \quad (4.6)$$

The bulk geometry is now completely specified, and is depicted in Figures 2 and 3.

With these assumptions the higher-dimensional hidden-photon field $\hat{X}_M$ is decomposed as[7]

$$\hat{X}_M(x^\mu, y^a) = \left(\frac{m}{2\pi}\right)^{\frac{n}{2}} \sum_{\vec{k}} X_M^{(\vec{k})}(x^\mu)\, e^{im\vec{k}\cdot(\vec{y}-\vec{y}_{SM})} , \quad (4.7)$$

[7] This method is largely taken from [59].

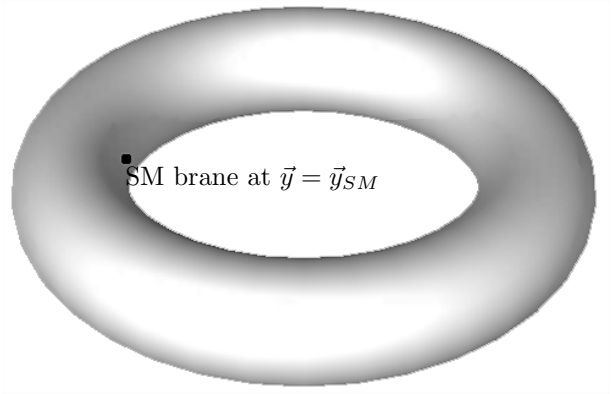

Figure 2: A sketch of the bulk geometry which emphasises the extra dimensions. The extra dimensions a compactified to form a n-dimensional torus with $n = 1, ..., 6$, although in this figure the depicted torus is only 2 dimensional. The $(3 + 1)$-dimensional SM brane is located at $\vec{y} = \vec{y}_{SM}$, where $\vec{y}$ are the extra-dimensional position coordinates, and is depicted in the figure by the dot. The SM photon is confined to the SM brane at $\vec{y} = \vec{y}_{SM}$, whereas the hidden photon and graviton are free to propagate throughout the whole bulk. The figure is modified slightly from the one in [57].

where

$$\sum_{\vec{k}} = \prod_{i=1}^{n} \sum_{\vec{k_i}} . \tag{4.8}$$

In 4 dimensions the hidden photon comes from a $U(1)$ gauge boson, and is represented by a real field. This reality condition must be respected by all Fourier modes, so

$$\left[X_M^{(\vec{k})}(x^\mu)\right]^\dagger = X_M^{(\vec{k})}(x^\mu) . \tag{4.9}$$

It is appropriate to preserve this reality condition in the higher-dimensional extension. This produces the condition

$$\begin{aligned} & \left[\hat{X}_M(x^\mu, y^a)\right]^\dagger && = \hat{X}_M(x^\mu, y^a) , \\ \rightarrow \quad & \left[X_M^{(\vec{k})}(x^\mu)\right]^\dagger && = X_M^{(-\vec{k})}(x^\mu) , \\ \rightarrow \quad & X_M^{(\vec{k})}(x^\mu) && = X_M^{(-\vec{k})}(x^\mu) , \end{aligned} \tag{4.10}$$

where the orthogonality of the Fourier modes and reality condition of Equation (4.9) have been used.

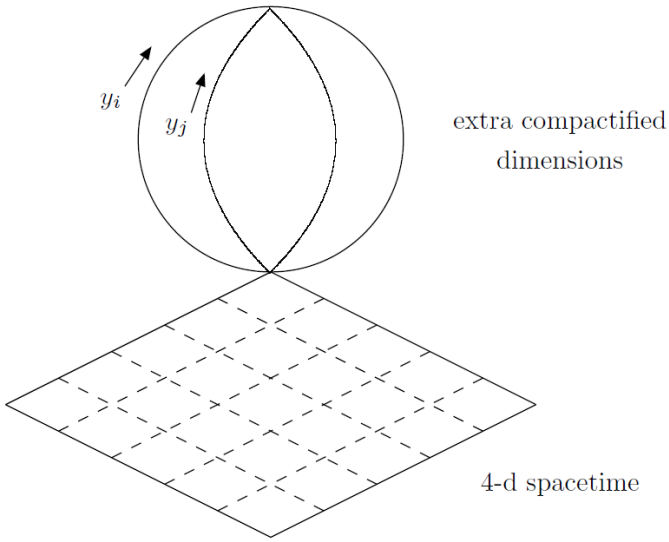

Figure 3: A sketch of the bulk geometry of the model. Dimensions longitudinal to the brane correspond to the observable 4-dimensional world. Extra dimensions are transverse to the brane and are given co-ordinates y^i, y^j etc., with i, j $= 1, ..., 6$. The SM photon is confined to the SM brane at $\vec{y} = \vec{y}_{SM}$, whereas the hidden photon and graviton are free to propagate throughout the whole bulk. The figure is taken from [58].

The 4-dimensional effective Lagrangian is now obtained by integrating out the extra dimensions. It is easiest to do this by considering each term in Equation (4.2) separately.

The hidden-photon kinetic term goes as

$$\hat{X}_{MN}\hat{X}^{MN} = \hat{X}_{\rho\sigma}\hat{X}^{\rho\sigma} + 2\hat{X}_{\rho a}\hat{X}^{\rho a} + \hat{X}_{ab}\,\hat{X}^{ab}\,, \tag{4.11}$$

where the antisymmetry of the field tensor has been used.

The Fourier expansion of the first term is

$$\left(\frac{m}{2\pi}\right)^n \sum_{\vec{k}}\sum_{\vec{l}} \left(\partial_\rho X_\sigma^{(\vec{k})}\partial^\rho X^{\sigma(\vec{l})} - \partial_\rho X_\sigma^{(\vec{k})}\partial^\sigma X^{\rho(\vec{l})}\right) e^{im(\vec{k}+\vec{l})\cdot(\vec{y}-\vec{y}_{SM})}\,. \tag{4.12}$$

Integrating this over $\int_0^{2\pi/m} d^n y$ gives

$$\sum_{\vec{k}} X_{\rho\sigma}^{(-\vec{k})} X^{\rho\sigma(\vec{k})} = \sum_{\vec{k}} X_{\rho\sigma}^{(\vec{k})} X^{\rho\sigma(\vec{k})}\,, \tag{4.13}$$

where the orthogonality of Fourier modes and the reality condition from Equation (4.10) have been used. The process of integrating out the extra dimensions has imposed conservation of KK number. This conservation will be broken for terms which include the $\delta(\vec{y}-\vec{y}_{SM})$ factor.

The second hidden-photon kinetic term from Equation (4.11) $\sim \hat{X}_{\rho a}\hat{X}^{\rho a}$. In 4 dimensions the fields $X_a^{(\vec{k})}$ become scalars, because a is not a 4-dimensional index. To emphasise this the notation replacement $X_a^{(\vec{k})} \to S_a^{(\vec{k})}$ is made,

$$\int_0^{\frac{2\pi}{m}} d^n y \left(\partial_\rho \hat{S}_a - \partial_a \hat{X}_\rho\right)\left(\partial^\rho \hat{S}^a - \partial^a \hat{X}^\rho\right)$$

$$= \sum_{\vec{k}} \left(\partial_\rho S_a^{(\vec{k})} - imk_a X_\rho^{(\vec{k})}\right)\left(\partial^\rho S^{a\,(\vec{k})} - imk^a X^{\rho\,(\vec{k})}\right)$$

$$= \sum_{\vec{k}} \Bigg(\underbrace{\partial_\rho S_a^{(\vec{k})} \partial^\rho S^{a\,(\vec{k})}}_{\text{scalar kinetic terms}} + \underbrace{-2imk_a X_\rho^{(\vec{k})} \partial^\rho\ S^{a\,(\vec{k})}}_{\text{interaction terms}} + \underbrace{-m^2 k^2 X_\rho^{(\vec{k})} X^{\rho\,(\vec{k})}}_{\text{gauge field mass terms}} \Bigg) . \quad (4.14)$$

Naïvely the second term implies interactions between scalars and hidden photons. For $\vec{k} = \vec{0}$ this term is zero and it is obvious that no such interaction exists.

However for $\vec{k} \neq \vec{0}$ it is still possible to perform a gauge transformation which leaves the field tensor $X_{\mu\nu}^{(\vec{k}=\vec{0})}$ invariant,

$$X_\rho^{(\vec{k}\neq\vec{0})} \to X_\rho^{(\vec{k}\neq\vec{0})} - \sum_{a=1}^{n} \frac{ik_a}{mk^2} \partial_\rho S_a^{(\vec{k}\neq\vec{0})}. \quad (4.15)$$

This is the unitary gauge, where the physical degrees of freedom are manifest. Using this it is possible to set

$$\sum_{a=1}^{n} k_a\, S^{a\,(\vec{k}\neq\vec{0})} = 0\,. \quad (4.16)$$

The linear combination of scalar fields $\sum_{a=1}^{n} k_a\, S^{a\,(\vec{k}\neq\vec{0})}$ has been eaten by a Higgs-type mechanism. Therefore one degree of freedom has disappeared from the collection of scalar fields, and now goes towards making the gauge fields $X_\mu^{(\vec{k}\neq 0)}$ massive.

It can be confirmed that the physical degrees of freedom add up.[8] First recall the reality conditions which are imposed on all scalar and vector particles (Equation (4.10)).

[8] This discussion is based on the one in [58].

Scalar particles have one component, which is itself physical.

A general massless gauge field P^M has D components. However not all of these are physical, as it is still necessary to account for gauge fixing. First it is possible to pick a particular gauge, which reduces the number of independent components by 1. Without loss of generality the Lorentz gauge

$$\partial_M P^M = 0 \tag{4.17}$$

can be chosen. Furthermore it is possible to perform the gauge transformation

$$P_M \to P_M - \partial_M \phi \tag{4.18}$$

for a real scalar ϕ, under which the field tensor is unchanged.[9] This gauge transformation removes another component, so overall there are $(D-2)$ physical degrees of freedom.

However if the gauge field is massive, the mass term $(1/2)\, m_P^2 P_M P^M$ is not invariant under the shift in Equation (4.18). Hence no such gauge transformation exists, and this component is not lost. A massive gauge field therefore has $(D-1)$ physical degrees of freedom overall.

It is now possible to check that the process of integrating out preserves the physical degrees of freedom of the higher-dimensional hidden photon. Before dimensional reduction, each massless Fourier mode has $(D-2) = (2+n)$ degrees of freedom. After integrating out, the cases $\vec{k} \neq \vec{0}$ and $\vec{k} = \vec{0}$ are slightly different.

For $\vec{k} \neq \vec{0}$ the gauge fields $X_\mu^{(\vec{k}\neq\vec{0})}$ eat the linear combination of scalar fields $\sum_{a=1}^{n} k_a S^{a(\vec{k}\neq\vec{0})}$ and become massive. The gauge fields now have 3 physical degrees of freedom, and there are $(n-1)$ uneaten scalar degrees of freedom left over. The total number of physical degrees of freedom is $3 + (n-1) = (2+n)$ as before.

For $\vec{k} = \vec{0}$ the gauge fields $X_\mu^{(\vec{k}=\vec{0})}$ remain massless, and the n scalars $S_a^{(\vec{k}=\vec{0})}$ remain uneaten, so there are $(2+n)$ physical degrees of freedom overall. Hence physical degrees of freedom are conserved.

[9] Note that Equations (4.17) and (4.18) together produce the condition $\partial^2 \phi = 0$.

In the unitary gauge of Equation (4.15) it is therefore possible to write

$$\begin{aligned}&\int_0^{\frac{2\pi}{m}} d^n y \left(\partial_\rho \hat{X}_a - \partial_a \hat{X}_\rho\right)\left(\partial^\rho \hat{X}^a - \partial^a \hat{X}^\rho\right)\\ = &\sum_{\vec{k}} \left(\underbrace{\partial_\rho S_a^{(\vec{k})} \partial^\rho S^{a\,(\vec{k})}}_{\text{scalar kinetic terms}} + \underbrace{-m^2 k^2 X_\rho^{(\vec{k})} X^{\rho\,(\vec{k})}}_{\text{gauge field mass terms}} \right). \end{aligned} \tag{4.19}$$

This form shows both the kinetic terms for the scalar fields, and the mass terms for the gauge fields. The apparent interaction terms have disappeared. This is physically important as it demonstrates that there are no decays from the hidden photon to the scalar particles.

The final hidden-photon Lagrangian term from Equation (4.11) is $\hat{X}_{ab}\hat{X}^{ab} = \hat{S}_{ab}\,\hat{S}^{ab}$. Integrating this out gives

$$\begin{aligned}&\int_0^{\frac{2\pi}{m}} d^n y \left(\partial_a \hat{S}_b - \partial_b \hat{S}_a\right)\left(\partial^a \hat{S}^b - \partial^b \hat{S}^a\right)\\ = &\sum_{\vec{k}} (-m^2) \left(k_a S_b^{(\vec{k})} - k_b S_a^{(\vec{k})}\right)\left(k^a S^{b\,(\vec{k})} - k^b S^{a\,(\vec{k})}\right)\\ = &\sum_{\vec{k}\neq\vec{0}} (-2\,m^2) \left(k^2 S_a^{(\vec{k})} S^{a\,(\vec{k})} - \left(k_a S^{a\,(\vec{k})}\right)^2\right), \end{aligned} \tag{4.20}$$

where in the third line it has been emphasised that there is no contribution for $\vec{k} = \vec{0}$. This is a non-diagonal mass matrix. The physical states are the mass eigenstates. These can be found by rewriting the mass matrix of Equation (4.20) as an eigenvalue equation [60],

$$\sum_{b=1}^{n} \left(k^2 \delta_{ab} - k_a k_b\right) v^b = \lambda v_a\,, \tag{4.21}$$

where the eigenvectors v_a are the mass eigenstates.

By inspection there is one zero eigenvalue, corresponding to $v_a = k_a$. This is precisely the linear combination of scalar fields $\sum_{a=1}^{n} k_a S_a$ which is eaten by the Higgs-type mechanism. Again by inspection, there are solutions with eigenvalue $\lambda = k^2$. This requires $\sum_{a=1}^{n} k_a v^a = 0$, for which there are $(n-1)$ linearly-independent eigenvectors. Therefore for any $\vec{k} \neq \vec{0}$ there is one massless scalar (which is eaten by the Higgs-type mechanism), and $(n-1)$ scalars of mass $k^2 m^2$.

Overall, the scalar Lagrangian for $\vec{k} = \vec{0}$ is given by

$$\sum_{a=1}^{n} \frac{1}{2} \partial_\mu S_a^{(\vec{k}=\vec{0})} \partial^\mu S^{a\,(\vec{k}=\vec{0})}\,, \tag{4.22}$$

and the scalar Lagrangian for $\vec{k} \neq \vec{0}$ can be rewritten in the mass-eigenstate basis as

$$= \sum_{\vec{k}\neq\vec{0}} \sum_{a=1}^{(n-1)} \frac{1}{2}\partial_\mu S_a^{(\vec{k}\neq\vec{0})} \partial^\mu S^{a\,(\vec{k}\neq\vec{0})} + \frac{1}{2} m^2 k^2 S_a^{(\vec{k}\neq\vec{0})} S^{a\,(\vec{k}\neq\vec{0})}\,, \tag{4.23}$$

where the eaten massless scalars are no longer present.

It has already been shown that there are no two body decays of the form $X \to S$, because the corresponding Lagrangian term disappears. It is further shown in Chapter 4.1.2 that there are no decays which involve only KK particles, as this is disallowed by KK-number conservation. Hence there are no decays involving the scalars, for example those of the form $X \to S+G$. It can further be observed that these scalars have no interactions, and are effectively physically decoupled. These scalars will therefore be ignored for the remainder of this work.

Integrating out the kinetic-mixing term in Equation (4.2) gives

$$\begin{aligned} & \int_0^{\frac{2\pi}{m}} d^n y \left(-\frac{\sin\chi}{2}\right) \hat{F}_{\mu\nu}\hat{X}^{\mu\nu}\,\delta(\vec{y}-\vec{y}_{SM}) \\ = & \int_0^{\frac{2\pi}{m}} d^n y \left(-\frac{\sin\chi}{2}\right) \left(\frac{m}{2\pi}\right)^n F_{\mu\nu} \sum_{\vec{k}} X^{\mu\nu(\vec{k})} e^{im\vec{k}\cdot(\vec{y}-\vec{y}_{SM})}\,\delta(\vec{y}-\vec{y}_{SM}) \\ = & -\frac{\sin\chi}{2} F_{\mu\nu} \sum_{\vec{k}} X^{\mu\nu(\vec{k})}. \end{aligned} \tag{4.24}$$

The SM photon therefore couples to all hidden-photon KK modes. Moreover it does so with the same coupling strength ($\sin\chi$).

Overall the effective 4-dimensional Lagrangian without gravitation is

$$\mathcal{L} = -\frac{1}{4}F_{\mu\nu}F^{\mu\nu} + \sum_{\vec{k}}\left(-\frac{1}{4}X^{(\vec{k})}_{\mu\nu}X^{\mu\nu}_{(\vec{k})} + \frac{1}{2}k^2 m^2 X^{(\vec{k})}_{\mu} X^{\mu}_{(\vec{k})}\right) + \sum_{\vec{k}} -\frac{\sin\chi}{2} F^{\mu\nu} X^{(\vec{k})}_{\mu\nu}\,. \tag{4.25}$$

4.1.2 The KK model with gravitation

After integrating out the extra dimensions, the graviton obtains a tower of massive KK modes in a very similar way to the hidden photon [61].

The Lagrangian for interaction between gravitation and the SM is given by [61]

$$\mathcal{L} = -\frac{1}{2\,M_{pl}} \sum_{\vec{k}} \left(G^{(\vec{k})}_{\mu\nu} T^{\mu\nu} + \sqrt{\frac{2}{3\,(n+2)}}\,\phi^{(\vec{k})}\,T^{\mu}{}_{\mu} \right)\,. \tag{4.26}$$

where $G_{\mu\nu}$ is the graviton field. It couples to the energy-momentum tensor of the SM.

ϕ is the "dilaton" field. This is essentially a scalar particle which is obtained by integrating out the higher-dimensional graviton field. It couples to the trace of the energy-momentum tensor of the SM. When the higher-dimensional hidden-photon field is integrated out extra scalar particles are also obtained (see Chapter 4.1.1), but the scalars associated with the hidden photon are physically decoupled from observable physics. However the dilaton field is physically coupled to SM fields, as can be seen from Equation (4.26).

The dilaton is coupled with the same strength coupling as the graviton (to leading order $1/M_{pl}$). Therefore the dilaton and graviton have similar strength interactions. This section proceeds by only considering graviton interactions. It will eventually be shown in Chapter 8.2.2 that interactions involving the graviton are highly suppressed and therefore always negligible. Therefore the effects of the dilaton are always negligible as well. Without the dilaton particle, the Lagrangian for interaction between gravitation and the SM is given by

$$\mathcal{L} = -\frac{1}{2\,M_{pl}} \sum_{\vec{k}} G_{\mu\nu}^{(\vec{k})} T^{\mu\nu} \,. \tag{4.27}$$

The energy-momentum tensor is generally given by

$$T_{\mu\nu} = \left(-\eta_{\mu\nu}\mathcal{L} + 2\frac{\delta\mathcal{L}}{\delta g^{\mu\nu}} \right) \Big|_{g=\eta} \,. \tag{4.28}$$

For the SM photon

$$\begin{aligned} \mathcal{L} &= -\frac{1}{4} F_{\alpha\beta} F_{\rho\sigma} g^{\rho\alpha} g^{\sigma\beta} \,, \\ \longrightarrow \frac{\delta L}{\delta g^{\mu\nu}} &= -\frac{1}{4} F_{\alpha\beta} F_{\rho\sigma} (\delta^{\rho}_{\mu}\delta^{\alpha}_{\nu} g^{\sigma\beta} + \delta^{\sigma}_{\mu}\delta^{\beta}_{\nu} g^{\rho\alpha}) \\ &= -\frac{1}{4} (F_{\nu}{}^{\sigma} F_{\mu\sigma} + F^{\rho}{}_{\nu} F_{\rho\mu}) \\ &= -\frac{1}{2} F_{\mu\sigma} F_{\nu}{}^{\sigma} \,, \end{aligned} \tag{4.29}$$

where in the last step the antisymmmetry of the field tensor has been used. Hence the energy-momentum tensor for the SM photon is given by

$$T_{\mu\nu} = \frac{1}{4} \eta_{\mu\nu} F_{\rho\sigma} F^{\rho\sigma} - \frac{1}{2} F_{\mu\sigma} F_{\nu}{}^{\sigma} \,. \tag{4.30}$$

Therefore the interaction Lagrangian between the graviton and the SM photon is given by

$$\sum_{\vec{k}} \frac{-1}{\sqrt{2}M_{pl}} G^{\mu\nu}(\vec{k}) \left(\frac{1}{4}\eta_{\mu\nu} F_{\rho\sigma}F^{\rho\sigma} - \frac{1}{2} F_{\mu\sigma}F_{\nu}{}^{\sigma} \right) . \tag{4.31}$$

It is possible to generalise Equation (4.27) for the interaction of a graviton with other KK fields. For example consider the interaction term of a graviton with two hidden photons. In higher-dimensional space the interaction term is schematically given by

$$\mathcal{L} \sim X^{(\vec{k})} X^{(\vec{l})} G^{(\vec{p})} e^{im(\vec{k}+\vec{l}+\vec{p})\cdot(\vec{y}-\vec{y}_{SM})} , \tag{4.32}$$

where KK-number vectors have been included. After integrating out the extra dimensions a δ function appears, which imposes

$$\vec{k} = -\vec{l} - \vec{p} \tag{4.33}$$

This conservation of KK number is physically important. For example consider the decay $X^{(\vec{k})} \to X^{(\vec{l})} + G^{(\vec{p})}$. Using $m_k = |\vec{k}|m$ etc.

$$\begin{aligned} |\vec{k}| &\leq |\vec{l} + \vec{p}| , \\ \to m_k &\leq m_l + m_p . \end{aligned} \tag{4.34}$$

Hence it is energetically impossible for such a decay to occur. This result generalises straightforwardly to all decays which involve only KK particles. Hence such decays do not occur.

The situation is different if there is a mixture of SM and KK particles. This can be understood by looking at the $X - \gamma - G$ interaction term. The higher-dimensional Lagrangian is schematically given by

$$\mathcal{L} \sim X^{(\vec{k})} \, A \, G^{(\vec{l})} e^{im(\vec{k}+\vec{l})\cdot(\vec{y}-\vec{y}_{SM})} \, \delta\left(\vec{y} - \vec{y}_{SM}\right) , \tag{4.35}$$

where the $\delta(\vec{y} - \vec{y}_{SM})$ factor should be noted. In this case integrating out the extra dimensions does *not* lead to KK-number conservation. It is therefore possible for these decays to occur. For example the decay $X^{(\vec{k})} \to \gamma + G^{(\vec{l})}$ is energetically possible for all $|\vec{l}| \leq |\vec{k}| - m_\gamma/m$, where m_γ can be non zero in a plasma.

The $X - \gamma - G$ interaction Lagrangian is given by generalising Equation (4.27), but including the KK-number of the hidden photons

$$\mathcal{L} = \sum_{\vec{k}} \sum_{\vec{l}} -\frac{\sin\chi}{2\sqrt{2}M_{pl}} G^{\mu\nu}(\vec{l}) \left(-\eta_{\mu\nu} F^{\rho\sigma} X^{(\vec{k})}_{\rho\sigma} + 4F_{\mu\sigma} X_{\nu}{}^{\sigma(\vec{k})} \right) . \tag{4.36}$$

The total Lagrangian, to 1^{st}-order in $1/M_{pl}$, is therefore given by Equations (4.25), (4.31) and (4.36).

4.2 Summary of Chapter 4

This chapter combines the minimal-hidden-photon model with LED. This is done by taking the Lagrangian for the minimal-hidden-photon model and then extending it to n extra dimensions in Equation (4.2).

The extension assumes that the SM photon is completely confined to the brane, which is located at a general point $\vec{y} = \vec{y}_{SM}$ in the extra dimensions. It is entirely possible that the coordinate y_{SM} is time-dependent. However the low-energy Lagrangian is actually independent of this coordinate, and therefore the low-energy-effective theory is independent of any higher-energy brane dynamics.

Hence any SM field in the extended Lagrangian (Equation (4.2)) is accompanied by a factor $\delta(\vec{y} - \vec{y}_{SM})$. The SM photon therefore does not obtain a tower of KK modes, in accordance with observation.

The presence of the brane breaks higher-dimensional Lorentz invariance, and therefore higher-dimensional Lorentz-breaking and brane-localising hidden-photon terms are generally allowed (see Equation (4.4)). However in this work it is assumed that these terms are negligible in comparison with the higher-dimensional Lorentz-preserving hidden-photon kinetic term. This assumption is not strongly justified, but instead is model dependent. The findings of this work are therefore correspondingly qualified. Further work should explore what happens when these terms are significant.

Simple assumptions are made about the bulk geometry, as is appropriate for a toy model. It is assumed that the bulk can be factorised separately into the brane $\times$ extra dimensions, and that each extra dimension can itself be individually factorised. It is further assumed that the extra dimensions are toroidally compactified, and are all equal in size.

The 4-dimensional effective Lagrangian is obtained by integrating out the extra dimensions. This process produces a tower of hidden-photon KK modes. These KK modes obtain masses naturally from the geometry of the extra dimensions, without the need for a Higgs or Stueckelberg mass term.

This process of integrating out also produces extra scalar particles which are associated with the hidden photon. However these scalar particles are physically decoupled from SM particles and do not produce observable effects.

The form of the kinetic-mixing term is largely unchanged. Now all hidden-photon KK modes interact with the SM photon with the same interaction strength ($\sin\chi$), in accordance with Equation (4.24).

The process of integrating out the extra dimensions supplies the graviton with a tower of KK modes, and also creates a tower of KK modes associated with the dilaton particle. This particle couples to the trace of the energy-momentum tensor of the SM. The interactions of the dilaton are similar in strength to those of the graviton. It will eventually be shown in Chapter 8.2.2 that decays involving the graviton are highly suppressed and therefore always negligible. Therefore the effects of the dilaton are always negligible as well, and this particle can be ignored.

The gravitational Lagrangian is derived, to 1^{st}-order in $1/M_{pl}$. Decays which only involve KK particles are energetically impossible. This is due to the KK-number conservation which comes from integrating out the extra dimensions. However it is possible to have decays which mix KK and SM particles. In this case the SM $\delta(\vec{y} - \vec{y}_{SM})$ factor breaks KK-number conservation, so decays of this form are energetically possible.

5 Calculation of constraints in the KK model

It is helpful to first consider the calculation of constraints in the non-KK model. The hidden-photon effect in a given process is denoted t_X. This is a function of χ and m_X, so it is possible to write $t_X(m_X, \chi)$. The constraint is obtained by imposing that the total hidden-photon effect is larger than some quantity d, which is associated with the process. For example in the case of atomic spectra, the process is a particular atomic transition, and d is the uncertainty in the current knowledge of the energy of this transition. In the case of solar-lifetime constraints, the process is energy loss, and d is the SM-photon luminosity. Setting $t_X > d$ constrains χ as a function of m_X.

In the KK model the total hidden-photon effect is obtained by summing over all KK-mode contributions. Hence

$$t_{X,KK} = \sum_{k=1}^{\infty} t_X(m_X \to m_k = k \times m,\, \chi) > d\,, \tag{5.1}$$

where $k = \sqrt{|\sum_{i=1}^{n} k_i^2|}$. The zero-mass mode does not contribute, as it is physically equivalent to the SM photon (see Chapter 2.1). The upper limit of k is actually quite a subtle issue, and is discussed further in Chapter 6. However for now the upper limit is simply set to be $k = \infty$.

These constraints have a fundamentally different shape from constraints in the non-KK model. In the non-KK model constraints decay as $m_X \to 0$. However KK-model constraints strengthen as $m \to 0$. The reason for this is quite simple. A particular experiment has a typical energy scale E. KK modes become effective in the limit $m \ll E$. If m is decreased, then the total energy range of the KK modes, $E - m$, is increased. Further, the separation of the KK modes, m, is decreased. Hence the effective number of KK modes is increased in two ways and constraints become correspondingly stronger.

5.1 Integral approximation

It is possible to simplify the calculation by replacing the summation by an integral. This is particularly important for large numbers of extra dimensions, where summation becomes practically difficult. It is justified because the errors involved are generally small. This can be seen by considering the Euler-

Maclaurin formula,

$$\sum_{i=1}^{r} f(i) = \int_{1}^{r} f(x)\,dx - B_1\,(f(r) + f(1)) + \ldots\ldots\ldots \tag{5.2}$$

Here the function $f(i)$ becomes the function t_X. The first (and dominant) correction in the formula is given, and is proportional to the first Bernoulli number $B_1 = -(1/2) \sim O(1)$. Therefore the error is approximately just the lowest-mass and highest-mass contributions. This is generally washed out by the large number of contributions from other modes, so the error is small. Therefore it is possible to make the replacement

$$\sum_{k=1}^{\infty} \to \int_{k=1}^{\infty} d^n k. \tag{5.3}$$

The extra dimensions are assumed to be geometrically identical, and therefore the integral is radially symmetric. Hence it is possible to make the further replacement

$$d^n k \to S_n\, k^{n-1}\, dk\,, \tag{5.4}$$

where the angular integration is given by

$$S_n = \frac{2\pi^{\frac{n}{2}}}{\Gamma\left(\frac{n}{2}\right)}\ . \tag{5.5}$$

Overall the constrained region is given by

$$t_{X,KK} = \int_{k=1}^{\infty} d^n k\ \ t_X(m_X \to m_k = k \times m,\, \chi) > d\ . \tag{5.6}$$

5.2 Summary of Chapter 5

Constraints in the KK model are obtained by summing the contributions from all KK modes. The summation is generally replaced with an integral, by using the Euler-Maclaurin formula. This simplifies calculation and the errors are small.

The KK constraints have a fundamentally different shape to constraints from the non-KK model. The non-KK constraints decay as $m_X \to 0$. This is because the hidden photon becomes indistinguishable from the SM photon and the physical effect of the hidden photon disappears. However the KK constraints strengthen in the limit $m \to 0$. This is because the effective number of KK modes increases, and so does the total physical effect.

6 Ultraviolet (UV) divergences

In the KK model the total hidden-photon effect is given by summing over KK modes. This generally includes contributions from very high-mass KK modes. It is therefore necessary to check carefully for UV divergences, which would indicate a breakdown of the theory. More specifically it is necessary to check that predictions are finite for all considered experiments.

For this purpose experiments are divided into two categories; real production and virtual production. This distinction is important because in each category the theory exhibits very different UV behaviour.

- Real production:
  In these experiments the hidden photon is directly detected and therefore needs to be a real particle. This category includes solar-lifetime, CAST, HB-lifetime, IDPB, SN1987a, and fixed-target experiments.

- Virtual production:
  In these experiments the hidden photon is not explicitly detected and therefore does not need to be a real particle. For example the atomic-spectral constraints involve a hidden-photon insertion to the SM-photon propagator, which modifies the Coulomb potential (Figure 5). Similarly the hidden-photon correction to the electron vertex function in QED (see Figure 10) alters the anomalous magnetic moment of SM fermions, leading to constraints.

It should be noted that, strictly speaking, the Z-boson mass experiment does not fit into either of these categories. This is because a hidden photon is not actually produced, but instead the hidden photon causes a modification to the tree-level quantity which is the Z-boson mass. However this experiment does actually exhibit all of the important features associated with virtual-production experiments, and can be regarded as a kind of an "effective" virtual-production experiment. This is explained further in Chapters 6.2 and 8.

6.1 UV divergences in real production

Thermal production is considered first. This applies in the solar-lifetime, HB-lifetime and SN1987a experiments. After summation over KK modes the total hidden-photon effect is given by Equation (5.6). t_X contains a Boltzmann-exponential production factor $\sim e^{-E/T}$, where T is the typical temperature scale of the process. This factor sharply cuts out the contribution of KK modes with masses $\gtrsim T$. Hence it is possible to just use Equation (5.6) and with an upper limit of $k = \infty$. The total hidden-photon effect is always UV finite.

The other real-production experiments have an experimentally-imposed upper limit to the energy. In Chapter 15 it is shown that the Intergalactic-Diffuse-Photon-Background (IDPB) experiment receives no contribution from KK modes with mass $> 2\,m_e$. In fixed-target experiments the original beam is monoenergetic with energy E_0, so there is again an upper limit for the KK-mode mass of E_0. The CAST detector has an upper limit of 15 keV, setting an upper limit on the mass of KK modes which can be detected. In all of these experiments there is therefore an experimentally-imposed upper limit for k in Equation (5.6), which results in a finite value for the total hidden-photon effect.

Therefore for real production the theory always gives UV-finite values for the total hidden-photon effect.

6.2 UV divergences in virtual production

For $a_{e,\mu}$ the hidden-photon contribution is a loop effect and the high-energy behaviour is governed by the powers of momentum in the loop integrals. Therefore at high-masses the hidden-photon effect dies off as a power law. More precisely the decay goes as $\sim m_k^{-2}$ (see Equation (10.7)).

For atomic spectra the hidden-photon contribution is a tree-level effect (see Figure 5), so the high-mass behaviour is less obvious. However in Appendix D it is shown that the decay is still a power law, and more specifically that the hidden-photon effect dies as $\sim m_k^{-2(1+l)}$. Here l is the lowest value of angular momentum for any state in the transition, so a $2\,s - 2\,p$ transition would have $l = 0$ and a $3\,p - 3\,d$ transition would have $l = 1$.

For virtual production it is possible to use Equation (5.6), and write the high-mass contribution of KK modes as $t_X \sim \chi^2\, m_k^{-q}$, where q is a positive integer.

A naïve calculation can be made by summing up to an value of $k = \infty$. For $n < q$ this sum is convergent, so the theory is manifestly UV finite. However for $n \geq q$ the summation diverges. However the theory can be salvaged by noting that it is essentially an effective theory, and is only expected to hold over a finite domain. Therefore the theory can be made UV finite by imposing an UV-cutoff mass M_c. The summation in Equation (5.6) with an upper limit of $k = M_c/m$ is UV finite.

The value of M_c is not obvious. In string theory the typical width of the SM brane is given by $1/M_*$. Therefore it is reasonable to expect that the theory should be valid up to $\sim M_*$. However in the low-energy-effective theory it is appropriate to set $M_c = aM_*$, where a is the UV-cutoff uncertainty parameter. a is essentially a free parameter, and parametrises unknown aspects of a more-fundamental higher-energy theory which might slightly move the UV cutoff away from M_*. It is reasonable to expect that M_c is within an order of magnitude or so of M_*, and therefore a is allowed to vary in the range $0.1 - 10$.

Introducing the UV cutoff,

$$t_{X,\,KK,\,\text{virtual}} = \int_{k=1}^{\infty} d^n k \; t_X(m_X \to m_k = k \times m,\, \chi) > d \;, \quad n < q,$$

$$= \int_{k=1}^{\frac{aM_*}{m}} d^n k \; t_X(m_X \to m_k,\, \chi) \sim \int_{k=1}^{\frac{aM_*}{m}} d^n k \; \frac{1}{(k \times m)^q} > d \;, \quad n \geq q \,. \quad (6.1)$$

From simple power counting it can be seen that the $n = q$ effect varies logarithmically with a and the $n > q$ effects vary as a power law in a, where the power increases with n.

Atomic spectra (see Chapter 9.2), and the Z-boson mass also involve virtual production, so it again generally necessary to impose the UV cutoff $M_c = aM_*$ in order to make the total hidden-photon effect UV finite, and constraints generally have uncertainties from the parameter a.

6.3 Summary of Chapter 6

The total hidden-photon effect in the KK model is obtained by summing over KK modes. This may include contributions from very high-mass KK modes. It is therefore necessary to check that the summation does not produce unphysical UV divergences.

In real-production experiments there is always an experimentally-imposed upper limit to the mass of KK modes. Therefore there are no contributions from arbitrarily-high-mass KK modes, and the theory is manifestly UV finite.

However for virtual-production experiments there is no such experimental upper limit on the energy. For a small enough n it is possible to sum over KK modes up to $k = \infty$ and obtain a finite result for the total hidden-photon effect. Therefore for small enough n the theory is UV finite for virtual production. However for large enough n the hidden-photon effect diverges if arbitrarily-high-mass modes are included.

The theory can be saved by regarding it as an effective one, which only holds up to a mass scale M_c. M_c should similar to M_*. However uncertainties can be accounted for by setting $M_c = aM_*$, where a is an uncertainty parameter which accounts for unknown higher-energy physics. M_c should be within an order of magnitude or so of M_*, and therefore a is allowed to vary in the range $0.1 - 10$. Constraints from virtual-production therefore generally contain uncertainties from the a parameter. These uncertainties increase with n.

7 The effective perturbation parameter

In this work the total hidden-photon effect is estimated by considering just the lowest order contribution. However in virtual production there will in general be an infinite number of contributions from higher-order diagrams. In order for perturbation theory to be valid, the effective coupling constant must always be $\ll 1$. In the KK theory the summation over KK modes means that

$$\chi^2_{eff,\,pert} \sim \chi^2 \times \text{Number} \quad \text{of} \quad \text{modes} \sim \chi^2 \times \int_{k=1}^{\frac{aM_*}{m}} d^n k\,, \tag{7.1}$$

which implies that

$$\chi^2 \ll \frac{1}{\sqrt{\int_{k=1}^{\frac{aM_*}{m}} d^n k}}\,. \tag{7.2}$$

is required.

Therefore in virtual-production experiments there are effectively two constrained regions of χ. Equation (6.1) produces a lower boundary for χ: above this boundary the hidden-photon physical effect is too large to fit with observation and hence χ is ruled out. However Equation 7.2 produces an upper boundary for χ: above this boundary perturbation theory breaks down, so no constraint can be obtained via the present method. It is necessary for the lower boundary to occur below the upper boundary for any constraint to be obtained. However it will eventually be shown that this does not occur, and therefore that no constraints are obtained for the KK model in virtual-production experiments.

8 Hidden-photon reabsorption

In some experiments a hidden photon can be produced but then "reabsorbed". This means that it can decay or scatter in such a way that it is not experimentally observable. It would then not contribute to the overall hidden-photon effect.

Consider for example the SN1987a energy-loss experiment. If a produced hidden photon manages to traverse the supernova interior then it escapes into space and contributes to energy loss. However it is possible for the hidden photon to decay back into SM particles whilst still inside the supernova interior, transferring its energy on to these SM particles. These SM particles interact strongly with surroundings and have a negligible chance of escape. Therefore the energy of the hidden photon does not escape the supernova, and there is no contribution to energy loss. Similarly it is possible for the hidden photon to scatter off particles in the supernova interior. If this occurs then the hidden photon loses energy in the scattering process, which is transferred back to the supernova. If the hidden photon subsequently exits the supernova interior then the energy it carries away is reduced.

It should be noted that a single collision does not transfer all of the hidden-photon energy back into the supernova. However the transferred energy is generally a significant fraction. This work makes the (slightly) conservative assumption that the hidden photon loses all of its energy during any scattering event. This simplifies calculations considerably and also produces slightly pessimistic and therefore robust constraints.

The hidden-photon reabsorption can be accounted for by multiplying by an escape factor e^{-l/l_0}, where l is the escape distance, and l_0 is the hidden-photon mean free path. This escape factor gives the fraction of hidden photons which are not reabsorbed, and therefore contribute to the observed effect.

In Chapter 6 two separate experimental categories are identified; real and virtual. The status of reabsorption in these two categories is very different.

In virtual production decays and scattering are higher order loop processes, and therefore negligible. Hence in virtual production it is possible to ignore reabsorption to a very good approximation, and assume that any produced hidden photons contribute to the total hidden-photon effect.

Recall that in the "effective" virtual-production experiment which considers the Z-boson mass, no hidden photon is actually produced, and therefore that reabsorption is again not an issue.

However in real production both types of reabsorption are generally important. Decays still happen at higher order, but still take place if the mean free path $\lesssim$ the experimental length scale. Some cases of real-production experiments also occur in non-vacuum regions. Here scattering generally takes place. Therefore in real-production experiments it is generally necessary to account for reabsorption by multiplying by the escape factor e^{-l/l_0}.

8.1 Constraints with an upper boundary

In real-production experiments there are generally two factors determining the hidden-photon effect; a production factor and the escape factor e^{-l/l_0}.

A constraint is obtained by imposing that the total hidden-photon effect is large enough to be experimentally observable. The constraint then consists of both a lower and an upper boundary.

Roughly speaking the lower boundary comes from the production factor and the upper boundary comes from the reabsorption factor. If χ is smaller than the lower boundary then production is too small. The hidden-photon effect is not observable, and this region is not ruled out. If χ is larger than the upper boundary then the hidden photon is reabsorbed too strongly. Hence the hidden-photon effect is not large enough to be observed, and this region is not excluded. The total hidden-photon effect is only large enough for observation in the intermediate region, and this region is excluded.

There are three experiments of this form; fixed-target, SN1987a energy-loss and IDPB.

In fixed-target experiments (see Chapter 11) the hidden photon is produced by an electron beam scattering off the positive ions in the target material. If the hidden photon is to be observed then it must traverse the target plus an extra shielded region before decaying (see Figure 14). This causes the escape factor, which produces the upper boundary for constraints (see for example Figure 15).

In the SN1987a experiment (see Chapter 16) it is necessary for the hidden photon to escape the confining region of the supernova core, in order to con-

tribute to energy loss. This produces the escape factor, which results in an upper boundary for the constraint (see for example Figure 31).

In the IDPB experiment (see Chapter 15) hidden photons are produced in the early universe. To be detected the hidden photons must then survive until the present day. The fraction of contributing hidden photons is then given by a "survival" factor rather than an "escape" factor, but the end result is still an upper boundary for the constraint (see example Figures 27 and 29).

Note however there are some real-production experiments in which constraints which do not have an upper boundary.

In the solar experiments (which produce the solar-lifetime and CAST constraints) and also the HB-lifetime experiment, scattering can occur. However reabsorbed hidden photons cause forbidden non-local energy transfer within the sun or the HB star and therefore still contribute to constraints. This is explained further in Chapters 12.1 and 13.1.

8.2 Different modes of reabsorption

This section discusses in detail the various modes of hidden-photon reabsorption. The first type of reabsorption process is scattering. This is important in non-vacuum conditions. The second type of reabsorption process is decay.

There are two categories of decay for the hidden photon,

- $X \rightarrow$ SM only decays:
  Most of these processes are when the hidden photon decays to a pair of SM fermions, for example $X \rightarrow e^+ + e^-$ etc. However there is also the loop-level decay $X \rightarrow \gamma + \gamma + \gamma$. These decays are discussed further in Chapter 8.2.1.

- $X \rightarrow \gamma + G$ decays:
  In Chapter 8.2.2 it is shown that these decays are negligible in comparison with ones of the form $X \rightarrow$ SM only.

Hence it is only necessary to account for decays of the form $X \rightarrow$ SM only.

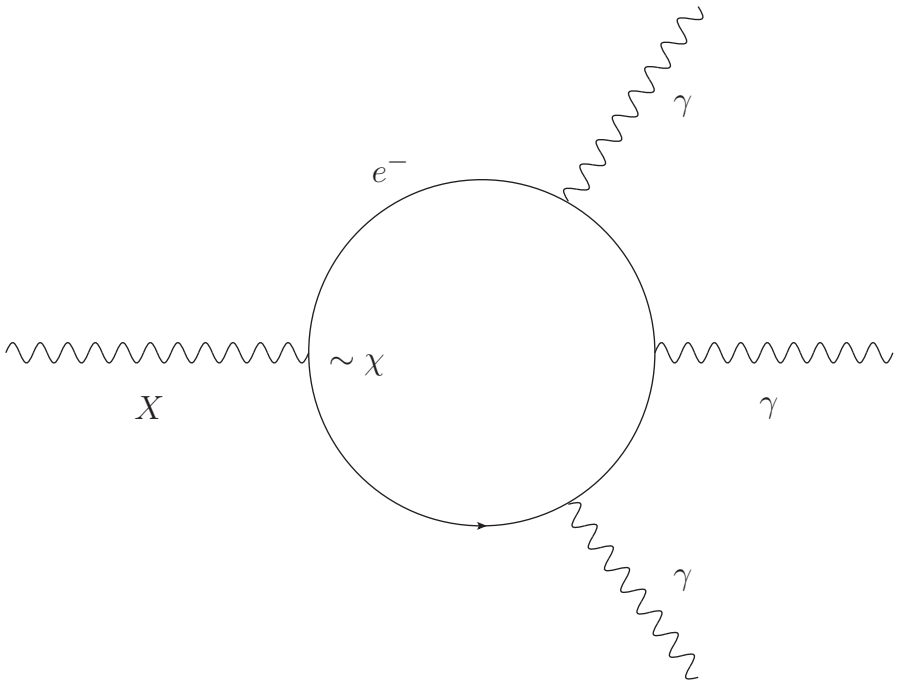

Figure 4: A Feynman diagram for the decay $X \to \gamma+\gamma+\gamma$. For $m_X \leq 2\,m_e$ this is the only decay channel for decays of the form $X \to$ SM only. The factor of χ has been highlighted. In the region $m_X > 2\,m_e$ the decay channel $X \to e^+ + e^-$ becomes available and dominates over the loop process.

8.2.1 $X \to$ SM only

These decays occur in both the non-KK and KK models, and are generally important.

At low masses $m_X \leq 2\,m_e$ the only decay of the form $X \to$ SM is the loop decay $X \to \gamma + \gamma + \gamma$. A Feynman diagram for this process is shown in Figure 4. Note that this diagram only depicts the contribution with an electron in the loop, but there are actually contributions with higher-mass SM particles in the loop. However these other contributions are always negligible (see Appendix B). The decay rate for $m_X \lesssim 2\,m_e$ is published in [3], and the decay rate for

$m_X \gtrsim 2\,m_e$ is calculated in Appendix A,

$$\begin{aligned}\Gamma_{X\to\gamma+\gamma+\gamma} &\sim \frac{17\chi^2\,\alpha^4\,m_X^9}{11664000\,\pi^3\,m_e^8}, && m_X \lesssim 2\,m_e,\\ &\sim (2.5\times10^{-2})\,\chi^2\,\alpha^4\,m_X, && m_X \gtrsim 2\,m_e\,. \end{aligned} \tag{8.1}$$

It is sometimes necessary to show that this loop decay is negligible in a given experiment. This is achieved by constructing a lower bound for the hidden-photon mean free path, and showing that it is larger than the experimental length scale. The mean free path is then given by Equation (8.1) together with the equation for a mean free path

$$l_0 = \gamma \times \frac{1}{(\Gamma/\mathrm{eV})} \times (2\times10^{-7})\,\mathrm{metres}\,, \tag{8.2}$$

where $\gamma = E/m_X$ is the Lorentz factor, and the final multiplicative factor is for conversion from eV^{-1} to metres. First it is noted that the decay rate is maximised (and the mean free path is minimised) if it is assumed that $m_\gamma = 0$, as this leaves the maximum phase space for decay. The mean free path is further minimised if $m_X \sim E_{\max}$, where $E_{\max}$ is the highest energy scale of a given experiment. Overall

$$l_{0,\,X\to\gamma+\gamma+\gamma,\,\min} \sim \frac{7\times10^{54}}{\chi^2\,(E_{\max}/\mathrm{eV})^9}\,\mathrm{metres}\,. \tag{8.3}$$

Consider for example solar-lifetime experiments. Here $E_{\max} \sim 0.1$ MeV, which leads to $l_0 \gtrsim (7\times10^9\,\mathrm{metres})/\chi^2 \gtrsim 7\times10^9$ metres for all $\chi \gtrsim 1$. This is much larger than the solar radius $R_\odot \sim 7\times10^8$ metres, so the loop decay is negligible in this experiment.

For $m_X > 2\,m_e$ the process $X \to e^+ + e^-$ becomes available. This has three fewer powers of α than the loop process, and therefore dominates. The decay rate is given by [3]

$$\Gamma_{X\to e^+ + e^-} \sim \frac{\alpha\chi^2\,m_X}{2}\sqrt{1-\left(\frac{2\,m_e}{m_X}\right)^2}\left(1+\frac{2\,m_e^2}{m_X^2}\right), \quad m_X > 2\,m_e\,. \tag{8.4}$$

In the KK model the decay rate is obtained by making the replacement $m_X \to m_k = k\times m$.

At even higher energies there are more decays of the form $X \to f^+ + f^-$ where f^- is a SM fermion with $m_f > m_e$, for example a muon. The decay rates

are given by

$$\Gamma_{X\to f^+ + f^-} \sim Q_f^2 \times \frac{\alpha\chi^2 m_X}{2}\sqrt{1-\left(\frac{2\,m_f}{m_X}\right)^2}\left(1+\frac{2\,m_f^2}{m_X^2}\right), \quad m_X > 2\,m_f\,, \tag{8.5}$$

where Q_f is the magnitude of the electric charge of f in units of e. These higher-mass decays are only important in the fixed-target experiments, which operate at energies $\gtrsim 10$ GeV.

8.2.2 $X \to \gamma + G$ decays

This decay comes from the Lagrangian term $\sim X\gamma\,G$. It is easy to show that this decay is negligible, in both the non-KK and KK models. This is achieved by constructing an upper bound for the decay rate, and showing that this is highly suppressed with respect to the decay rate for $X \to \gamma + \gamma + \gamma$.

The non-KK model is considered first, the decay rate for which is calculated in Appendix C. Here $m_G = 0$. An upper bound is constructed by setting the SM-photon mass $m_\gamma = 0$,

$$\begin{aligned}\Gamma(X\to\gamma+G) &\leq \Gamma(X\to\gamma+G)\Big|_{m_G=0,\,m_\gamma=0}\\ &= \frac{\chi^2 m_X^3}{12\,\pi M_{pl}^2}\,.\end{aligned} \tag{8.6}$$

By comparison with Equation (8.1) it can be seen that the decay $X \to \gamma + G$ is indeed highly suppressed with respect to $X \to \gamma + \gamma + \gamma$ decay, and is therefore negligible.

The KK model is now considered. The total decay rate is now obtained by summing over all possible final-state gravitons, that is all $|\vec{l}| \leq |\vec{k}| - m_\gamma/m$. This is given by

$$\Gamma\left(X^{(\vec{k})}\to\gamma+G,\,\text{total}\right) = \int_0^{(m_k-m_\gamma)} d^n l \;\; \Gamma(m_k, m_l)\,, \tag{8.7}$$

where $\Gamma(m_k, m_l)$ is the decay rate for a hidden photon with mass m_k to a graviton with mass m_l, and the integration element $d^n l$ is given by Equations (5.4) and (5.5) with $k \to l$.

It is now necessary to calculate an upper bound for the decay rate. Again m_γ is set to 0. Furthermore the decay rate increases with the number of extra

dimensions n, so the maximum value of $n = 6$ is used. Overall

$$\Gamma\left(X^{(\vec{k})} \to \gamma + G, \text{total}, n = 6, \max\right) = \frac{\chi^2 m_k^9 \pi^2 (1120 \ln 2 - 729)}{(30240\, m^6\, M_{pl}^2)}\,. \tag{8.8}$$

This can be rewritten in a more transparent form by replacing M_{pl} using Equation (3.3),

$$\Gamma\left(X^{(\vec{k})} \to \gamma + G, \text{total}, n = 6, \max\right) = \frac{\chi^2 m_k^9 (1120 \ln 2 - 729)}{(1935360\, \pi^4 M_*^8)}\,. \tag{8.9}$$

Comparing Equations (8.6) and (8.9) it can be seen that the summation over final-state KK modes has caused the replacement of the 4-dimensional Planck mass M_{pl} with the higher-dimensional Planck mass M_*. This increases the decay rate substantially. Nevertheless by comparing Equations (8.9) and (8.1) and noting that $M_* \gg m_e$, it can be seen that the decay $X^{(\vec{k})} \to \gamma + G$ is highly suppressed relative to the one for $X \to \gamma + \gamma + \gamma$.

Therefore the decay of a hidden photon to a SM photon plus graviton is negligible in both the non-KK and KK models.

8.3 Summary of Chapter 8

In some experiments it is possible for a hidden photon to be produced but not observed, due to reabsorption. Reabsorption is not significant in virtual-production experiments, but is generally important in real-production experiments.

This reabsorption is parametrised by including a hidden-photon escape factor e^{-l/l_0}. Constraints then obtain an upper boundary. Above this upper boundary reabsorption is too large so no hidden-photon effect is observable and no constraint is obtained. Below the lower boundary production is too small, so again no effect is observed and no constraint is obtained. The hidden photon is only constrained in the intermediate region.

The hidden photon can be reabsorbed through scattering or decay. Scattering occurs when the hidden photon travels through a non-vacuum region. There are several terms in the Lagrangian which suggest hidden-photon decays. However the only significant decays are of the form $X \to$ SM only. These decays consist of the loop-level decay $X \to \gamma + \gamma + \gamma$ and tree-level ones of the form $X \to f^+ + f^-$, where f^- is a SM fermion. The loop-level decay is the

only possible one for $m_X \leq 2\,m_e$. However for $m_X > 2\,m_e$ the tree-level decays dominate.

9 Atomic-spectral constraints

9.1 Atomic-spectral constraints for the non-KK model

This chapter uses atomic spectra to constrain hidden photons.

9.1.1 Coulomb's law with hidden photons

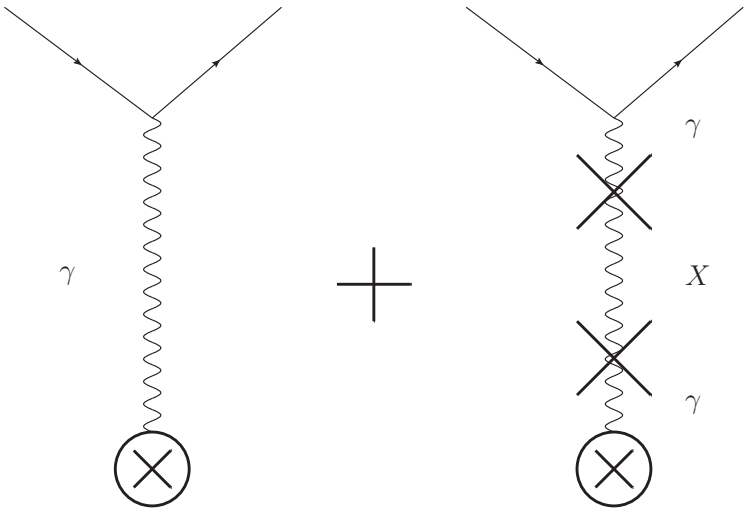

Figure 5: Feynman diagrams for the electromagnetic potential. The first contribution is from the SM photon. The second contribution is from the hidden photon, and leads to a modification of Coulomb's law (see Equation (9.1)).

The kinetic-mixing term in Equation (2.1) causes a tree-level insertion to the photon propagator as shown in Figure 5. In the static limit this leads to the addition of a new Yukawa-like term to the Coulomb potential [16]

$$V(r) = -\frac{Z\alpha}{r}(1 + \chi^2 e^{-m_X r}) \equiv V_{\text{Coulomb}}(r) + \delta V(r)\,, \tag{9.1}$$

where Z is the charge, α is the fine-structure constant, and small-angle approximations have been used for χ.

Chapter 2 discussed how the physical effects of the hidden photon die off in the limits $m_X \to 0$ and $m_X \to \infty$. This is clearly demonstrated by the static Coulomb potential,

- $m_X \to 0$:
  In this region the exponential term tends to unity and the original Coulomb potential is recovered up to a factor $(1 + \chi^2)$. This can be absorbed in the definition of α, making it unobservable. Hence the hidden photon is not observable. This is physically sensible, since in the limit $m_X \to 0$ the hidden photon becomes indistinguishable from the SM photon.

- $m_X \to \infty$:
  Here the exponential term dies off and the original Coulomb potential is recovered. Physically this is because as $m_X \to 0$ the hidden photon becomes impossible to excite as a virtual particle and therefore does not contribute to the electromagnetic force.

- Intermediate m_X:
  In this region there are non-zero deviations from Coulomb's law. In particular the largest deviation occurs for $m_X \sim 1/l$ where l is the typical length scale of the experiment.

Therefore any constraints on hidden photons are strongest around $m_X \sim l$ and drop off in the limits $m_X \to 0$ and $m_X \to \infty$. For atomic spectra l is approximately the Bohr radius of the atom or ion involved in the transition.

The Bohr radius of ordinary atomic hydrogen corresponds to a mass scale ~ 1 keV. Existing spectroscopic constraints probe this region [7,8,36]. However there exist a range of different atomic systems, including ordinary hydrogen, muonic atoms, and more exotic atoms. Many atomic systems have higher reduced masses than atomic hydrogen and are therefore sensitive to larger values of m_X. These include muonic hydrogen (where the e^- from atomic hydrogen is replaced by a μ^-), and hydrogenic ions with $Z > 1$. Also it is possible that certain exotic atoms, such as pure-QED systems, have smaller fractional uncertainties than atomic hydrogen. This might produce stronger constraints.

9.1.2 Obtaining constraints using atomic spectra

Hidden-photon constraints are obtained by adapting the method presented in [13], where the $2\,s_{1/2} - 2\,p_{1/2}$ Lamb shift transition in atomic hydrogen is used to constrain minicharged particles (MCPs).

At 1^{st}-order in perturbation theory the energy shift of a state $|\psi_n\rangle$ is given by

$$\delta E_n^{(1)} = \langle \psi_n \mid \delta V \mid \psi_n \rangle \,, \tag{9.2}$$

where the $|\psi_n\rangle$ are the 0^{th}-order wavefunctions, and δV is the perturbation to the potential. For this to be a good approximation the energy shift should be small. This is consistent with what is expected for the hidden-photon effect, since so far no large deviation from the standard QED prediction has been observed. If the standard prediction and the experimentally measured values agree, it is possible to impose that $\delta E_n^{(1)}$ must be smaller than the uncertainty in the transition. This results in a constraint on δV.

A few important points should be noted about these uncertainties,

- "Same-n transitions" and "different-n" transitions:

  Note that in this context n is the principal quantum number of an atomic energy level and *not* the number of extra dimensions. The theoretical energy of a state can generally be written as

  $$E_{n,l,j} = E_{n,j}^{D,R} + L_{n,l,j} \,, \tag{9.3}$$

  where the first term is the sum of energies from the Dirac equation plus recoil corrections (effectively the 0^{th}-order energy). The second term is the Lamb shift, defined as any contribution which separates states of the same n,j.

  The first term is proportional to the Rydberg constant R_∞ and has an uncertainty $\sim 10^{-10}$ eV [62]. Therefore any transitions between states of different n in atomic hydrogen has a theoretical-error contribution of $\sim 10^{-10}$ eV from R_∞.

  The situation is worse in exotic atoms, as the effective Rydberg constant is modified by a factor proportional to the reduced masses μ_H, μ_{exotic} of atomic hydrogen and the exotic atom respectively,

  $$R_{eff} = \frac{\mu_{exotic}}{\mu_H} R_\infty. \tag{9.4}$$

  Therefore in, for example, muonic hydrogen, there would be a fractional uncertainty of around 10^{-7} due to the mass of the muon. This would cause an overall uncertainty of $\gtrsim 0.1$ meV.

However same-n transitions do not have a 0^{th}-order energy and are limited only by uncertainties in the Lamb shifts of the states.

- Definition of "uncertainty":
  When forming constraints the total uncertainty of a quantity is estimated by adding together the absolute values of the $1\,\sigma$ theoretical and experimental errors, that is for a given measurement M,

$$\Delta M = |\Delta M_{th}| + |\Delta M_{exp}|\,. \tag{9.5}$$

  The quantity ΔM has been constructed by adding absolute uncertainties. It therefore constitutes a conservative estimate of the error, and produces slightly pessimistic and therefore robust constraints.

  In the case of different-n transitions there is a contribution from the Rydberg constant. However the major contribution to ΔM_{th} generally comes from finite-nuclear-size effects. For most of the considered atoms, data for the finite-nuclear size is consistent. For example the hydrogen-like helium ion has three different electron-scattering determinations, and also a muonic-helium-ion determination, of the alpha-particle charge radius. These values all agree within $1\,\sigma$ [63], meaning that to a good approximation the theoretical value for a transition can be calculated by assuming one particular value of the nuclear radius. It is therefore possible to estimate the uncertainty from finite-nuclear-size effects simply by considering the uncertainty in this one value of the nuclear radius. This is indeed what is done in the cited theoretical calculations, and the corresponding error is included in $|\Delta M_{th}|$.

  However for atoms with a proton nucleus things become more complicated. The recent muonic-hydrogen determination of $r_p = 0.84184(67)$ fm [64] provides the most precise measurement from atomic spectra. This disagrees with the best previous atomic-spectral determination of $r_p = 0.8768(69)$ fm from [62] by around $5\,\sigma$. The muonic-hydrogen extraction also deviates by around $2.5\,\sigma$ from the best electron-scattering determination of $r_p = 0.897(18)$ fm [65]. For conservative and robust constraints it is therefore necessary to modify the error analysis to account for the large

variation in r_p by adding a term $|\Delta M(r_p)|$,

$$\widetilde{\Delta M} = |\Delta M_{th}| + |\Delta M_{exp}| + |\Delta M(r_p)|. \tag{9.6}$$

To leading order the proton-radius contribution to a given state is [66]

$$E_{NS}(r_p) = \frac{2\, m_o^3 \alpha^4 r_p^2}{3n^3}\delta_{l0}\,, \tag{9.7}$$

where m_o is the mass of the orbiting particle. For example in atomic hydrogen $m_o = m_e$, and in muonic hydrogen $m_o = m_\mu$. It is possible to roughly estimate $|\Delta M(r_p)|$ by considering two widely-separated values of the proton radius. Denoting $r_{p,\mu} = 0.84184(67)$ fm as the muonic-hydrogen determination, and $r_{p,e} = 0.897(18)$ fm as the electron-scattering determination,

$$|\Delta M(r_p)| = |E_{NS}(r_{p,e}) - E_{NS}(r_{p,\mu})|. \tag{9.8}$$

$\widetilde{\Delta M}$ is used for constraints from atoms with a proton nucleus and ΔM is used for constraints from all other atoms.

Errors quoted in the text are always at the 1 ΔM (or $\widetilde{\Delta M}$) level. However unless otherwise stated the constraints produced in the figures are always at the 2 ΔM (or 2 $\widetilde{\Delta M}$) level.

- Charge radius of the proton and other nuclei:

  As already discussed the charge radius of the nuclei is a major source of uncertainty. In addition it is necessary to make sure that the determinations of the radius are from an independent source. For example it is *not* possible take a measurement of the Lamb shift in ordinary hydrogen to measure both the radius of the proton and put a constraint on deviations from Coulomb's law. Two independent measurements are needed. Moreover to avoid even partial degeneracies (which tend to weaken the constraint in particular at short length scales), it is best if the determination of the radius is obtained at relatively-high momentum transfer, corresponding to a short length scale. Therefore these determinations are usually taken from electron-scattering data.

9.1.3 Searching for deviations from Coulomb's law

Constraints will first be produced using a "naïve" method. These are formed using only one transition. It will be shown that this naïve method works properly for same-n transitions, producing constraints which decay correctly in the limit $m_X \to 0$. However it will also be shown that for different-n transitions the naive method produces constraints which do not decay properly in the limit $m_X \to 0$.

This "naïve" method is first demonstrated by using the $2\,s_{1/2} - 2\,p_{1/2}$ Lamb-shift transition in atomic hydrogen, which is a same-n transition. For this case Equation (9.2) leads to

$$\delta E = \int_0^\infty dr\, r^2 \delta V(r) \left[R_{20}^2(r) - R_{21}^2(r)\right] = -\frac{\chi^2\, \alpha\, a_0\, m_X^2}{2(1 + a_0\, m_X)^4}\,, \tag{9.9}$$

where δV given by Equation (9.1), and the normalized radial hydrogen wave-functions $R_{n\ell}$ are given by

$$R_{20}(r) = \frac{1}{\sqrt{2}\, a_0^{3/2}} \left(1 - \frac{\rho}{2}\right) e^{-\rho/2}\,,\ R_{21}(r) = \frac{1}{2\sqrt{6}\, a_0^{3/2}} \rho\, e^{-\rho/2}\,, \tag{9.10}$$

where $\rho = r/a_0$ and $a_0^{-1} = \alpha\, m_e$.

There is an experimental uncertainty of 3 kHz [67] and theoretical uncertainty of 6 kHz [68], as well as a contribution of 17 kHz from $|\Delta M(r_p)|$ (see Equation (9.8)). Equation (9.6) therefore gives $\widetilde{\Delta M} = 10^{-10}$ eV. The constraints for the $2\,s_{1/2} - 2\,p_{1/2}$ transition is shown as the blue curve in Figure 6, and is at the 2 $\widetilde{\Delta M}$ level.

This constraint has the correct shape. It dies off the in the limits $m_X \to 0$ and $m_X \to \infty$, and is strongest at $m_X \sim 1/a$, where the Bohr radius a is the typical length scale involved.

This method can also be applied to the $1\,s_{1/2} - 2\,s_{1/2}$ transition in atomic hydrogen. The experimental value of this transition has a relative uncertainty 2.8×10^{-14}, and it represents the most precise measurement of atomic hydrogen [69]. However the constraints are limited by a much larger theoretical uncertainty. As already discussed there are uncertainties of around 10^{-10} eV from the Rydberg constant as well as a similar contribution from the Lamb shifts of the states [70]. Furthermore it is necessary to add the $|\Delta M(r_p)|$ contribution

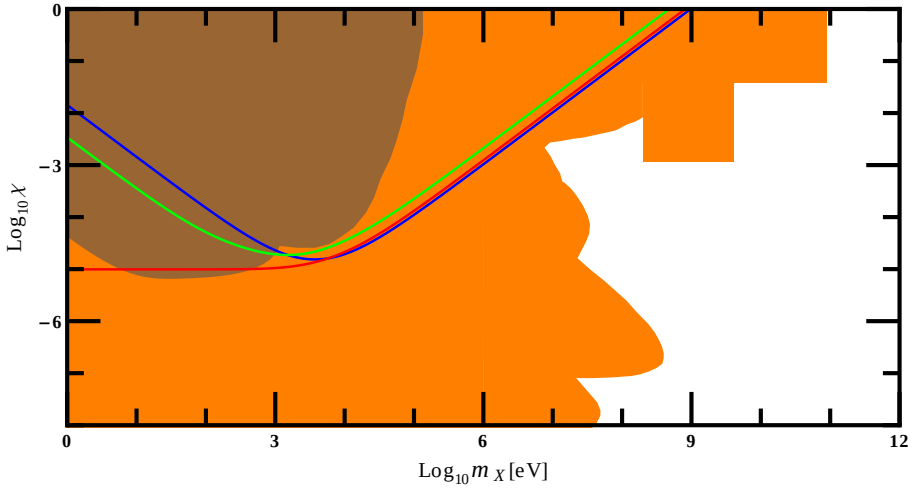

Figure 6: The blue curve denotes the constraint on hidden photons obtained from the $2\,s_{1/2} - 2\,p_{1/2}$ transition in atomic hydrogen. The constraint uses a conservative error of $2\ \widetilde{\Delta M} = 2 \times 10^{-10}$ eV, where $\widetilde{\Delta M}$ is defined in (9.6). For same-n transitions χ automatically dies off correctly for both small and large m_X. The red curve shows the naïve constraint from the $1\,s_{1/2} - 2\,s_{1/2}$ transition in atomic hydrogen. It exhibits incorrect behaviour at small m_X. The green curve gives a correctly shaped constraint, which is obtained by combining the $1\,s_{1/2} - 2\,s_{1/2}$ with the $2\,s_{1/2} - 8\,s_{1/2}$ transition, according to the renormalization procedure described in Chapter 9.1.3. The green and blue constraints are two of the strongest from atomic spectra, and are combined together in the non-KK model summary plot in Figure 1. For comparison previously published constraints are depicted as the colour filled regions. Those corresponding to pure tests of Coulomb's law (also obtained from atomic spectra) are highlighted in brown [7, 8, 36]. The remaining white region corresponds to unexplored parameter space.

of $\sim 7 \times 10^{-10}$ eV, to get $\widetilde{\Delta M} = 1 \times 10^{-9}$ eV. The 1^{st}-order energy shift is

$$\begin{aligned}\delta E &= \int_0^\infty dr\, r^2 \delta V(r) \left[R_{20}^2(r) - R_{10}^2(r)\right] \\ &= \chi^2 \alpha \left[\frac{12 + a_0\, m_X(60 + a_0\, m_X(87 + 14 a_0\, m_X(4 + a_0\, m_X)))}{4a_0(1 + a_0\, m_X)^4(2 + a_0\, m_X)^2}\right], \quad (9.11)\end{aligned}$$

where

$$R_{10}(r) = \frac{2}{a_0^{3/2}} e^{-\rho}\,, \quad (9.12)$$

and where again $\rho = r/a_0$ and $a_0^{-1} = \alpha\, m_e$.

The result is shown in Figure 6 as the red curve. This constraint does not have the correct drop off for small masses. This can be understood by looking at $\delta V(r)$ in Equation (9.1), which dies off at large m_X but grows at small m_X. Therefore the constraint saturates at small masses, which is not physically correct.

This is simply an artefact of the calculation method, caused by the particular choice for the splitting of the potential in Equation (9.1). At small masses the perturbation reduces to a term that has the form of a Coulomb potential, but with an extra factor $(1 + \chi^2)$. This effectively increases the strength of the electromagnetic coupling and therefore the energy difference between the two states. In other words the coupling α has not been properly renormalized, that is the factor $(1+\chi^2)$ has not been properly absorbed into the definition of α. The coupling constant α has effectively become a function of χ and m_X. Therefore α becomes an unknown quantity that needs to be fixed by experiment. It is therefore necessary to have two measurement to solve for the two unknowns χ and α.[10]

This method is now briefly sketched. First it is assumed that there are two observables M_1 and M_2. Theoretically these are functions of α, χ^2 and m_X. For notational transparency the m_X dependence is suppressed. Therefore the two measurements can be written $M_1(\alpha, \chi^2)$ and $M_2(\alpha, \chi^2)$.

The results of these measurements are often quoted in the form

$$M_1|_{\text{exp}} - M_1|_{\text{th}} = \pm\delta M_1 \pm \Delta M_1, \quad (9.13)$$

$$M_2|_{\text{exp}} - M_2|_{\text{th}} = \pm\delta M_2 \pm \Delta M_2\,. \quad (9.14)$$

[10] Of course the variation of any extra parameter would require an extra measurement.

δM is the difference between the mean values of the theoretical and experimental values of the measurement M, and ΔM is the uncertainty in M. If $|\delta M| < \Delta M$ then the theoretical and experimental values are said to agree within errors.

Without considering a hidden photon,

$$M_1|_{\text{exp}} - M_1(\alpha_0, 0) = \pm\delta M_1 \pm \Delta M_1, \tag{9.15}$$

$$M_2|_{\text{exp}} - M_2(\alpha_0, 0) = \pm\delta M_2 \pm \Delta M_2, \tag{9.16}$$

with some value α_0 such that both δM_1 and δM_2 are small.

A hidden photon can now be added. The hidden-photon effect is small, and can be written as a perturbative expansion about $(\alpha, \chi) = (\alpha_0, 0)$. Hence

$$\frac{\partial M_1}{\partial \alpha}|_{\alpha=\alpha_0,\chi^2=0}\,\delta\alpha + \frac{\partial M_1}{\partial \chi^2}|_{\alpha=\alpha_0,\chi^2=0}\,\chi^2 = \pm\delta M_1 \pm \Delta M_1, \tag{9.17}$$

$$\frac{\partial M_2}{\partial \alpha}|_{\alpha=\alpha_0,\chi^2=0}\delta\alpha + \frac{\partial M_2}{\partial \chi^2}|_{\alpha=\alpha_0,\chi^2=0}\chi^2 = \pm\delta M_2 \pm \Delta M_2. \tag{9.18}$$

In matrix notation this linear system of equations reads

$$\begin{pmatrix} \frac{\partial M_1}{\partial \alpha}|_{\alpha=\alpha_0,\chi^2=0} & \frac{\partial M_1}{\partial \chi^2}|_{\alpha=\alpha_0,\chi^2=0} \\ \frac{\partial M_2}{\partial \alpha}|_{\alpha=\alpha_0,\chi^2=0} & \frac{\partial M_2}{\partial \chi^2}|_{\alpha=\alpha_0,\chi^2=0} \end{pmatrix} \begin{pmatrix} \delta\alpha \\ \chi^2 \end{pmatrix} = \begin{pmatrix} \pm\delta M_1 \pm \Delta M_1 \\ \pm\delta M_2 \pm \Delta M_2 \end{pmatrix}, \tag{9.19}$$

which can be solved easily

$$\begin{pmatrix} \delta\alpha \\ \chi^2 \end{pmatrix} = \begin{pmatrix} \frac{\partial M_1}{\partial \alpha}|_{\alpha=\alpha_0,\chi^2=0} & \frac{\partial M_1}{\partial \chi^2}|_{\alpha=\alpha_0,\chi^2=0} \\ \frac{\partial M_2}{\partial \alpha}|_{\alpha=\alpha_0,\chi^2=0} & \frac{\partial M_2}{\partial \chi^2}|_{\alpha=\alpha_0,\chi^2=0} \end{pmatrix}^{-1} \begin{pmatrix} \pm\delta M_1 \pm \Delta M_1 \\ \pm\delta M_2 \pm \Delta M_2 \end{pmatrix}. \tag{9.20}$$

From this it is possible to directly read off the allowed values of χ^2.

For the cases of interest it is typically sufficient to determine the derivatives $\partial M_i/\partial\alpha$, $\partial M_i/\partial\chi^2$ to leading order in α and χ^2.

This procedure corrects the behaviour of constraints for small m_X^2. This can be shown by considering a simple example where, in absence of hidden photons, both observables behave as simple power laws, $\sim \alpha^{n_1}$ and $\sim \alpha^{n_2}$,

$$M_i = M_i|_{\chi^2=0} + \delta_{\chi^2} M_i = c_i\alpha^{n_i} + c_i\alpha^{n_i}\chi^2 f_i(m_X) + O(\chi^4). \tag{9.21}$$

The term in $\delta_{\chi^2} M_i$ is the hidden-photon effect calculated in 1^{st}-order perturbation theory (Equation (9.2)) using the potential in Equation (9.1). For convenience the correction has been written with c_i and χ^2 factored out, with the remaining factor represented by a function $f_i(m_X)$.

From Equation (9.1) it can be seen that $\delta V(r)$ term dies off at large m_X. Hence the function $f_i(m_X) \to 0$ as $m_X \to \infty$. However, the perturbation actually grows towards smaller masses, and $f_i(m_X)$ tends to a constant limit. Before addition of the hidden photon the Coulomb potential can be written as

$$V_0(r) = -\frac{Z\alpha}{r}\,. \tag{9.22}$$

After the hidden photon is added,

$$V(r) = -\frac{Z\alpha}{r}(1+\chi^2)\,, \tag{9.23}$$

where the limit $m_X \to 0$ has been taken. Hence the fine-structure constant has essentially been redefined

$$\alpha \to \alpha\,(1+\chi^2). \tag{9.24}$$

Therefore, for $m_X \to 0$, there is an alternative way to obtain the perturbation. It is possible to simply insert the redefined α into the unperturbed expression,

$$M_i = c_i\alpha^{n_i} + n_i c_i \alpha^{n_i}\chi^2 + O(\chi^4)\,. \tag{9.25}$$

Comparing (9.21) with (9.25) it can be seen that $f_i(m_X) \to n_i$ as $m_X \to 0$.

Inserting (9.21) into the general expression (9.20),

$$\chi^2 = \frac{\frac{n_1(\pm\delta M_2 \pm \Delta M_2)}{M_2(\alpha_0,0)} - \frac{n_2(\pm\delta M_1 \pm \Delta M_1)}{M_1(\alpha_0,0)}}{(n_1 f_2(m_X) - n_2 f_1(m_X))}\,. \tag{9.26}$$

For conservative and robust constraints the the maximum value of χ^2 is used,

$$\chi^2 \gtrsim \frac{\frac{n_1|\Delta M_2|}{M_2} + \frac{n_2|\Delta M_1|}{M_1}}{|(n_1 f_2(m_X) - n_2 f_1(m_X))|}\,. \tag{9.27}$$

where $|\Delta M|$ is defined in (9.5). Constraints from transitions in atomic hydrogen and muonic hydrogen use $|\widetilde{\Delta M}|$ defined in (9.6).

The high-mass and low-mass behaviour is as follows,

- $m_X \to \infty$:

  Here $f_1(m_X), f_2(m_X) \to 0$ so the constraint dies off.

  More specifically it is found that the functions $f(m_X)$ decay as $m_X^{-2(1+l)}$ at for large m_X, where l is the lowest value of the angular momentum involved in the transition. A $2\,s - 2\,p$ transition therefore has $l = 0$ and a $3\,p - 3\,d$ transition has $l = 1$ etc. Hence in the limit $m_X \to 0$

$$\chi \sim m_X^{(1+l)}\,. \tag{9.28}$$

The high-mass decay described by Equation (9.28) must be considered carefully. It is conceivable that this could be modified by the effects of finite-nuclear size, but this is shown not to be the case in Appendix D. This result is particularly important for the KK model, which requires summation over high-mass modes.

- $m_X \to 0$:
  Here $f_1(m_X) \to n_1, f_2(m_X) \to n_2$ so the denominator tends to zero. Again the upper limit on χ^2 increases and the constraint dies off.

Therefore the expected behaviour is obtained in the limits $m_X \to 0$ and $m_X \to \infty$.

In renormalized constraints, and unless otherwise stated, M_1 is always taken to be the $2\,s_{1/2} - 8\,s_{1/2}$ transition in atomic hydrogen, simply because it is experimentally measured to a high precision of 3×10^{-11} eV [71]. This is similar to the theoretical error of 4.5×10^{-11} eV from R_∞ and 5×10^{-11} eV from the Lamb shift of the $2\,s_{1/2}$ state. Added together with the $\Delta M(r_p)$ contribution gives an overall uncertainty of $\widetilde{\Delta M_1} = 2 \times 10^{-10}$ eV.

A properly-renormalized constraint can therefore be obtained by taking M_2 to be the $1\,s_{1/2} - 2\,s_{1/2}$ transition in atomic hydrogen. Figure 6 shows the correctly renormalized $1\,s_{1/2} - 2\,s_{1/2}$ constraints (green) versus the naïve constraint (red).

In the renormalized method the measurements themselves do not need to be from atomic spectra. The same technique works for any process which is affected by the hidden photon. Indeed in Chapter 10.1 the method is used to produce properly-renormalized constraints by combining the anomalous magnetic moments of the electron and muon.

However the full renormalization method is actually not necessary for the $2\,s_{1/2} - 2\,p_{1/2}$ Lamb-shift constraint - it has already been shown that the naïve method produces a constraint with the proper low-mass decay (the blue curve in Figure 6). This is because in the limit $m_X \to 0$ the electromagnetic potential behaves as a perfect Coulomb's law (see Equation (9.23)). However for a perfect Coulomb's law the energies of $2\,s_{1/2}$ and the $2\,p_{1/2}$ are degenerate. Therefore, to leading order, the addition of a term of the Coulomb's law form does not produce an energy shift between the two states. This is true for all same-n

transitions.

Therefore the renormalization procedure works trivially for same-n transitions. Considering just one measurement M, and noting that the 0^{th}-order energy vanishes,

$$M = c\alpha^2\chi^2 f_2(m_X) + O(\chi^4). \tag{9.29}$$

$M \propto \chi^2$, so that $\delta\alpha$ corrections obtained from a second measurement would produce negligible terms of $\mathrm{O}(\chi^4)$. Therefore information from the second measurement is suppressed. This means that it is possible to form properly-renormalized constraints for same-n transitions using only one measurement M and with only one error ΔM (or $\widetilde{\Delta M}$).

9.1.4 New constraints

The first atomic system considered is ordinary atomic hydrogen. The constraints from $2\,s_{1/2}-2\,p_{1/2}$ (blue) and the properly-renormalized $1\,s_{1/2}-2\,s_{1/2}$ constraint (green) are shown in Figure 6. Neither of these penetrate new parameter space for hidden photons. However these constraints do constitute the best pure tests of Coulomb's law in this region of parameter space.

So far all considered transitions have involved the $1\,s_{1/2}$ or $2\,s_{1/2}$ states. These have Lamb shifts with high-theoretical uncertainty due to finite-nuclear-size effects. This is because the 0^{th}-order wavefunctions for s states are non-zero at the origin and therefore penetrate the nucleus deeply, leading to large uncertainties from finite-nuclear-size effects. This is also true for s states with $n > 2$.

States with $l > 0$ have 0^{th}-order wavefunctions which are zero at the origin and therefore have a small overlap with the nucleus. This means that the Lamb-shift uncertainties are small. Therefore same-n transitions between states with $l > 0$ (for example $3\,p_{3/2}-3\,d_{3/2}$) have extremely small theoretical uncertainties. Unfortunately, these kinds of excited states are unstable and the experimental measurements have large uncertainties. Furthermore the constraints in these transitions decay more quickly with energy (see Equation (9.28)), dying off well before new parameter space is reached. Therefore, barring significant technological advances, transitions between states with $l > 0$ are not very useful for constraining χ.

The $2\,s_{1/2} - 2\,p_{1/2}$ Lamb-shift constraint for atomic hydrogen almost penetrates the unknown region. This motivates examination of hydrogenic ions with $Z > 1$. The advantage here is that the characteristic energy of transitions scales as Z, so for higher values of Z constraints move towards the right and towards the unexplored region. The disadvantage is the higher theoretical uncertainties involved. This is due to an increase in the size of the nucleus, as well as a decrease in the Bohr radius (which scales as $1/Z$ and gives the characteristic length scale of the electron orbit). Unfortunately, this also causes the electron to penetrate the nucleus more deeply, which results in larger theoretical uncertainties from finite-nuclear-size effects. Constraints then move upwards and away from the unexplored region. If the advantages outweigh the disadvantages, then stronger constraints may be obtained. It is therefore sensible to investigate constraints for different $Z > 1$.

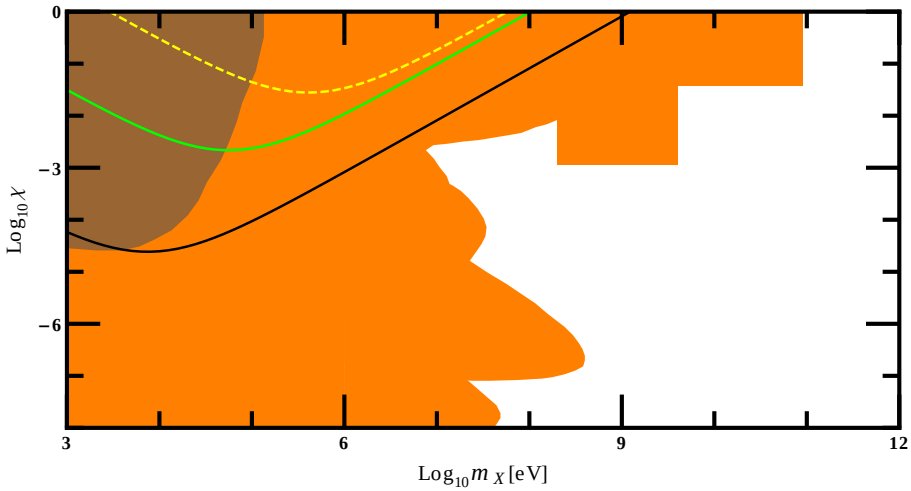

Figure 7: Non-KK constraints from the $2\,s_{1/2} - 2\,p_{1/2}$ transition in hydrogenic ions with $Z = 2$ (black), $Z = 15$ (green), and $Z = 110$ (yellow, dashed). At the 2 ΔM level the uncertainties are 3×10^{-9} eV [63], 6×10^{-4} eV [72, 73] and 8 eV [73] respectively. Note that the $Z = 110$ curve uses only the uncertainty from the theoretical calculation, but that no experimental data for the transition exists. The constraint is therefore an optimistic, speculative one, and is therefore represented by a dashed line. It can be seen that, as Z increases, constraints move away from the unexplored region and therefore become less useful.

Drake et al. [63] find experimental and theoretical errors for the $Z = 2$ helium ion $2\,s_{1/2} - 2\,p_{1/2}$ transition of 0.16 MHz and 0.2 MHz respectively, giving $\Delta M = 1.5 \times 10^{-9}$ eV.[11] The resulting constraint is shown as the black curve in Figure 7. For $Z = 15$ the experimental [72] and theoretical errors [73] combine to give a value of $\Delta M = 3 \times 10^{-4}$ eV. The resulting constraint is shown as the green curve in Figure 7. Finally $Z = 110$ is considered. This is the largest value of Z for which data is available. Johnson and Soff [73] find a theoretical uncertainty of ~ 4 eV. No experimental data for this transition exists. However accounting for experimental errors would cause the constraint to weaken. It is therefore only possible to derive an optimistic, speculative constraint. The estimated sensitivity shown as the dashed-yellow curve in Figure 7. The curve may be an optimistic one, but it is still adequate to demonstrate the requisite trend.

It can be seen that as Z increases constraints move up and away from the untested region, therefore becoming weaker. This trend[12] should be similar for other possible transitions in $Z > 1$ hydrogenic ions. Therefore $Z > 1$ transitions are generally not useful.

Exotic atoms are now considered. These systems have certain advantages over atomic hydrogen:

- Pure-QED systems like muonium and positronium may have smaller fractional theoretical uncertainties, as all experimental data is consistent with pointlike leptons [74]. Therefore is it appropriate to assume a pointlike nucleus. This eliminates the major source of theoretical uncertainty;
- Most exotic atoms have larger reduced masses than atomic hydrogen, shifting constraints to higher energies and towards the untested region;

[11] Remember that for atoms without a proton nucleus the current measurement of nuclear charge radii are consistent. Therefore the uncertainty is given by ΔM (Equation (9.5)) and not $\widetilde{\Delta M}$ (Equation (9.6)).

[12] Note that, because of the increase in the uncertainty of the Lamb shift in atomic hydrogen caused by the inconsistent values of the proton radius, the constraint from hydrogen-like helium is actually slightly better than the one from atomic hydrogen. This causes a slight anomaly in the trend. However as soon as the inconsistency in r_p is clarified, the anomaly should be solved, and the trend should hold completely.

Disadvantages:

- Higher-mass systems often have larger theoretical uncertainty (leptonic systems excluded). This is because the larger reduced mass results in a smaller Bohr radius of the system. Bound-state orbits then penetrate the nucleus more deeply, which then leads to larger corrections due to finite-nuclear-size effects;
- Similarly, hadronic atoms and atoms with $Z > 1$ have larger nuclei than atomic hydrogen, again causing larger finite-nuclear-size effects;
- Hadronic orbiting particles also interact with the nucleus via the strong interaction, which causes huge theoretical and experimental uncertainties. Therefore hadronic atoms do not produce strong constraints, but they are briefly reviewed for completeness;

Leptonic atoms are considered first. Positronium is not useful as the reduced mass is actually smaller than that of atomic hydrogen, and the uncertainties are much higher. For example the $1\,s - 2\,s$ and $2\,s - 2\,p$ transitions are limited by large experimental uncertainties, which are caused by complications such as annihilation [75–77]. The uncertainties are around two orders larger, which leads to a constraint which is around one order of magnitude weaker in χ than the ones from atomic hydrogen.

Ordinary muonium ($\mu^+\,e^-$) and true muonium ($\mu^+\,\mu^-$) are more interesting.

Experimental results have already been produced for the $1\,s_{1/2} - 2\,s_{1/2}$ and $2\,s_{1/2} - 2\,p_{1/2}$ transitions in ordinary muonium, but the resulting constraints do not improve on atomic hydrogen. The reduced mass of ordinary muonium is almost the same (in fact slightly smaller) than atomic hydrogen, so better constraints can only be obtained if uncertainties are reduced. However the $1\,s_{1/2} - 2\,s_{1/2}$ transition suffers from large theoretical errors associated with the effective Rydberg constant (see Equation (9.4)). This produces a fractional error larger than that of atomic hydrogen and consequently a weaker constraint. The $2\,s_{1/2} - 2\,p_{1/2}$ transition suffers from no such 0^{th}-order uncertainties, and indeed the theoretical uncertainty should be smaller than atomic hydrogen since there are no finite-nuclear-size effects. However the experimental situation is not yet very good. Only $1\,s_{1/2}$ states can be produced in large quantities, whereas the

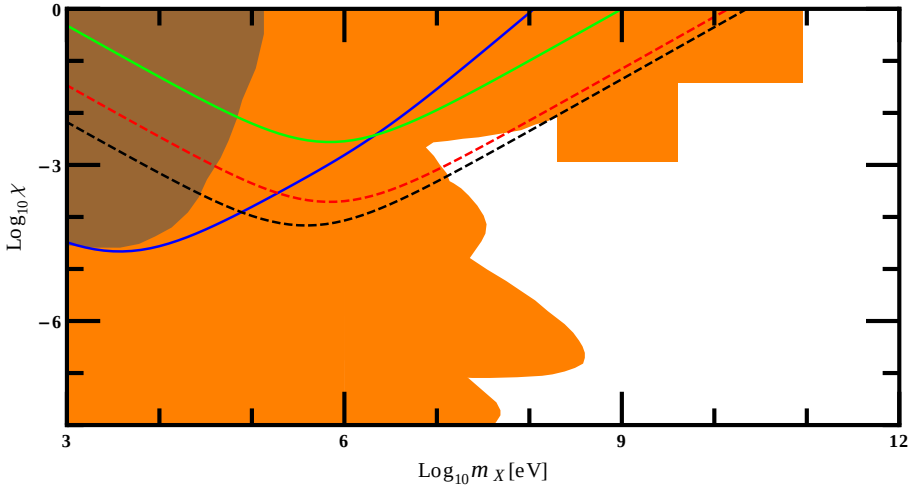

Figure 8: Non-KK constraints from muonic atoms. The dashed-black curve shows a speculative constraint from the $2\,s_{1/2} - 2\,p_{1/2}$ transition in true muonium. This is formed using only an estimate of the theoretical uncertainty of ~ 0.1 GHz (see Appendix E). If the experimental result is measured to a similar precision and agrees with theory it should be possible to form a constraint similar to this, and penetrate unexplored parameter space. The solid-green curve shows an actual constraint formed from the $2\,s^{F=1}_{1/2} - 2\,p^{F=2}_{3/2}$ transition in muonic hydrogen. There is a large theoretical error $2\,\widetilde{\Delta M} = 1.2$ meV. This is caused by the wide range of possible values of r_p that have been made possible by the recent muonic-hydrogen anomaly [64]. The dashed-red curve uses the muonic-hydrogen transition to form a speculative constraint. The error here is taken to be just the $2\,\sigma$ experimental uncertainty of 6×10^{-6} eV [64]. Finally the blue curve shows a constraint obtained by combining the measurement of the Lamb shift in ordinary hydrogen and the $2\,s^{F=1}_{1/2} - 2\,p^{F=2}_{3/2}$ transition in muonic hydrogen (see Appendix F). Using these two measurements it is not necessary to have an additional determination of the proton radius from, say, electron-scattering experiments.

production of metastable $2\,s_{1/2}$ states is much lower [78]. This means that the $2\,s_{1/2} - 2\,p_{1/2}$ transition has only been experimentally measured to a fractional precision of 1.5×10^{-2} at the $1\,\sigma$ level, leading to weak constraints.

A recent article [79] suggests that true muonium can be produced and studied in the near future. This atomic system would be extremely useful, as it has a reduced mass of around 2 orders of magnitude larger than atomic hydrogen, and theoretical errors should be low due to the absence of finite-nuclear-size effects. Since no experimental data has been produced yet, there has been no motivation for precise theoretical calculations. However it is possible to produce a rough theoretical estimate (see Appendix E) to form an optimistic, speculative constraint. This is shown as the dashed-black line in Figure 8. This is encouraging as it penetrates new parameter space. However, one still needs to obtain a consistent experimental result, and hope that the experimental error is not so large that it causes the constraint to deteriorate significantly.

Muonic atoms could also prove to be useful. The reduced mass of these systems is around 200 times larger than atomic hydrogen, shifting constraints towards larger values of m_X.

The $2\,s_{1/2}^{F=1} - 2\,p_{3/2}^{F=2}$ difference in muonic hydrogen is calculated to be [64, 66, 80–84]

$$E = -\left[209.9779(49) - 5.2262\left(\frac{r_p}{\text{fm}}\right)^2 + 0.0347\left(\frac{r_p}{\text{fm}}\right)^3\right] \text{ meV}. \tag{9.30}$$

The most precise current value of $r_p = 0.8768(69)$ fm, which is obtained from atomic spectra [62], produces a theoretical value of $E = -205.984(062)$ meV. The theoretical uncertainty alone is quite high. Moreover, the theoretical value also deviates from the recently measured experimental value of $-206.295000(3)$ meV [64] by around $5\,\sigma$. This large discrepancy is bad for producing constraints, but is a potential sign of new physics. Appendix F considers the possibility that the hidden photon could explain the anomaly. However a negative result is found.

However it is still possible to form a constraint by using the (inflated) error given in (9.6). The r_p variation increases the uncertainty to give $\widetilde{\Delta M} = 6 \times 10^{-4}$ eV. The solid-green curve in Figure 8 shows the corresponding constraint at the $2\ \widetilde{\Delta M}$ level. In the large-mass region this constraint is of comparable strength to the one from the Lamb shift in ordinary hydrogen.

It is also possible to form an optimistic, speculative constraint by considering just the experimental uncertainty. This is shown as the dashed-red curve in Figure 8. The constraint covers a similar region to the speculative constraint obtained from true muonium (dashed-black curve) and penetrates the unknown region. If an independent and sufficiently precise value of r_p is determined, which is consistent with the muonic-hydrogen extraction, then the speculative constraint could be turned into a real one. This motivates the search for more precise, independent determinations of the proton radius. However as discussed in Chapter 9.1.2 this measurement should preferably originate from measurements at relatively-high momentum transfer, in order to avoid degeneracies. At the moment the only obvious candidate process is electron scattering, although an increase in the precision by an order of magnitude may be challenging.

It can easily be shown that hadronic atoms do not produce strong constraints. The existing candidates involve the π^-, K^-, p^+, and K^- particles orbiting a proton nucleus. In each case there are significant experimental uncertainties, which completely destroy constraints. For example with pionic hydrogen the experimental strong interaction shift of the $1\,s_{1/2}$ ground state [85]

$$\epsilon_{1s} = (7.120 \pm 0.008 \pm 0.007)\ \text{eV}\,, \tag{9.31}$$

where the errors are systematic and statistical respectively. This essentially means that, for example, the $3\,p_{1/2} - 1\,s_{1/2}$ transition would have an error of at least 10 meV, which does not produce a useful constraint. All transitions in kaonic and sigmaonic hydrogen have large uncertainties due to the determination of the particle masses alone [86]. Transitions in antiprotonic hydrogen have large experimental uncertainties due to both strong interaction shifts and annihilation [87]. Furthermore it is necessary to account for large theoretical uncertainties, for example finite-size effects from both nucleus and orbiting particle. Therefore the benefits from the larger reduced masses of hadronic atoms are washed out by experimental uncertainties and quantum-chromodynamic (QCD) effects.

Overall, the strongest constraints come from atomic spectra are from the $2\,s_{1/2} - 2\,p_{1/2}$ transition in atomic hydrogen, the $2\,s_{1/2} - 2\,p_{1/2}$ in hydrogen-like helium, and the renormalized constraint which combines the $1\,s_{1/2} - 2\,s_{1/2}$ and $2\,s_{1/2} - 8\,s_{1/2}$ transitions in atomic hydrogen. These are shown together in Figure 1.

9.2 Atomic-spectral constraints for the KK model

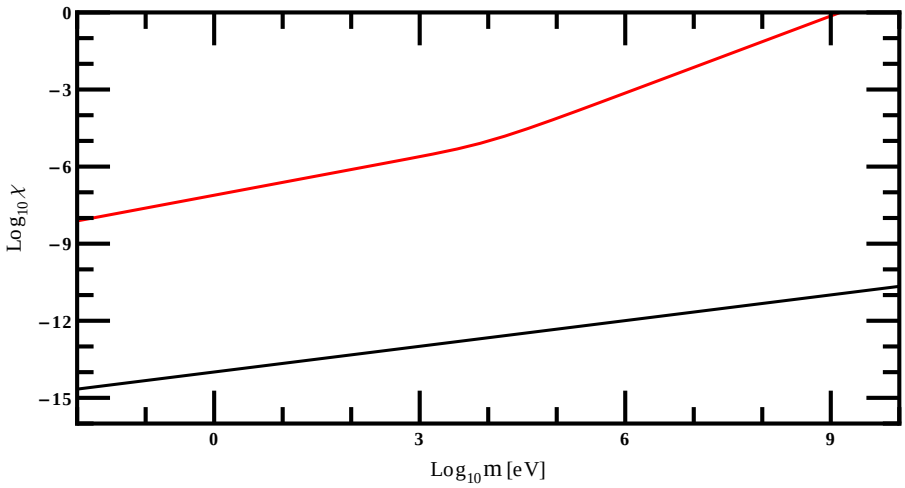

Figure 9: KK constraints from $2\,s_{1/2} - 2\,p_{1/2}$ in atomic hydrogen, for $n = 1$ extra dimensions and with the uncertainty parameter set to $a = 1$. The red curve represents a lower boundary for constrained values of χ. This is obtained by insisting that the total hidden-photon effect is larger than the uncertainty in the transition, in accordance with Equations (9.9) and (6.1). However the black curve represents an upper boundary for χ. It is obtained by insisting that the effective coupling constant (Equation 7.1) $\ll 1$, and therefore that the perturbative treatment is valid. The lower boundary is above the upper boundary, and there is therefore no constrained region of parameter space. It can easily be shown that the same result is obtained for all the considered values of $n = 1, ..., 6$ and $a = 0.1 - 1$, and therefore that no constraints are obtained in the KK model from atomic spectra. Similarly it can be shown that no constraints are obtained in the other virtual-production experiments.

The strongest constraints produced for the non-KK model cover very similar regions in parameter space. In the KK model these transitions also produce very similar constraints. Hence it is only necessary to consider updating one of these constraints to the KK model. This is chosen to be the $2\,s_{1/2} - 2\,p_{1/2}$ Lamb-shift transition in atomic hydrogen to the KK model, simply because the analytical expressions are easier to work with.

In the non-KK model the hidden-photon contribution to the Lamb shift is given by Equation (9.9). In the KK model the total hidden-photon effect is found by summing over KK modes using Equation (6.1). As explained in Appendix D, finite-nuclear-size effects do not cause any modification to the high-mass behaviour in Equation (9.9). Hence the contribution of each hidden-photon KK mode goes as a power law $\sim m_k^{-q}$, where $q = 2\,(1 + l)$, and where l is the lowest value of angular momentum for any state in the transition. Therefore $l = 0$ and $q = 2$ for the $2\,s_{1/2} - 2\,p_{1/2}$ transition.

It will be helpful to first consider specific values of n and the uncertainty parameter a, which will be taken as $n = 1$ and $a = 1$. This situation is shown in Figure 9. The red curve represents a lower boundary for constrained values of χ. This is obtained by insisting that the total hidden-photon effect is larger than the uncertainty in the transition, in accordance with Equations (9.9) and (6.1). However the black curve represents an upper boundary for χ. It is obtained by insisting that the effective coupling constant (Equation 7.1) $\ll 1$, and therefore that the perturbative treatment is valid. The lower boundary is above the upper boundary, and there is therefore no constrained region of parameter space. It can easily be shown that the same result is obtained for all the considered values of $n = 1, ..., 6$ and $a = 0.1 - 1$, and therefore that no constraints are obtained in the KK model from atomic spectra.

Similarly it will be shown that no constraints are obtained in the other virtual-production experiments.

9.3 Summary of Chapter 9

The hidden photon modifies the electromagnetic Coulomb potential by the addition of a Yukawa-like term. This causes deviations to the QED predictions for atomic spectra. These deviations are calculated in 1^{st}-order quantum-mechanical perturbation theory. Constraints are obtained by demanding that the hidden-photon effect is larger than the uncertainty in a given transition.

The total uncertainty is defined as the addition of the absolute values of the theoretical and experimental uncertainties. For non-hydrogenic atoms this is given by Equation (9.5). For hydrogenic atoms it is necessary to include an extra term which accounts for the discrepancy between measurements of the

proton radius [64]. The total uncertainty is then given by Equation (9.5).

A distinction is drawn between two types of transitions; same-n transitions and different-n transitions.

Constraints are first produced using a naïve method. In the non-KK model, same-n transitions produce constraints which decay properly as $m_X \to 0$. However for different-n transition the naïve method produces incorrectly shaped constraints. These do not decay properly in the limit $m_X \to 0$, but instead saturate.

This is remedied by using a renormalized method, which combines two atomic spectra for each constraint. This constraint decays properly in the limit $m_X \to 0$. This renormalized method is not just confined to atomic spectra. Indeed in Chapter 10.1 it is used to form a properly-renormalized constraint which combines the anomalous magnetic moments of the electron and muon, and decays properly in the limit $m_X \to 0$.

It is possible to produce constraints from atomic spectra in a wide range of atoms. The strongest ones are from the $2\,s_{1/2} - 2\,p_{1/2}$ Lamb shift in atomic hydrogen, the renormalized constraint which combines the $1\,s_{1/2} - 2\,s_{1/2}$ and $2\,s_{1/2} - 8\,s_{1/2}$ transitions in atomic hydrogen, and the $2\,s_{1/2} - 2\,p_{1/2}$ Lamb shift in hydrogen-like helium ions. These constraints all cover very similar regions of parameter space, and are plotted together in Figure 1.

The KK model is then considered. The strongest constraints from the non-KK model are all very similar. These will produce very similar constraints in the KK model. It is therefore sufficient to update the constraints from only one transition. This is chosen to be the $2\,s_{1/2} - 2\,p_{1/2}$ Lamb shift in atomic hydrogen, since the analytical expressions are easier to work with.

However it is found that no constraints are actually obtained for the KK model. This is because constraints have both a lower boundary and upper boundary in χ. The lower boundary is obtained by insisting that the total hidden-photon effect is larger than the uncertainty in the transition. The upper boundary is obtained by insisting that the effective coupling constant (Equation 7.1) $\ll 1$, and therefore that the perturbative treatment is valid. The lower boundary always occurs above the upper boundary, and there is therefore no constrained region of parameter space. Similarly it will be shown that no

constraints are obtained in the other virtual-production experiments.

10 $a_{e,\mu}$ constraints

At the classical level the magnetic moment of every SM fermion in given by $g = 2$. The first quantum, or "anomalous" correction occurs at the one-loop level in quantum electrodynamics (QED). The contributing Feynman diagram is shown in Figure 10 b).

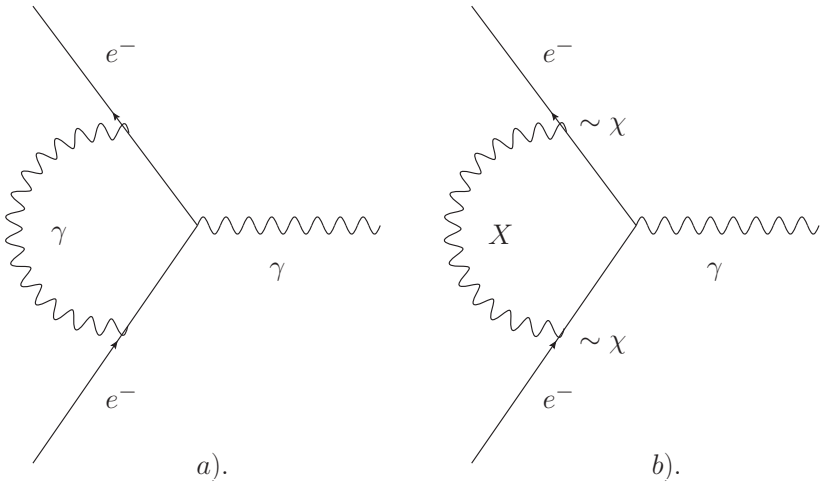

Figure 10: The leading-order Feynman diagrams for the anomalous magnetic moment of the electron. The Feynman diagrams for anomalous magnetic moment of other SM fermions f^- are found trivially by substituting $e^- \to f^-$. The SM-photon contribution is shown in a) The hidden-photon contribution is shown in b). The factors of χ in the hidden-photon contribution have been highlighted.

The QED prediction and the best experimental value for a_e are extremely close. In contrast there is a significant discrepancy between the QED prediction for a_μ and the best experimental value [88, 89]. This is a potential sign of BSM physics, and in Chapter 10.1.1 it is shown that there is a region of parameter space in which the hidden photon could account for this discrepancy [4, 90].

In Chapter 10.1 a_e and a_μ are separately used to derive constraints on the hidden photon, reproducing the results from [4,90]. These constraints are similar to the naïve constraints from atomic spectra in Chapter 9.1, and do not decay properly in the limit $m_X \to 0$. The renormalized method from Chapter 9.1 is

then used to combine both a_e and a_μ into one constraint, which exhibits proper high and low-mass behaviour.

10.1 $a_{e,\mu}$ constraints for the non-KK model

The starting point for the calculation is the SM-photon contribution to a_e. This is essentially found by evaluating Figure 10 a) in the non-relativistic limit and then finding the spin-dependent part. This leads to the expression [91]

$$a_e \equiv \frac{(g-2)_e}{2} = F_2(q^2=0)\,, \tag{10.1}$$

where q^2 is the momentum transfer, and the so-called form factor is given by

$$F_2(q^2) = \frac{\alpha}{2\pi}\int_0^1 dxdydz\,\delta(x+y+z-1)\left[\frac{2\,m_e^2 z(1-z)}{m_e^2(1-z)^2 - q^2xy + m_\gamma^2 z}\right] + O(\alpha^2)\,, \tag{10.2}$$

where m_γ is the SM-photon mass. In a vacuum $m_\gamma = 0$,

$$\begin{aligned} a_e &= \frac{\alpha}{2\pi}\int_0^1 dx\,dy\,dz\,\delta(x+y+z-1)\left[\frac{2\,m_e^2 z(1-z)}{m_e^2(1-z)^2}\right] + O(\alpha^2) \\ &= \frac{\alpha}{\pi}\int_0^1 dz \int_0^{1-z} \frac{z}{(1-z)} + O(\alpha^2) \\ &= \frac{\alpha}{2\pi} + O(\alpha^2)\,, \end{aligned} \tag{10.3}$$

which is the leading-order contribution to the anomalous magnetic moment of the electron.

This can be modified to give the hidden-photon effect by starting with the general Lagrangian (2.1) and then transforming to the propagation-eigenstate basis, where the X_P has mass m_X and the A_P is massless. Using Equations (2.2), (2.4), and (2.5) results in the relation $A^\mu \sim A_P^\mu + \chi X_P^\mu$. Hence the electromagnetic interaction term becomes

$$e j_\mu A^\mu \to e j_\mu \left(A_P^\mu + \chi X_P^\mu\right)\,, \tag{10.4}$$

where j^μ is any SM electromagnetic current. There are now two contributions to any electromagnetic quantity. The first involves the massless SM photon A_P. The second involves the hidden photon X_P and is suppressed by a factor $\sim \chi^2$. Hence it is possible to write

$$F_{2,X}(q^2=0) = F_2(q^2=0, m_\gamma \equiv 0) + \chi^2\, F_2(q^2=0, m_\gamma \to m_X \not\equiv 0)\,. \tag{10.5}$$

Overall

$$a_e = \frac{\alpha}{2\pi} + \chi^2 F_2(q^2 = 0, m_X) + O(\alpha^2)\,, \tag{10.6}$$

where

$$F_2(q^2 = 0, m_X) = \frac{\alpha}{\pi}\int_0^1 dz \left(\frac{m_e^2\, z\,(1-z)^2}{m_e^2(1-z)^2 + z\, m_X^2}\right)\,. \tag{10.7}$$

A constraint can be obtained by imposing that the hidden-photon contribution to a_e is larger than the uncertainty in a_e [4]. This uncertainty is defined by Equation (9.5). The most recent experimental value comes from a cyclotron experiment, $a_e = 159652180.73(0.28) \times 10^{-12}$ [92, 93]. Currently the best theoretical value is $1159652181.78(77) \times 10^{-12}$ [94].

The first measurement or "M_1" is taken to be a_e. Therefore Equation (9.5) gives $\Delta M_1 = 8.4 \times 10^{-12}$ at the $1\,\sigma$ level. Using the notation of Equations (9.13) - (9.16) gives $|\delta M_1| = 2.06 \times 10^{-12}$. Since $\delta M_1 < \Delta M_1$ the theoretical and experimental values for this measurement are consistent. Hence the error for this measurement can just be taken as $\Delta M_1 = 8.4 \times 10^{-12}$. The constraint is the red curve shown in Figure 11, and uses an uncertainty of $2\,\Delta M_1$. Like the naïve single transition constraints in Chapter 9.1, this does not decay properly in the limit $m_X \to 0$. This can be understood by inspecting Equation (10.7), where the hidden-photon effect saturates for small m_X.

In the same fashion it is possible to form a naïve, non-renormalized constraint using a_μ [4]. Therefore the second measurement or "M_2" is taken to be a_μ. The uncertainty for this quantity is again defined by Equation (9.5). The most recent experimental value of a_μ is $11659208.0(6.3) \times 10^{-10}$ [88, 89]. The most recent theoretical value is $11659180.4(5.1) \times 10^{-10}$ [89]. Using Equation (9.5) gives $\Delta M_2 = 22.8 \times 10^{-10}$ at the $1\,\sigma$ level. However $|\delta M_2| = 55.2 \times 10^{-10}$, meaning that $|\delta M_2|/\Delta M_2 \sim 2.4\,\sigma$.[13] Therefore the QED and experimental values are not consistent for a_μ. This is a potential sign of BSM physics. However it also means that it is *not* appropriate to just use ΔM_2 as the error for this transition. Instead the error is taken to be $|\delta M_2| = 55.2 \times 10^{-10}$.

[13] It is often claimed that the experimental and theoretical values differ by $3.4\,\sigma$, for example in [89]. This is true if ΔM_2 is calculated by adding the experimental and theoretical errors in quadrature. However in (9.5) the absolute values of the experimental and theoretical errors are added together.

The hidden-photon contribution to a_μ is given by Equations (10.6) and (10.7) only with $m_e \to m_\mu$. A constraint is obtained by imposing that this is larger than $2\,|\delta M_2|$. This is shown as the blue curve in Figure 11. Again this constraint does not decay properly in the limit $m_X \to 0$, but does behave properly in the high-mass region.

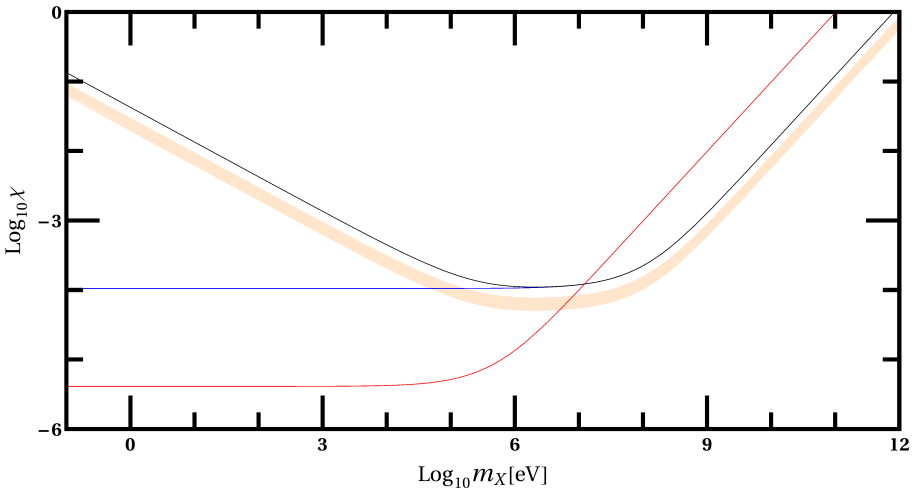

Figure 11: Constraints from a_e and a_μ in the non-KK model. The red curve is the naïve constraint using only a_e, which does not decay properly in the limit $m_X \to 0$. The blue curve is the naïve constraint using only a_μ, which also does not decay properly in the limit $m_X \to 0$. The black curve is the renormalized constraint which combines both a_e and a_μ, and decays properly in the limit $m_X \to 0$. The light-orange band is the region in which the hidden photon could be used to solve the a_μ anomaly.

It could be argued that the lack of proper low-mass decay of these naïve constraints is not important, as in this region the constraints from other experiments dominate. The naïve constraints behave properly in the important high-mass region $m_X \gtrsim m_e$. Nevertheless the renormalization method is used to produce a constraint with the proper low-mass behaviour. This is obtained by using (9.27) with $M_1 = a_e$ and $M_2 = a_\mu$ and uses errors at the 2 ΔM_1 and 2 δM_2 level. It is shown as the black constraint in Figure 11.

10.1.1 Hidden photon as a solution to the a_μ discrepancy

There is a region of parameter space in which the hidden photon could resolve the discrepancy between theory and experiment for a_μ [4].

The renormalized method can be used to find this region. First it must be demanded that the hidden-photon effect is large enough to explain the a_μ discrepancy, and therefore must be $\gtrsim 1 \times \Delta M_2$. However the hidden-photon effect must not be larger than the discrepancy, and therefore must be $\lesssim \delta M_2 \sim 2.4 \times \Delta M_2$. The uncertainty of a_e is taken to be $\sim 1 \times \Delta M_1 = 8.4 \times 10^{-12}$. This produces the light-orange band of parameter space in Figure 11. This is also shown as the light-orange "a_μ band" in Figure 1.

10.2 $a_{e,\mu}$ constraints for the KK model

First it should be noted that production is virtual, and therefore that KK decays are not important. However production is at loop-level effect so the hidden-photon effect dies slowly at high masses, specifically m_k^{-2} (see Equation (10.3)). Therefore it is generally necessary to introduce an UV cutoff $M_c = aM_*$, where a is the uncertainty parameter (see in Chapter 6.2).

Constraints are obtained by using the renormalized method with $M_1 = a_e$ and $M_2 = a_\mu$, and summing over KK modes. Errors are at the 2 ΔM_1 and 2 δM_2 level.

In similar fashion to to the atomic-spectral case it will be helpful to first consider specific values of n and the uncertainty parameter a, which will be taken as $n = 1$ and $a = 1$. This situation is shown in Figure 12. The red curve represents a lower boundary for constrained values of χ. This is obtained by insisting that the total hidden-photon effect is larger than the uncertainties in a_e and a_μ, in accordance with Equations (10.6), (10.7), and (6.1). However the black curve represents an upper boundary for χ. It is obtained by insisting that the effective coupling constant (Equation 7.1) $\ll 1$, and therefore that the perturbative treatment is valid. The lower boundary is above the upper boundary, and there is therefore no constrained region of parameter space. It can easily be shown that the same result is obtained for all the considered values of $n = 1, ..., 6$ and $a = 0.1 - 1$, and therefore that no constraints are obtained in the KK model from $a_{e,\mu}$. This is of course the same result that was obtained

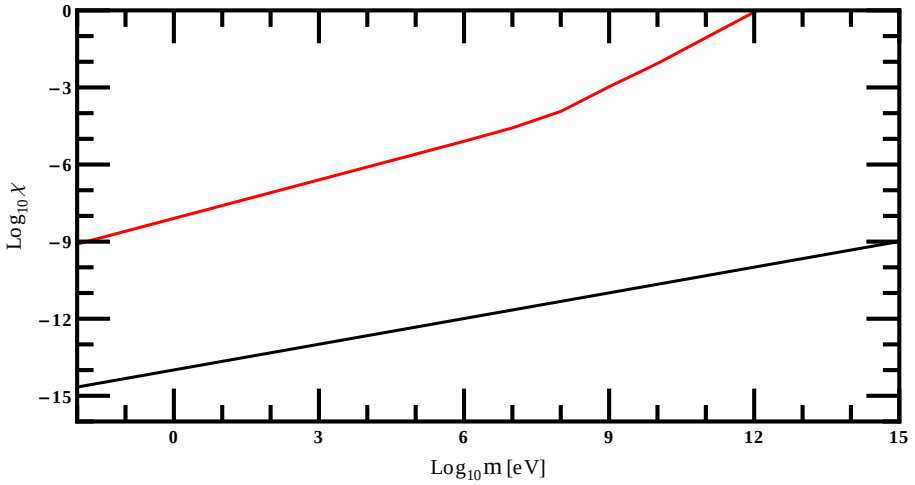

Figure 12: Constraints for the KK model from a_e and a_μ. This uses the properly-renormalized method described in Chapter 9.1, which combines both quantities. The red curve represents a lower boundary for constrained values of χ. This is obtained by insisting that the total hidden-photon effect is larger than the uncertainties in a_e and a_μ, in accordance with Equations (10.6), (10.7), and (6.1). However the black curve represents an upper boundary for χ. It is obtained by insisting that the effective coupling constant (Equation 7.1) $\ll 1$, and therefore that the perturbative treatment is valid. The lower boundary is above the upper boundary, and there is therefore no constrained region of parameter space. It can easily be shown that the same result is obtained for all the considered values of $n = 1, ..., 6$ and $a = 0.1 - 1$, and therefore that no constraints are obtained in the KK model from $a_{e,\mu}$. This is the same result that was obtained from atomic spectra in Chapter 9.2.

from atomic spectra in Chapter 9.2.

10.3 Summary of Chapter 10

The anomalous magnetic moment of SM fermions is calculated in QED. The QED prediction for a_e agrees very closely with the most recent experimental value. However for a_μ there is large discrepancy between QED and experiment [88, 89].

A constraint is obtained by imposing that the hidden-photon contribution to a_e is larger than the uncertainty in a_e [4], where the uncertainty is defined by Equation (9.5). The constraint is shown as the red curve in Figure 11. It does not decay properly in the limit $m_X \to 0$ but instead saturates, in a similar fashion to the naïve atomic-spectral constraints from Chapter 9.1. A similar constraint is obtained from a_μ, and is shown as the blue curve in Figure 11. Again this constraint does not decay properly in the limit $m_X \to 0$, but instead saturates.

It is also possible to combine both a_e and a_μ using the renormalization method from Chapter 9.1. This produces a constraint which decays properly in the limit $m_X \to 0$. This is denoted as the $a_{e,\mu}$ constraint, and is shown as the black curve in Figure 11.

The hidden photon could be used to solve the a_μ anomaly, provided that it lies in a narrow band of parameter space. This is shown as the light-orange band in Figure 11.

Similarly to the atomic-spectral case, it is not possible to use $a_{e,\mu}$ to produce constraints in the KK model. This is because if the total hidden-photon effect is large enough to be observed, then the effective perturbative coupling becomes so large that the perturbative treatment breaks down. This is generally true for virtual-production experiments.

11 Fixed-target constraints

Fixed-target experiments essentially involve firing an electron beam at a stationary target material. Hidden photons are then emitted through bremsstrahlung as the electron scatters off the positive ions in the material (diagrams (a) in Figure 13). The basic idea is that this hidden photon should decay to an e^+e^- pair, which is then detected. Lack of observation of such final-state particles constrains the hidden photon [38].

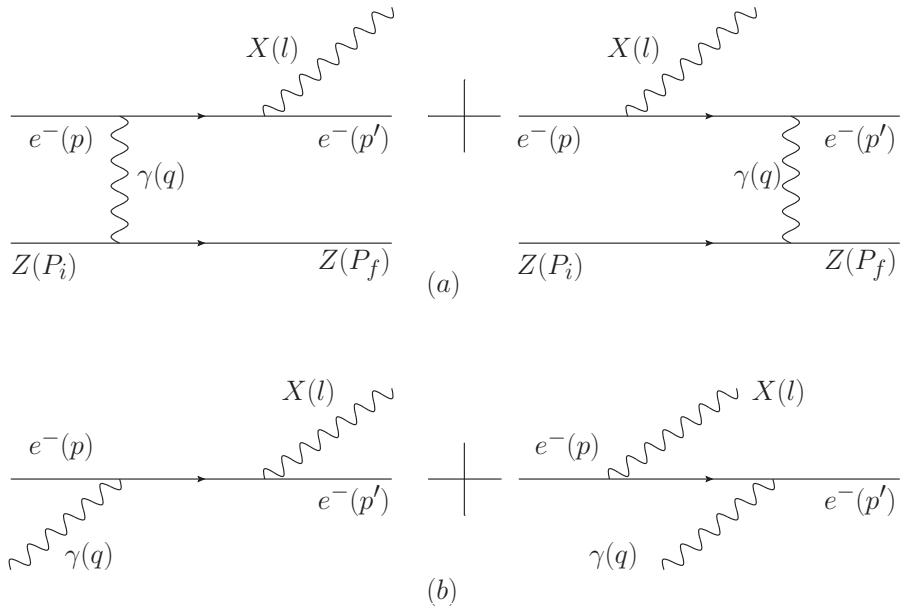

Figure 13: The top two diagrams (a) show the bremsstrahlung production process for fixed-target experiments. In Equation (11.3) the Weizsäcker-Williams approximation [95–97] is used to relate this to the simpler cross section for Compton-like hidden-photon production (b).

In all considered experiments the targets are "thick". This means the target material is of several radiations lengths, where a high-energy electron loses e^{-1} of its energy on passing through one radiation length [86].

The distance traversed beyond the front of the target is measured by the coordinate z (see Figure 14). The produced hidden photons need to decay after an initial length such that $z > l$, where l includes the target length and a shielded region. It also has to decay before the detector, which requires $z < L$.

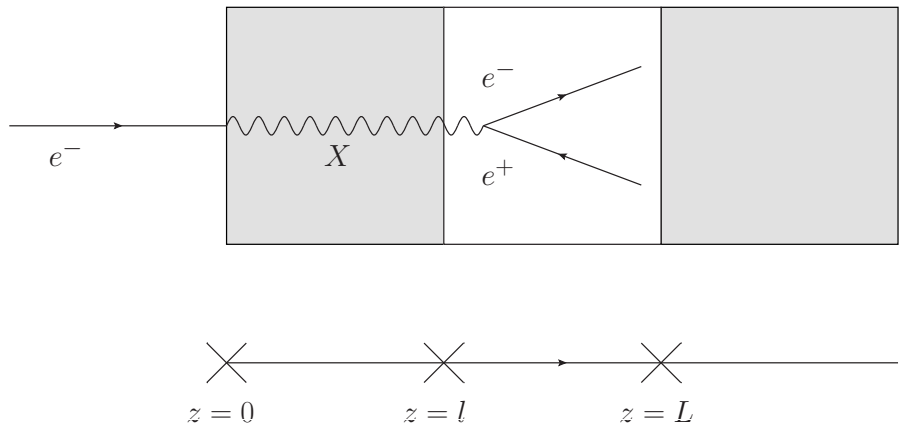

Figure 14: Schematic diagram of the fixed-target experimental setup. $z < l$ is the target plus the shielded region. For detection the hidden photon must decay in the region $l < z < L$. The region $z > L$ is beyond the detector.

11.1 Fixed-target constraints for the non-KK model

The differential form of the production cross section for the bremsstrahlung process in Figure 13 a) is given by

$$\frac{d\sigma\left(e^-(p) + Z(P_i) \to e^-(p') + X(l) + Z(P_f)\right)}{dE_X\, d\cos\theta_X}\,, \tag{11.1}$$

where in the lab frame $P_i = (M_i, \vec{0})$, and θ_X is the angle between the incoming electron beam and the outgoing hidden photon.

The Weizsäcker-Williams approximation [95–97] can then be used to relate the full cross section to the simpler hidden-photon Compton-scattering process,

$$e^-(p) + \gamma(q) \to e^-(p') + X(l)\,, \tag{11.2}$$

with $q = P_i - P_f$. This Compton-scattering cross section is shown in diagrams (b) in Figure 13. Therefore

$$\frac{d\sigma\big(e^-(p) + Z(P_i) \to e^-(p') + X(l) + Z(P_f)\big)}{dE_X\, d\cos\theta_X}$$

$$\sim \left[\left(\frac{\alpha f}{\pi}\right)\left(\frac{E_0 x\beta}{(1-x)}\right)\left(\frac{d\sigma\big(e^-(p) + \gamma(q) \to e^-(p') + X(l)\big)}{d(p\cdot l)}\right)\right]\Bigg|_{t_r\,=\,t_{r,min}}\,, \tag{11.3}$$

where $t_r = -q^2$ is the momentum transfer, and $\beta = \sqrt{1 - m_X^2/E_0^2}$.

The Equation (11.3) must be examined more closely. The left hand side is the differential cross section for the full process, which involves all initial and final-state particles. This involves all values of momentum transfer $t_{r,min} \leq t_r \leq t_{r,max}$. However on the right hand side the differential cross section is evaluated only at $t_{r,min}$. The dependence on the full range of t_r is now contained inside a flux factor f, which represents the effective flux of virtual SM-photons which are exchanged in the bremsstrahlung process. This is given by

$$f \equiv \int_{t_{r,min}}^{t_{r,max}} dt_r \times \frac{(t_r - t_{r,min})}{t_r^2} \times G_2(t_r)\,. \tag{11.4}$$

$G_2(t_r)$ is a general electric form factor,[14] which can be written as

$$G_2(t) = \underbrace{\left(\frac{a^2 t}{1+a^2 t}\right)^2 \left(\frac{1}{1+t/d}\right)^2 Z^2}_{G_{2,el}(t)} + \underbrace{\left(\frac{a'^2 t}{1+a'^2 t}\right)^2 \left(\frac{1+(t/4m_p^2)(\mu_p^2-1)}{(1+(t/0.71\,\mathrm{GeV})^2)^4}\right)^2 Z}_{G_{2,in}(t)}, \tag{11.5}$$

where

$$a = 111 Z^{-1/3} m_e^{-1}, a' = 773\, Z^{-2/3} m_e^{-1}, d = 0.164(\mathrm{GeV})^2 A^{-2/3}, \mu_p = 2.79. \tag{11.6}$$

Both terms comprise an atomic form factor, multiplied by a nuclear form factor [38, 95].

In Appendix G.1 the cross section is discussed in more detail, as well as finding expressions for $t_{r,min}$ and $t_{r,max}$.

The number of detected e^+e^- pairs N is given by

$$\frac{dN}{dxdz} = N_e \left(\frac{N_0 X_0}{A}\right) \int_{E_X}^{E_0} dE_1 \int_0^W dw\, I(E_1; E_0, w) \left(\frac{E_0}{E_1}\frac{d\sigma}{dx'}\right)\Bigg|_{x'=\frac{E_X}{E_1}} \frac{dP(z)}{dz}\,. \tag{11.7}$$

E_0 is the energy of the beam electrons. The energy fraction passed on to hidden photons is denoted x, so $E_X = xE_0$. N_0 is the Avogadro constant, X_0 is the radiation length (in g/cm^2) of the target material, A is the atomic mass, and ρ is the density. The number of radiation lengths which the electron beam has penetrated is denoted w, and W is the total number of radiation lengths of the target. E_1 is the energy of the electron beam as it passes through the target, and $I(E_1; E_0, w)$ describes the beam intensity as it passes through the material.

[14] The other form factor $G_1(t_r)$ contributes only a negligible amount in all cases of interest.

In the considered experiments $W \gg 1$, so it is possible to use the formula

$$I(E_1; E_0, w) \approx \frac{1}{E_0} y^{bw-1}\, bw\,, \tag{11.8}$$

where $y \equiv (E_0 - E_1)/E_0$ and $b = 4/3$.

Equation (11.7) can be further converted using the expression

$$\frac{N_0 X_0}{A} = \frac{m_e^2}{\alpha^3 \left(Z^2 \left[L_{rad} - f(Z)\right] + Z L'_{rad}\right)}\,, \tag{11.9}$$

where [96]

$$L_{rad} = \ln(184.15\, Z^{-\frac{1}{3}}), \quad L'_{rad} = \ln(1194\, Z^{-\frac{2}{3}}), \tag{11.10}$$

and

$$f(Z) = a_0^2(1 + a_0^2)^{-1} + 0.202 - 0.037 a_0^2 + 0.008 a_0^4 - 0.002 a_0^6 + O(a_0^8)\,, \tag{11.11}$$

where $a_0 = \alpha Z$.

The final factor in Equation (11.7) is the escape probability factor

$$\frac{dP(z)}{dz} = \frac{1}{l_0}\, e^{-\frac{z}{l_0}}\,, \tag{11.12}$$

where l_0 is the hidden-photon mean free path due to reabsorption. This reabsorption factor leads to an upper boundary for fixed-target constraints, as explained in Chapter 8.1. These upper boundaries can be seen for example in the constraints in Figure 15. As usual there are two components to this reabsorption; decay and scattering.

Scattering is only important in the non-vacuum region $z < l$. Here it is possible for the hidden photon to scatter off the target materials via the inverse of the bremsstrahlung process shown in Figure 13 a). However this scattering process is suppressed by $O(\alpha^2)$ relative to decay. Therefore it is only necessary to account for decay when calculating the hidden-photon mean free path l_0.

For the region $2\, m_e \leq m_X \leq 2\, m_\mu$ the decay $X \to e^+ + e^-$ dominates. This decay produces the detectable final-state particles. For $m_X > 2\, m_\mu$ extra decay channels become available, for example decay to $\mu^+ + \mu^-$, or final-state hadrons. In the non-KK model it is initially assumed that constraints are restricted to the region $m_X \lesssim 2\, m_\mu \sim 200$ MeV, and therefore that these extra decay channels are negligible. It will eventually be confirmed that the E141 and E774 constraints do indeed die off well before $m_X = 2\, m_\mu$ (see Figure 15), so this procedure is

self-consistent and the method is valid. The E137 constraint actually involves masses slightly larger than $2\,m_\mu$ (see Figure 15), but the overlap is small and the assumption is still valid to a reasonable approximation. Therefore only the decay to $e^+ + e^-$ is relevant, and that the mean free path is given by Equations (8.2) and (8.4). In the KK model there are contributions from KK modes with masses $m_k > 2\,m_\mu$, and it is therefore necessary to account for other decay channels, for example $X \to \mu^+ + \mu^-$ (see Chapter 11.2).

Constraints are obtained by taking Equation (11.7) and applying kinematic cuts. This means only counting contributions from final-state particles which have detectable energies and angles, and is detailed in Appendix G.2. The total number of expected e^+e^- pairs N is given by integrating over the region $l < z < L$, and the energy fraction x. A constraint is obtained by imposing that N is larger than the experimental background.

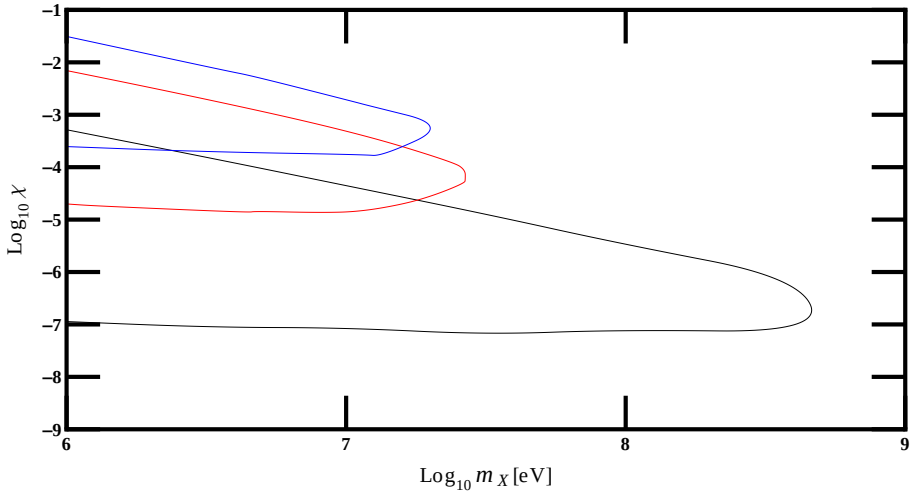

Figure 15: Summary plot of non-KK fixed-target constraints. The detected final-state particles are either electrons or positrons from the decay $X \to e^+ + e^-$. Hence the constraints only occur for $m_X > 2\,m_e$. The black curve is from E137, the red curve is from E141, and the blue curve is from E774. Each constraint contains an upper boundary. As explained in Chapter 8.1 this comes from reabsorption of the hidden photon in the shielded region of the beam dump (see Figure 14).

The strongest constraint comes from E137 at SLAC [98]. This involves sending $\sim 2 \times 10^{21}$ electrons with an initial-beam energy of $E_0 = 20$ GeV at an aluminium ($Z = 13$, $A = 27$) target. There is a shielded region of length 200 metres, so overall $l \sim 200$ metres. This is followed by an approximate vacuum region ~ 200 metres, followed by a detector with radius $r = 3$ metres. The detection system is an electromagnetic shower counter, which can detect electrons, positrons, or photons. The production of final-state SM photons is negligible. This is because in the region $l < z < L$ (see Figure 14) the hidden photon travels through an approximate vacuum, so scattering effects are not significant. Hence the detected signal is either an electron or positron. The detector requires the electron or positron to have an energy of at least $E_{crit} = 0.1 \times E_0$ for detection. This is accounted for in the kinematic cuts (see Appendix G.2).

Decay products with masses $\gg 2\,m_e$ cause a very different kind of cascade effect in the detector and can be easily distinguished from the e^+e^- signal. Therefore the effects of these higher-mass particles are easily subtracted off, and only events which could have been caused by an electron, positron or photon are counted. For the non-KK model this is not too important, as production of these higher-mass particles is negligible. However in the KK model there are effective contributions from KK modes with masses $2\,m_\mu < m_k < E_0$. Therefore there is appreciable production of these higher-mass particles. These do not contribute significantly to the observed signal, but cause a reduction to the hidden-photon mean free path.

No candidate events are observed in the experiment, and the constraint is formed by assuming a background of around 10 events. This is shown as the black curve in Figure 15. Constraints are only obtained for $m_X > 2\,m_e$, for which the decay $X \to e^+ + e^-$ is energetically possible.

The fixed-target experiment E774 at SLAC [99] is now considered. This uses 0.52×10^{10} electrons with $E_0 = 275$ GeV, and a tungsten ($Z = 74$, $A = 184$) target. In this case $l = 0.3$ metres, $L = 7.55$ metres, and $r = 0.3$ metres. The background is 17 events. The detector is again a general electromagnetic calorimeter, meaning that either a positron or electron can be detected, as long as it has energy $\geq E_{crit} = 0.1 \times E_0 = 27.5$ GeV. As in the the E137 experiment,

final-state SM-photon events are negligible, and it is possible to ignore final-state particles with masses $\geq m_\mu$. The final constraint is shown by the blue curve in Figure 15.

The final fixed-target experiment is E141 at SLAC [100]. Here 2×10^{15} electrons with $E_0 = 9$ GeV are fired at a tungsten ($X = 74$, $A = 184$) target. In this case $l = 0.22$ metres, $L = 35$ metres, and $r = 0.075$ metres. Here only a final-state positron is detected. Again this means that particles with masses $\geq m_\mu$ do not contribute to the observed signal. However these particles can reduce the mean free path of the hidden photon. This effect is negligible in the non-KK model, but is significant in the KK model. The positron must have an energy of at least $E_{crit} = 0.5 \times E_0$ to be detected. This is accounted for in the kinematic cuts (see Appendix G.2). The final constraint is obtained by imposing that the hidden-photon effect is less than the background of ~ 1000 events, and is shown as the red curve in Figure 15.

11.2 Fixed-target constraints for the KK model

As in the non-KK model, hidden-photon reabsorption is important. In Chapter 11.1 it is shown that scattering is negligible in the non-KK model. This carries over to the KK model. In the KK model there are generally contributions from KK modes with masses $2\,m_\mu < m_k < E_0$. Hence it is necessary to account for extra decay channels of the form $X \to$ SM only. As noted in Chapter 11.1, decays to final states other than $e^+ + e^-$ do not contribute significantly to the observed signal. Their only physical effect here is to reduce the hidden-photon mean free path. The total decay rate is given be approximately by that of $X \to e^+ + e^-$ multiplied by the effective number of decay channels N_{eff},

$$\Gamma_{X,\,\mathrm{total}} \sim N_{eff}\ \frac{\alpha\chi^2 m_X}{2}\,, \tag{11.13}$$

where

$$\begin{aligned} N_{eff} &= 1, & m_k \leq 2\,m_\mu, \\ N_{eff} &= 2 + R(m_k), & m_k > 2\,m_\mu\,, \end{aligned} \tag{11.14}$$

and R is the energy dependent ratio

$$R = \frac{\sigma\left(e^+ + e^- \to \text{hadrons}\right)}{\sigma\left(e^+ + e^- \to \mu^+ + \mu^-\right)}\,, \tag{11.15}$$

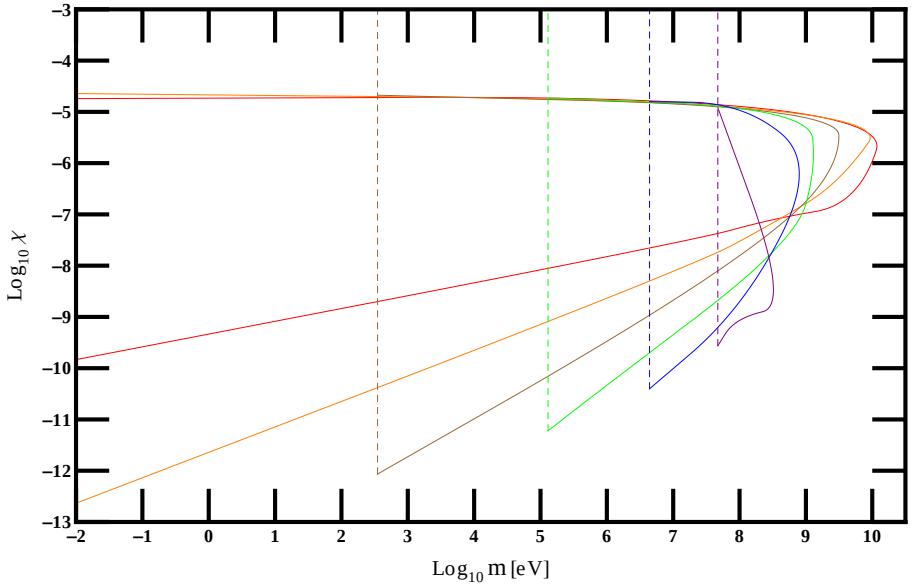

Figure 16: E137 fixed-target constraints for the KK model. The different coloured curves are for different numbers of extra dimensions; $n = 1$ (red), $n = 2$ (orange), $n = 3$ (brown), $n = 4$ (green), $n = 5$ (blue), and $n = 6$ (purple). Constraints are only produced for the ranges of m described in Table 1. Note that it is still possible to get constraints for $m \leq 2\,m_e$. This is because higher-mass KK modes with $m_k > 2\,m_e$ can still decay to a detectable e^+e^- pair.

the data for which is taken from [101]. The hidden-photon mean free path is now given by Equations (8.2) and (11.15).

The theoretical prediction for the hidden-photon effect must also be multiplied by the number of detected e^+e^- pairs by a factor of $1/N_{eff}$, to exclude the extra high-mass decay channels.

The constraints for the E137 experiment are shown in Figure 16, the E141 experiment in Figure 17, and the E774 experiment are shown in Figure 18. The different coloured curves are for different numbers of extra dimensions; $n = 1$ (red), $n = 2$ (orange), $n = 3$ (brown), $n = 4$ (green), $n = 5$ (blue), and $n = 6$ (purple). The constraints are only produced for the ranges of m described in Table 1. Note that it is still possible get constraints for $m \leq 2\,m_e$, because

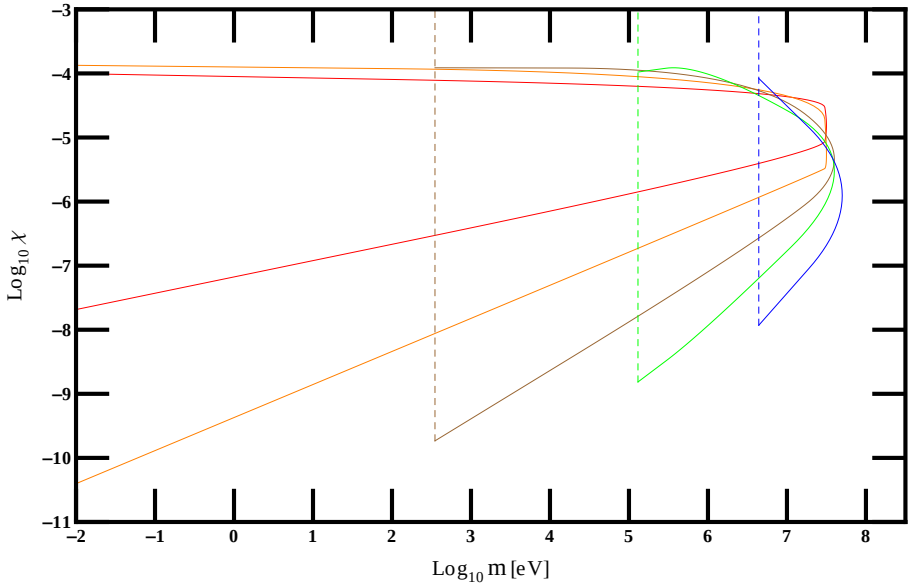

Figure 17: E141 fixed-target constraints for the KK model. The different coloured curves are for different numbers of extra dimensions; $n = 1$ (red), $n = 2$ (orange), $n = 3$ (brown), $n = 4$ (green), $n = 5$ (blue). The constraints are only produced for the ranges of m described in Table 1. There are negligible constraints for $n = 6$, and these are not plotted. Note that it is still possible to get constraints for $m \leq 2\,m_e$. This is because higher-mass KK modes with $m_k > 2\,m_e$ can still decay to a detectable e^+e^- pair.

higher KK modes with $m_k > 2\,m_e$ can still decay to a detectable e^+e^- pair.

11.3 Summary of Chapter 11

Fixed-target experiments involve firing an electron beam at a stationary target. This work only considers experiments with thick targets, that is a targets of multiple radiation lengths. Hidden photons are emitted through bremsstrahlung off the positive ions within the material. If the hidden photon escapes a shielded region and then decays to an e^+e^- pair it can be detected. Lack of observation of such e^+e^- pairs constrains the hidden photon.

The probability of a hidden photon escaping the shielded region is given by the usual escape factor e^{-l/l_0}, which results in the usual upper boundary for

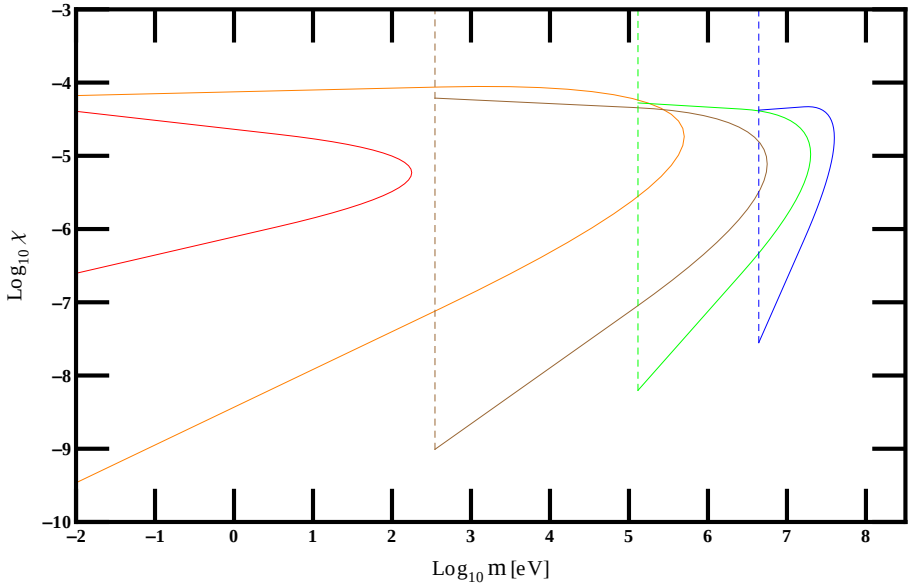

Figure 18: E774 fixed-target constraints for the KK model. The different coloured curves are for different numbers of extra dimensions; $n = 1$ (red), $n = 2$ (orange), $n = 3$ (brown), $n = 4$ (green), $n = 5$ (blue). The constraints are only produced for the ranges of m described in Table 1. There are negligible constraints for $n = 6$, and these are not plotted. Note that it is still possible to get constraints for $m \leq 2\,m_e$. This is because higher-mass KK modes with $m_k > 2\,m_e$ can still decay to a detectable e^+e^- pair.

constraints.

Constraints are obtained from the experiments E137, E141, and E774. The constraints for the non-KK model are shown in Figure 15.

Constraints are also produced in the KK model. There are generally contributions from KK modes with masses $> 2\,m_\mu$. These higher-mass KK modes have decays to final-state SM particles other than the electron or positron. The higher-mass final-state SM particles do not contribute significantly to the observed signal. However these particles do reduce the mean free path l_0. The final constraints are shown Figure 16 (E137), Figure 17 (E141), and Figure 18 (E774).

12 Solar-lifetime constraints

It can be shown that any form of exotic solar luminosity must be smaller than that arising from SM photons, otherwise the consumption rate of nuclear fuel is too great and no present day solar model can be constructed [33–35, 102]. A constraint is then obtained by insisting that the hidden-photon luminosity is larger than that of SM photons [35].

12.1 Reabsorption in solar-lifetime constraints

First it should be noted that solar energies are $\lesssim 0.1$ MeV. Hence decays to $e^+ + e^-$, or any higher-mass SM particles, are not significant. It is further shown in Chapter 8.2.1 that $X \to \gamma + \gamma + \gamma$ are negligible on the energy and length scales of the solar-lifetime experiment. Therefore hidden-photon reabsorption through decay is negligible. However reabsorption can still occur via hidden-photon scattering within the sun.

In Chapter 8.1 it is explained that in some cases of real production, hidden-photon reabsorption results in an upper boundary for constraints. However the solar-lifetime constraints are significantly different. It is indeed possible for a hidden photon to be reabsorbed within the sun via scattering. It would then be possible to account for this reabsorption with the usual escape probability factor e^{-l/l_0}, which would lead to the usual upper boundary. For parameter space above the upper boundary, the hidden photon is not constrained from energy-loss considerations.

However the calculation uses a precise solar model (BP05(OP) [103]) which is consistent with recent helioseismology and neutrino-flux data. If a hidden photon is reabsorbed then the non-local energy transfer would unacceptably disturb the tightly-constrained solar model [35, 104]. Hence this reabsorption region, above the upper boundary, is still ruled out by non-local energy-transfer considerations. Therefore it is not necessary to explicitly consider hidden-photon reabsorption. The final constraints therefore contain a lower boundary only, as can be seen from Figures 19 and 20.

This argument carries over to the HB-lifetime constraints. In the HB case, non-local energy transfer disturbs the tightly-constrained stellar model for the

globular-cluster star [105].[15]

12.2 Solar-lifetime constraints for the non-KK model

Solar-lifetime constraints were first considered in [36,106]. However the most recent constraints [35] properly account for resonant effects caused by SM-photon $\longleftrightarrow$ hidden-photon oscillations and are much stronger.

In a plasma the SM photon has both transverse and longitudinal excitations. However it is shown in [35] that the contribution from longitudinal modes is always smaller than that of transverse modes. Hence ignoring the the longitudinal contribution produces a small error. This error can be quantified by noting that production $\sim \chi^2$ for both transverse and longitudinal modes. Therefore ignoring the longitudinal contribution weakens the constraint by a factor $\lesssim \sqrt{2}$. Therefore in this work only transverse excitations are considered. This simplifies the calculation considerably and also produces a slightly conservative constraint.

Transverse modes behave like massive particles and are always timelike. Therefore it is possible to write down a complex mass squared term π_γ^2.[16] Overall the hidden-photon Lagrangian is now given by

$$\mathcal{L} = -\frac{1}{4}F_{\mu\nu}F^{\mu\nu} + \frac{1}{2}\pi_\gamma A_\mu A^\mu - \frac{1}{4}X_{\mu\nu}X^{\mu\nu} + \frac{1}{2}m_X^2 X_\mu X^\mu - \frac{\chi}{2}F_{\mu\nu}X^{\mu\nu}\,. \quad (12.1)$$

where small-angle approximations have been for χ.

The real part of π_T is the effective squared mass of the SM photon. To leading order this is given by [107–109]

$$\mathrm{Re}\{\pi_\gamma\} \equiv m_\gamma^2 \sim \omega_P^2 \sim \frac{4\pi\alpha\, n_e}{m_e}, \quad T \ll m_e\,,$$

where ω_P is the plasma frequency and n_e is the electron number density.

The imaginary part of π_γ is the photon energy ω multiplied by the difference between the absorption and production rates [35, 110]. Production includes a Boltzmann exponential factor, so $\Gamma_\gamma^P \sim \Gamma_\gamma\, e^{-\omega/T}$, where Γ_γ is the absorption

[15] Note that in the SN1987a experiment the stellar model actually allows non-local energy transfer. Hence this argument does not carry over, and hidden-photon reabsorption must be accounted for explicitly (see Chapter 16).

[16] Longitudinal modes have more complex behaviour and can be either timelike, spacelike, or lightlike. Hence it is not possible to write down a simple mass term for them.

rate. Therefore a damping factor D_γ is defined as the difference between the production and absorption factors,

$$\begin{aligned} \mathrm{Im}\{\pi_\gamma\} &\equiv \omega D_\gamma \,, \\ &= \omega \left(\Gamma_\gamma^P - \Gamma_\gamma\right) \,, \\ &\sim \omega \left(e^{-\frac{\omega}{T}} - 1\right) \Gamma_\gamma \,. \end{aligned} \tag{12.2}$$

In a plasma environment the squared mass of the electron also receives corrections [111]. These corrections $\sim \mu_e^2$ and $\sim T^2$, where μ_e is the electron chemical potential. In the sun electrons are non-degenerate so $\mu_e \ll m_e$, where m_e the vacuum value of the electron mass. Electrons are also non-relativistic with $T \ll m_e$. Hence these corrections to the electron mass are negligible, and the electron mass can just be taken as $\sim m_e$.

It is now necessary to calculate D_γ. The significant transitions are of the free-free type, meaning that initial-state and final-state electrons are in free and not bound states [35]. The effects of free-bound and bound-bound transitions are neglected, which effectively assumes perfect ionization throughout the sun. This approximation actually breaks down in the outer layers of the sun, where production is mainly of lower-energy hidden photons with $\omega \sim$ eV. However the energy of these particles is small. Furthermore these particles are produced in a small volume of the sun and therefore represent a very small fraction of produced hidden photons. Hence the errors are small and this approximation is valid.

One significant contribution is from Compton scattering $\gamma + e^- \to \gamma + e^-$, and the other from bremsstrahlung $e^- + Z \to e^- + Z + \gamma$. The Compton-scattering rate is given by

$$\Gamma_{\mathrm{Compton}} = \frac{8\pi\alpha^2 n_e}{3m_e^2} \,, \tag{12.3}$$

and the bremsstrahlung rate is given by

$$\Gamma_{\mathrm{bremsstrahlung}} = \frac{16\pi^2\alpha^3}{3m_e^2\omega^3}\sqrt{\frac{2\pi m_e}{3T}}\, n_e \sum_i Z_i^2\, n_i\, \overline{g_{f,f,i}} \,, \tag{12.4}$$

where the i index stands for the different species of positive ion. There are contributions from the following nuclear species; H, ^3He, ^4He, ^{12}C, ^{14}N, ^{16}O. However to a good approximation it is possible to neglect contributions from the less abundant species ^{12}C, ^{14}N, and ^{16}O.

$\overline{g_{f,f,i}}$ is the Boltzmann-averaged Gaunt factor, which accounts for quantum deviations to the classical expression. An expression for this is given in [112],

$$\overline{g_{f,f,i}} = 1 + \frac{0.1728}{\kappa^{\frac{2}{3}}} - \frac{0.0496}{\kappa^{\frac{4}{3}}} - \frac{0.0172}{\kappa^2} + O(\kappa^{-3}), \quad \kappa = Z\left(\frac{\text{Rydberg}}{\omega}\right)^{\frac{1}{2}} . \quad (12.5)$$

Most SM-photon energies are much larger than a Rydberg, so this correction is extremely small. Once again this approximation breaks down in the outer layers of the sun, and again the errors involved are small.

If an A_I oscillates into an X_P it can escape from the sun and contribute to energy loss. The oscillating fraction is calculated by employing a treatment similar to the one in Chapter 2.2, only this time accounting for the non-zero complex squared plasma-mass of the SM photon π_γ.

The Lagrangian in Equation (12.1) is transformed to the interaction-eigenstate basis by using the definitions [20]

$$A_I = A, \quad X_I = X - \chi A\,. \quad (12.6)$$

The Lagrangian now becomes

$$\begin{aligned}\mathcal{L} &= -\frac{1}{4}F_{\mu\nu}F^{\mu\nu} + \frac{1}{2}\pi_\gamma A_\mu A^\mu - \frac{1}{4}\left(X_{I\mu\nu} + \chi F_{\mu\nu}\right)\left(X_I^{\mu\nu} + \chi F^{\mu\nu}\right) \\ &\quad + \frac{\chi}{2}\left(X_{I\mu\nu} + \chi F_{\mu\nu}\right)F^{\mu\nu} + \frac{1}{2}m_X^2\left(X_{I\mu} + \chi A_\mu\right)\left(X_I^\mu + \chi A^\mu\right), \\ &= -\frac{1}{4}F^I_{\mu\nu}F_I^{\mu\nu} - \frac{1}{4}X^I_{\mu\nu}X_I^{\mu\nu} + \frac{\pi_\gamma}{2}A^I_\mu A_I^\mu + \frac{m_X^2}{2}\left(X^I_\mu X_I^\mu - 2\chi A^I_\mu X_I^\mu + \chi^2 A^I_\mu A_I^\mu\right). \quad (12.7)\end{aligned}$$

This is transformed to the propagation-eigenstate basis by diagonalizing the squared-mass matrix

$$\begin{pmatrix} m_X^2 & -\chi m_X^2 \\ -\chi m_X^2 & \chi^2 m_X^2 + \pi_\gamma \end{pmatrix} . \quad (12.8)$$

The eigenvalues are given by

$$\begin{aligned}&\lambda^2 - \lambda\left(\pi_\gamma + m_X^2 + \chi^2 m_X^2\right) + \pi_\gamma m_X^2 = 0\,, \\ &\rightarrow \lambda = \frac{1}{2}\left(m_X^2 + \pi_\gamma + \chi^2 m_X^2 \pm \left(m_X^2 - \pi_\gamma\right)\sqrt{1 + \frac{2\chi^2 m_X^2\left(m_X^2 + \pi_\gamma\right)}{\left(m_X^2 - \pi_\gamma\right)^2}}\right) + O(\chi^4) \\ &\lambda = m_X^2 + \frac{\chi^2 m_X^4}{m_X^2 - \pi_\gamma} + O(\chi^4) \text{ or } \pi_\gamma - \frac{\chi^2 m_X^4}{m_X^2 - \pi_\gamma} + O(\chi^4) \\ &\sim \pi_\gamma \text{ or } m_X^2\,. \end{aligned} \quad (12.9)$$

Therefore the propagating eigenstates (A_P, X_P) have mass squared terms $\sim (\pi_\gamma, m_X^2)$. Furthermore the bases are related by

$$\begin{pmatrix} A_I \\ X_I \end{pmatrix} = \begin{pmatrix} 1 & \frac{-\chi\, m_X^2}{m_X^2 - \pi_\gamma} \\ \frac{\chi\, m_X^2}{m_X^2 - \pi_\gamma} & 1 \end{pmatrix} \cdot \begin{pmatrix} A_P \\ X_P \end{pmatrix} . \tag{12.10}$$

If an A_I particle is produced at $t = 0$, $z = 0$, then the wavefunction at general t, z is given by

$$A_I(t,z) \simeq e^{i\left(\omega t - k_{A_P} z\right)} A_P + \frac{\chi m_X^2}{\pi_\gamma - m_X^2} e^{i\left(\omega t - i k_{X_P} z\right)} X_P \ , \tag{12.11}$$

where $k_{A_P} \sim \sqrt{\omega^2 - m_\gamma^2}$, and $k_{X_P} \sim \sqrt{\omega^2 - m_X^2}$.

A_P is strongly damped by the imaginary part of π_γ. It therefore does not propagate very far, and has a negligible chance of escape. X_P does not have this damping and it is possible for this eigenstate to escape. The probability of a produced A_I escaping a sun is therefore the probability that it turns into an X_P and not as A_P,

$$P_{A_I \to X_P} = |\langle A_I | X_P \rangle|^2 \simeq \chi^2 \frac{m_X^4}{(m_\gamma^2 - m_X^2)^2 + (\omega D_\gamma)^2} \ , \tag{12.12}$$

where m_γ and D_γ are evaluated at the point of production. This probability factor is essentially the effective coupling strength between the SM photon and the hidden photon within a plasma

$$\chi_{eff}^2 = \chi^2 \frac{m_X^4}{(m_\gamma^2 - m_X^2)^2 + (\omega D_\gamma)^2} \ . \tag{12.13}$$

If $m_X \gg m_\gamma$ vacuum conditions are reproduced and $\chi_{eff} \to \chi$ as expected. For $m_X \ll m_\gamma$, $\chi_{eff}^2 \sim \chi^2\, m_X^4$, so the hidden-photon effect dies off as a power law and constraints also decay as a power law ($\chi \sim m_X^{-2}$). This satisfies the requirement that hidden-photon constraints should die off in the limit $m_X \to 0$.[17] At the resonance $m_X = m_\gamma$ the SM-photon width D_γ becomes important as a damping factor.

The total luminosity can now be calculated. The production rate of A_I particles must be multiplied by the density of states $(4\pi r^2 dr k^2 dk)/(2\pi^2)$, a factor

[17] Note that high-mass decay of the constraint is already guaranteed by the Boltzmann-exponential factor for real production.

of the energy ω, and finally the oscillation probability factor from Equation (12.12). This is then integrated over $0 \leq r \leq R_\odot$,

$$L_X = \int_{m_X}^{\infty} d\omega\, \omega^2 \sqrt{\omega^2 - m_X^2} \int_0^{R_\odot} 4\pi r^2 dr\, \frac{1}{\pi^2}\, \chi_{eff}^2\, \Gamma_\gamma\, e^{-\frac{\omega}{T}}\,. \qquad (12.14)$$

The values of macroscopic quantities such as n_i, n_e, and T are taken from the solar model BP05(OP) [103]. The excluded region is given by $L_X > L_\gamma = 3.83 \times 10^{26}\,\text{Watt} \sim 10^{30}\ (\text{eV})^2$, and is shown as the black constraint in Figure 19.

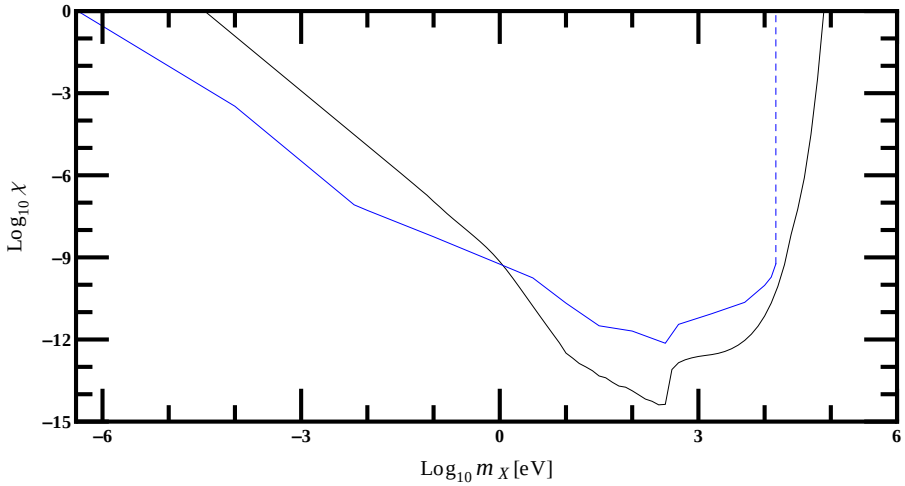

Figure 19: Non-KK constraints from solar experiments. Due to the consideration of non-local energy transfer it is not necessary to explicitly account for hidden-photon reabsorption (see Chapters 12.1 and 13.1). This results in a lower boundary and no upper boundary for constraints, as explained in Chapter 12.1. The black curve is the constraint from solar-lifetime considerations. This is obtained by insisting that the hidden-photon luminosity is larger than the SM-photon luminosity. The blue curve is the constraint from the CAST experiment (see Chapter 13.2). This is obtained by insisting that the hidden-photon contribution to the CAST signal is larger than the experimental background. CAST is only sensitive to particles with energies < 15 keV. This results in an upper limit for the range of m_X, which is shown by the blue-dashed line.

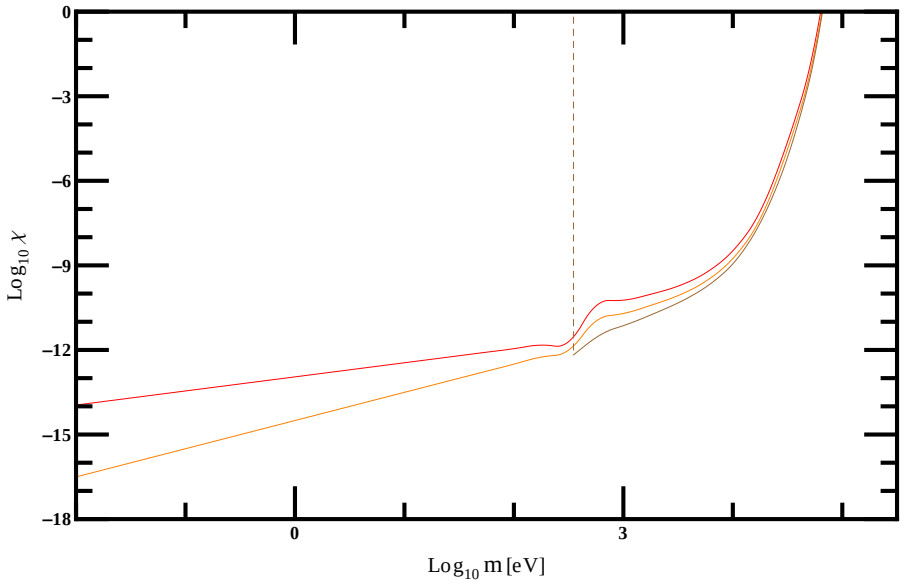

Figure 20: Solar-lifetime constraints for the KK model. This is a real-production experiment and hidden photons are produced thermally, with production exponentially suppressed for KK modes with masses $\gtrsim 0.1$ MeV. Therefore no constraints are produced for $n = 4, ..., 6$, as in this mass region KK modes are already experimentally excluded (see Table 1). Constraints for $n = 1, ..., 3$ are obtained; $n = 1$ (red), $n = 2$ (orange), and $n = 3$ (brown), where the $n = 3$ constraints only occurs for $m > 0.35$ keV. Because of the exponential suppression of high-mass KK modes, the total hidden-photon effect is manifestly UV finite for all n. Hence it is not necessary to include an UV cutoff $M_c = aM_*$, and constraints have no uncertainties from the parameter a (see Chapter 6.1).

12.3 Solar-lifetime constraints for the KK model

The constraints are obtained by summing over KK modes in the usual manner, and are plotted in Figure 20. Production is exponentially suppressed for KK modes with masses $\gtrsim 0.1$ MeV. The first repercussion of this is that no constraints are produced for $n = 4, ..., 6$, as in this mass region KK modes are already experimentally excluded (see Table 1). Constraints for $n = 1, ..., 3$ are obtained; $n = 1$ (red), $n = 2$ (orange), and $n = 3$ (brown), where the $n = 3$ constraint only occurs for $m > 0.35$ keV. The second repercussion it that the total hidden-photon effect is manifestly UV finite for all n (see Chapter 6.1). Therefore it is not necessary to include an UV cutoff $M_c = aM_*$, and constraints have no uncertainties from the parameter a.

12.4 Summary of Chapter 12

Solar hidden photons can escape from the sun and contribute to solar energy loss. If this is larger than the SM-photon luminosity $L_\odot$ then no present day solar model can be constructed [33–35, 102], effectively constraining the hidden photon.

Hidden photons are not significantly reabsorbed through decay. This is because solar energy scales ($\lesssim 0.1$ MeV) are too low for $X \to f^+ + f^-$ decay, and the decay $X \to \gamma + \gamma + \gamma$ is negligible on solar energy and length scales. Reabsorption can still occur through scattering. However scattering results in non-local energy transfer, which unacceptably disturbs the tightly-constrained solar model. Therefore reabsorbed hidden photons are still excluded. Hence it is not necessary to explicitly consider hidden-photon reabsorption, and constraints do not have an upper boundary.

The first stage of the calculation is to calculate the production rate of SM-photon interaction eigenstates A_I. An A_I particle must oscillate into a hidden-photon propagation eigenstate X_P in order to escape. The probability associated with this oscillation process results in the effective plasma-modified kinetic mixing χ_{eff} (Equation (12.13)). If $m_X \gg m_\gamma$ vacuum conditions are reproduced and $\chi_{eff} \to \chi$ as expected. For $m_X \ll m_\gamma$, $\chi^2_{eff} \sim \chi^2 m_X^4$, so the hidden-photon effect dies off as a power law, satisfying the requirement that constraints die off as $m_X \to 0$.

The constraint for the non-KK model is shown as the black curve in Figure 19.

Constraints for the KK model are produced by summing over KK modes in the usual fashion. These are shown in Figure 20. This is a real-production experiment, with hidden photons being produced thermally. Therefore the production of very high-mass KK modes is exponentially suppressed and the total hidden-photon effect is manifestly UV finite. Hence there is no need to introduce a cutoff parameter $M_c = aM_*$, and the constraints have no uncertainties from the parameter a. Furthermore no constraints are produced for $n = 4, ..., 6$, as in the solar energy range ($\lesssim 0.1$ MeV) KK modes are already experimentally excluded (see Table 1).

13 CERN Axion Solar Telescope (CAST) constraints

The experimental data is taken from the CERN Axion Solar Telescope (CAST) [113], which is capable of detecting hidden photons [35, 114–116]. A constraint is obtained by insisting that the flux detected by the helioscope is larger than the experimental background [35].

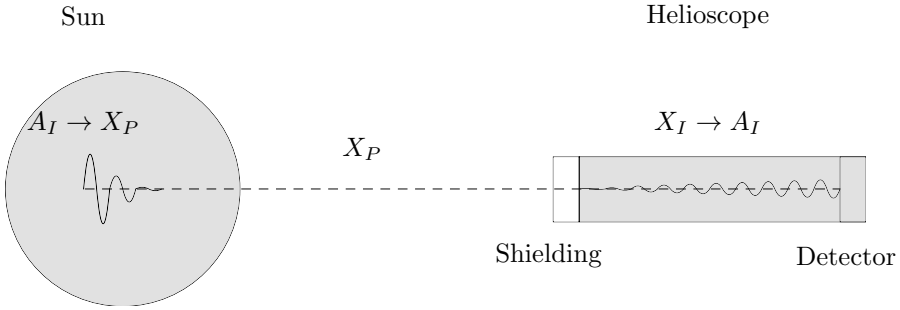

Figure 21: Schematic diagram showing how hidden photons can be detected in CAST. A SM-photon interaction eigenstate A_I is produced inside the sun. This can then oscillate into a hidden-photon propagation eigenstate X_P, which can then exit the sun. On passing through the detector shielding, the X_P is projected onto the hidden-photon interaction eigenstate X_I, which then passes through the detector. This can then oscillate into a detectable SM-photon interaction eigenstate A_I. This figure is modified slightly from the one in [35].

The schematic experimental set-up is shown in Figure 21. The hidden-photon propagation eigenstates X_P exit the sun and are projected onto the interaction eigenstates X_I when the beam passes through the shielding. $X_I - A_I$ oscillations take place within the vacuum region of the helioscope. If a A_I particle is present when the beam hits the detector then a signal is recorded.

13.1 Reabsorption in CAST constraints

Chapter 12.1 showed that it is not necessary to explicitly consider hidden-photon reabsorption in solar-lifetime experiments. This is because a reabsorbed hidden photon would cause forbidden non-local energy transfer and would therefore

still be constrained.

The CAST experiment is slightly more tricky. It is still not necessary to account for reabsorption within the sun, as this is accounted for in the solar-lifetime constraint. However a hidden photon can now be reabsorbed outside the sun on its way to the CAST detector. This hidden photon would then not contribute to constraints.

It is easy to show that decays are not important. The CAST detector can only detect hidden photons with energies $\lesssim 15$ keV, so decays to $e^+ + e^-$, or any higher-mass SM particles, are not significant. A lower bound for the mean free path for the decay $X \to \gamma + \gamma + \gamma$ is given by Equation (8.3) with $E_{max} \sim 15$ keV, which leads to $l_0 \gtrsim (2 \times 10^{17})/\chi^2 \gtrsim 2 \times 10^{17}$ metres for all $\chi \lesssim 1$. This is much larger than the earth-sun distance $R_\oplus \sim 1.5 \times 10^{11}$ metres, so this decay is negligible. Therefore decays are negligible for the CAST experiment in both the KK and the non-KK model.

The hidden photon can only be reabsorbed through scattering. This is most likely in the atmosphere of the earth, which is the most dense medium outside of the sun through which the hidden photon propagates. However the atmosphere of the earth is still much less dense than the sun, and is also many orders of magnitude smaller. Therefore a given hidden photon is much more likely to scatter inside the sun than inside the atmosphere of the earth. Hence if χ is large enough for a hidden photon to scatter in the earth's atmosphere, then it will almost certainly have already been reabsorbed within the sun. Conversely if χ is small enough for a hidden photon to escape from the sun then it will almost certainly not scatter within the earth's atmosphere. Therefore scattering outside of the sun can be ignored.

Finally it should be noted that the hidden-photon signal is depleted as it passes through the CAST shield. This is because the propagation eigenstate X_P, which travels through space, is projected onto the interaction eigenstate X_I, which enters the detector. This can be seen from Figure 21. Similar depletion occurs as the beam passes through other non-vacuum regions in the atmosphere of the earth. However this depletion is a negligible $O(\chi^2)$.

In conclusion hidden-photon reabsorption does not have to be accounted for explicitly in the CAST experiment. Therefore, like the solar-lifetime constraints,

CAST constraints have a lower boundary but no upper boundary (see Figures 19 and 22).

13.2 CAST constraints for the non-KK model

The derivation of these constraints is similar to that of the solar-lifetime ones. The total rate for hidden-photon production is found by taking the total luminosity in Equation (12.14) and removing a factor ω from the integrand. Dividing by the effective surface area $1/(4\pi R_{\oplus}^2)$ gives the average flux incident at the surface of the earth.

However only a fraction of this flux is detected by the helioscope. The X_I travels through the helioscope as a linear combination of the two propagation eigenstates. The interior of the helioscope is an approximate vacuum, so the oscillation probability is given by Equation (2.7) with a detector length of $z = 10$ metres. Multiplying the total solar flux of hidden photons by this probability gives the detected flux.

The CAST detector is only sensitive to hidden photons in the energy range $(0.5-15)$ keV [113]. The limits of the integral in Equation (12.14) need to be adjusted accordingly. A constraint is obtained by imposing that the hidden-photon effect is larger than a pessimistic background of 10^{-8}counts $\mathrm{cm}^{-2}\,\mathrm{s}^{-1}$ $(\omega/\mathrm{eV}) \sim 2.5\times10^{-33}\,(\mathrm{eV})^3$ (ω/eV) [35,113]. This is shown as the blue curve shown in Figure 19. The constraints only apply for masses up to the detector upper energy limit of 15 keV, which is shown in the figure as the blue-dashed line.

13.3 CAST constraints for the KK model

Constraints in the KK model are obtained by summing over KK modes in the usual manner. The detector imposes an experimentally-imposed upper limit for the mass of KK modes $m_k = 15$ keV, so the total hidden-photon effect is finite for all n. Hence there is no need to introduce an UV cutoff $M_c = aM_*$, and constraints have no uncertainties from the parameter a. Furthermore the constraints have an upper value of $m = 15$ keV. Finally no constraints are produced for $n = 4, ..., 6$, as in this mass region KK modes are already experimentally excluded (see Table 1).

The constraints are shown in Figure 22. The plotted curves are for $n = 1$ (red), $n = 2$ (orange), and $n = 3$ (brown) extra dimensions.

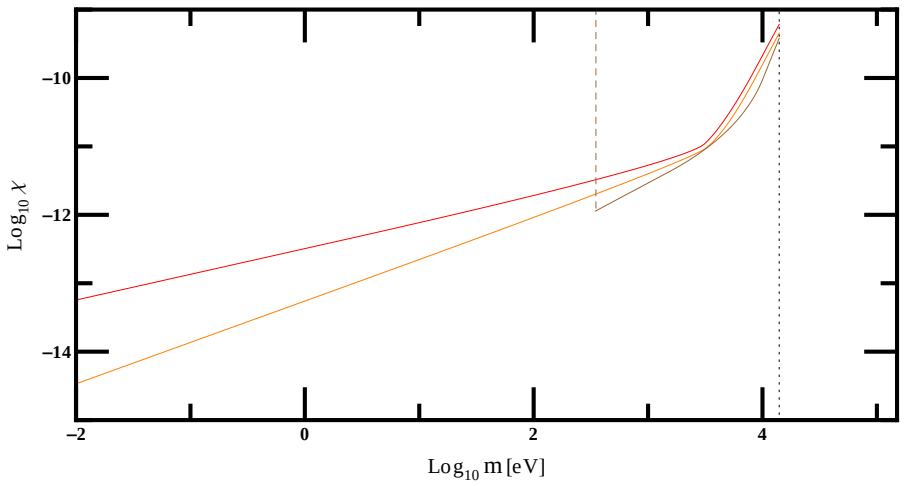

Figure 22: KK constraints from the CAST experiment. The CAST detector has an upper energy limit of 15 keV. Hence constraints have an upper limit of $m = 15$ keV, which is shown as the dashed-black curve. A further repercussion is that no constraints are produced for $n = 4, ..., 6$, as in this mass region KK modes are already experimentally excluded (see Table 1). The plotted curves are for $n = 1$ (red), $n = 2$ (orange), and $n = 3$ (brown) extra dimensions.

13.4 Summary of Chapter 13

Solar hidden photons can be detected on earth by CAST.

In the CAST experiment it is not necessary to explicitly consider hidden-photon reabsorption. Therefore constraints have a lower boundary but not an upper boundary. This is similar to the solar-lifetime experiment.

In the non-KK model a constraint is obtained by insisting that the hidden-photon effect is larger than the CAST background. The CAST detector has an upper energy limit of 15 keV, so constraints only hold up to $m_X = 15$ keV.

In the KK model constraints are obtained by summing over KK modes in the usual way (see Figure 22). The detector imposes an experimentally-imposed upper limit for the mass of KK modes $m_k = 15$ keV, so there are no uncertainties

from the parameter a, constraints have an upper value of $m = 15$ keV, and no constraints are produced for $n = 4, ..., 6$ (see Table 1).

14 Horizontal branch (HB) lifetime constraints

The basic principle here is the same as for solar-lifetime constraints. If any form of exotic solar luminosity is larger than that arising from SM photons ($\sim 20L_\odot$ where $L_\odot$ is the SM-photon solar luminosity) then the helium-burning time of a HB globular-cluster star is reduced, in conflict with observations [109]. This can be used to constrain hidden photons [117].

14.1 HB-lifetime constraints for the non-KK model

The method is similar to the one used for the solar-lifetime constraints in Chapter 12.2.

The total hidden-photon luminosity is still given by Equation (12.14). However this time the stellar model is that of a typical HB globular-cluster star [105]. There is a crucial physical difference between the sun and globular-cluster stars. In the latter case there are two major regions of energy production. The core contains mainly helium, and the major energy source there is helium burning. There is also an outer shell which contains mostly hydrogen, where the main energy source is hydrogen burning. The situation is shown in Figure 23. This leads to two different areas of resonant production for hidden photons; one in the helium-rich core, and one in the hydrogen-rich shell.

The argument from non-local energy transfer, previously used for solar-lifetime constraints (see Chapter 12.1), can be carried over. Hence it is not necessary to explicitly consider hidden-photon reabsorption, and constraints do not have an upper bound.

A constraint can be obtained by imposing that the hidden-photon luminosity is larger than the SM-photon luminosity $\sim 20L_\odot$. This is shown in Figure 24. This constraint applies at slightly higher masses than the solar-lifetime, which is due to the higher temperature scales in the HB star. The constraint is also somewhat stronger, in that it bounds χ to smaller values. This is because the densities in the HB star are around two of orders magnitude larger, meaning that hidden-photon production is more efficient.

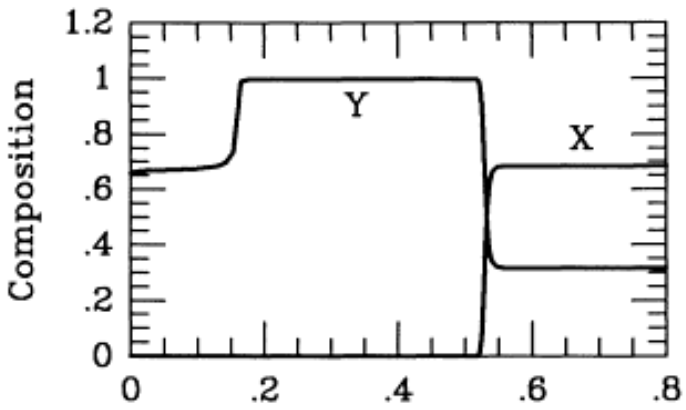

Figure 23: The chemical composition of a typical horizontal-branch (HB) globular-cluster star, as a function of the stellar mass (in units of $M_\odot$). Both the model and figure are taken from [105]. The core is mainly composed of helium (denoted Y), and there is a hydrogen (denoted X) rich shell outside the core.

14.2 HB-lifetime constraints for the KK model

In the KK model constraints are obtained by summing over KK modes in the usual manner, and these are plotted in Figure 25.

This is a real-production experiment, with hidden photons produced thermally. Therefore production of very high-mass modes is exponentially suppressed and the total hidden-photon effect is always UV finite. Hence there is no need to introduce an UV cutoff $M_c = aM_*$, and constraints have no uncertainties from the parameter a (see Chapter 6.1). Furthermore no constraints are produced for $n = 5$ or $n = 6$ because in the mass region $\lesssim 1$ MeV, KK modes are already experimentally excluded (see Table 1). Constraints for $n = 1, ..., 4$ are obtained; $n = 1$ (red), $n = 2$ (orange), and $n = 3$ (brown), and $n = 4$ (green).

14.3 Summary of Chapter 14

Hidden photons produced in HB globular-cluster stars can escape and contribute to stellar energy loss. If the hidden-photon luminosity is larger than that arising from SM photons ($\sim 20L_\odot$) then the helium-burning time is greatly reduced,

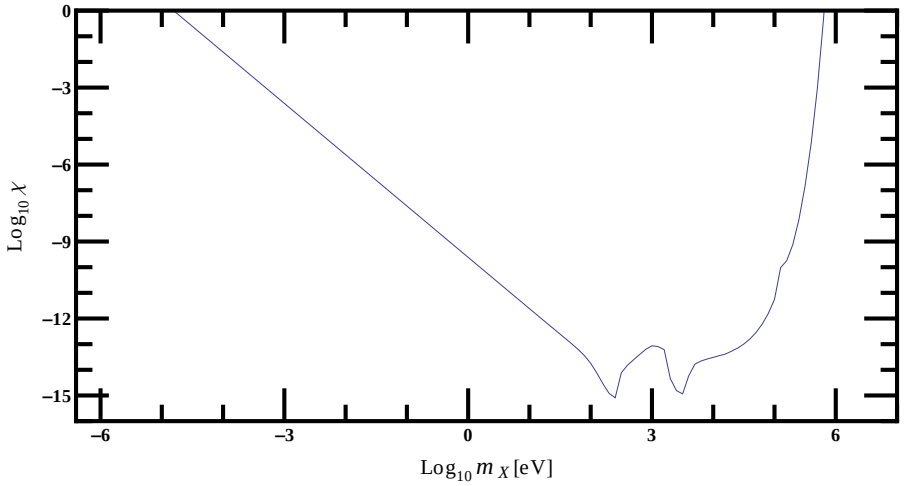

Figure 24: Non-KK constraint from consideration of the lifetime of horizontal branch (HB) stars. It is obtained by imposing that the hidden-photon luminosity is larger than the SM-photon luminosity $\sim 20L_\odot$, where $L_\odot$ is the solar SM-photon luminosity. This would significantly reduce the HB-star lifetime, in conflict with observation [109, 117]. It is not necessary to account for hidden-photon reabsorption and therefore constraints have no upper bound, as explained in Chapter 12.1. This constraint occurs at slightly higher masses than the solar-lifetime one (see Figure 19), which is due to the higher temperature scales in the HB star. There are two spikes for resonant production. This is because there are two regions of resonant production; one in the helium-rich core of the HB star, and one in the hydrogen-rich outer shell.

in conflict with observations [109]. This constrains hidden photons [117].

The argument from non-local energy transfer, used for solar-lifetime constraints, can be carried over. Hence it is not necessary to explicitly consider hidden-photon reabsorption, and constraints do not have an upper bound.

In the HB star there are two major areas of energy production; a helium-burning core, and a hydrogen-burning shell. Therefore there are two resonances for hidden-photon production. The non-KK constraint therefore has two resonance spikes (see Figure 24).

The KK constraints are obtained in the usual manner by summing over

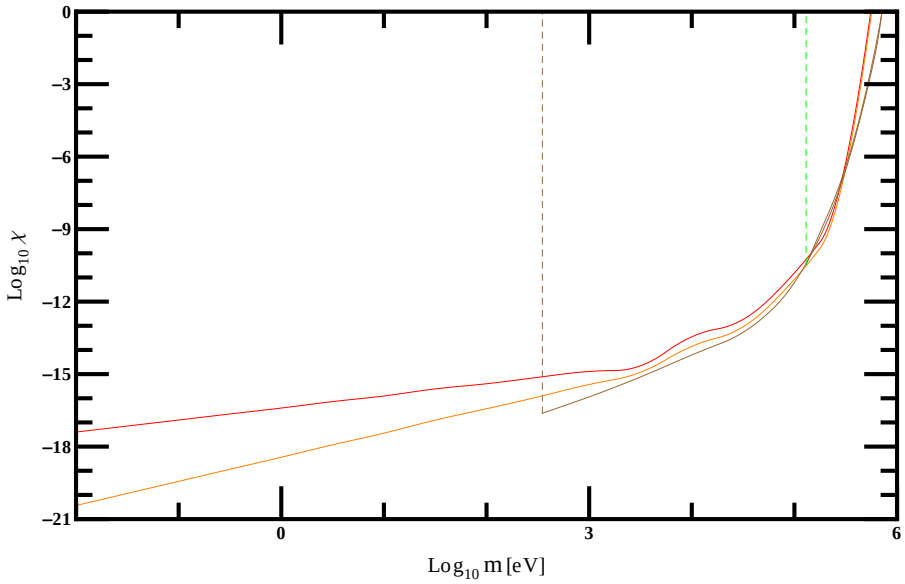

Figure 25: HB-lifetime constraints for the KK model. This is a real-production experiment and hidden photons are produced thermally, with production exponentially suppressed for KK modes with masses $\gtrsim 1$ MeV. Therefore no constraints are produced for $n = 5$ or $n = 6$, as in this mass region KK modes are already experimentally excluded (see Table 1), where production is negligible. Constraints for $n = 1, ..., 4$ are obtained; $n = 1$ (red), $n = 2$ (orange), and $n = 3$ (brown), and $n = 4$ (green). Because of the exponential suppression of high-mass KK modes, the total hidden-photon effect is manifestly UV finite for all n. Hence it is not necessary to include an UV cutoff $M_c = aM_*$, and constraints have no uncertainties from the parameter a (see Chapter 6.1).

KK modes (see Figure 25). This is a real-production experiment, with hidden photons produced thermally. Therefore production of very high-mass modes is exponentially suppressed and the total hidden-photon effect is always UV finite. Hence there is no need to introduce an UV cutoff $M_c = aM_*$, and constraints have no uncertainties from the parameter a. Furthermore no constraints are produced for $n = 5$ or $n = 6$, as KK modes are already excluded in the mass region $\lesssim 1$ MeV (see Table 1).

15 IDPB constraints

Hidden photons can be produced in the early universe. If χ is small enough then these hidden photons may have survived until the present day. The decay $X \to \gamma+\gamma+\gamma$ then contributes to the flux from the Intergalactic Diffuse Photon Background (IDPB). A constraint can be obtained by insisting that the hidden-photon contribution to the IDPB flux is larger than the experimentally-observed value [3].

15.1 IDPB constraints for the non-KK model

First it is necessary to calculate the abundance of hidden photons in the early universe. At very early times the temperature is very high. If $T \gg m_X$ then $m_\gamma \gg m_X$, the effective mixing parameter (see Equation (12.13)) is suppressed, and the hidden-photon abundance is negligible. Therefore an initial condition of zero hidden-photon abundance can be assumed.

Calculations are performed in the propagation-eigenstate basis. Here the X_P has a mass of m_X. In the early universe the leading-order contribution to the complex squared mass of the SM photon comes from Compton scattering off electrons and positrons [107, 118]. The real part is given by

$$\begin{aligned} m_\gamma^2 &= \frac{4\pi\alpha n_e}{m_e}, \quad T \lesssim 2\, m_e, \\ m_\gamma^2 &= \frac{2}{3}\alpha\pi T^2, \quad T \gtrsim 2\, m_e, \end{aligned} \tag{15.1}$$

and D_γ as defined in Equation (12.2) is given by

$$\begin{aligned} D_\gamma &= \frac{2\alpha m_\gamma^2}{3m_e}, && T \lesssim 2\, m_e, \\ D_\gamma &= \frac{3\alpha m_\gamma^2}{2\pi^2\omega}\ln\left(\frac{4T\omega}{m_e^2}\right), && T \gtrsim 2\, m_e\,. \end{aligned} \tag{15.2}$$

Propagation of the A_P is strongly damped. The X_P has no such damping factor and propagates much more efficiently. Hence the two eigenstates propagate largely separately and the Boltzmann evolution equation for incoherent production applies,

$$\frac{\partial Y_X}{\partial \ln T} = \frac{\Gamma_X}{H} \times \frac{d\ln s}{d\ln T^3} \times Y_A\,, \tag{15.3}$$

where $Y_i = n_i/s$ is the ratio of the number density to the total entropy density and H is the Hubble constant.

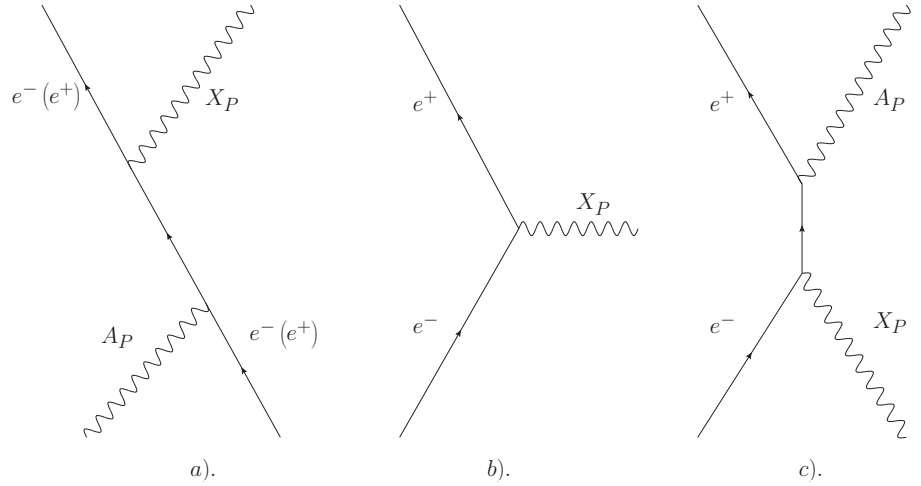

Figure 26: Feynman diagrams for hidden production in the early universe. Figure a). depicts Compton-like production of hidden photons. This can involve either an electron or positron. Figure b) depicts hidden-photon production through pair coalescence. Figure c). depicts production of a hidden photon as well as a SM photon through pair annihilation.

The effective degrees of freedom in a plasma are defined by

$$\begin{aligned} g_{eff} &= \frac{30\rho}{\pi^2 T^4}, \\ h_{eff} &= \frac{45 s}{2\pi^2 T^3}, \\ \frac{d\ln s}{d\ln T^3} &= 1 + \frac{1}{3}\frac{T}{h_{eff}}\frac{dh_{eff}}{dT}\,. \end{aligned} \tag{15.4}$$

These quantities are roughly constant in the region $T \lesssim 2\,m_e$, where the only effective degrees of freedom are neutrinos. Here $g_{eff}\,(T \lesssim 2\,m_e) \sim 3.36$, $h_{eff}\,(T \lesssim 2\,m_e) \sim 43/11$. However in the region $T \gtrsim 2\,m_e$ there is a large increase in g_{eff} and h_{eff} as higher-mass particles become energetically accessible.

Figure 26 shows the three leading-order contributions to hidden-photon production. Diagram a). is the Compton-like production process $A_P + e^- \to X_P + e^-$ or $A_P + e^+ \to X_P + e^+$. Diagram b) shows the pair-coalescence process $e^+ + e^- \to X_P$. Diagram c). shows the pair-annihilation process

$e^+ + e^- \to A_P + X_P$. The production rate is given by

$$\Gamma_X = \Gamma_{\text{Compton}} + \Gamma_{\text{coalesce}} + \Gamma_{\text{annihilate}}$$

$$= (n_{e^+} n_{e^-}) \langle \sigma_{\text{Compton}} v_{M\ddot{o}l} \rangle + \left(\frac{n_{e^+} n_{e^-}}{n_\gamma} \right) \left(\langle \sigma_{\text{coalesce}} v_{M\ddot{o}l} \rangle + \langle \sigma_{\text{annihilate}} v_{M\ddot{o}l} \rangle \right) , \quad (15.5)$$

where the Möller speed is defined as the relative speed between the two initial-state particles in a reaction. For example for initial state particles P and Q, $v_{M\ddot{o}l} = \sqrt{|v_P - v_Q|^2 - |v_P v_Q|^2}$.

It can be assumed that electrons (positrons) are in thermal equilibrium and therefore the electron (positron) number density is given by Fermi-Dirac statistics.[18]

It should be noted that the number density of the final-state particles in the production processes shown in Figure 26 is *not* equal to the equilibrium number density. Instead the produced particles should have an approximately thermal spectrum. Furthermore particles are only produced efficiently for temperatures much larger than the particle mass. Hence the particle mass can be set to zero for the purpose of calculating the number density. Hence the number density n_X of produced hidden photons is approximately that of a massless photon gas, which is denoted as n_γ. This is the origin of the n_γ factor in the denominator in the second and third terms of Equation (15.5).

The region $m_X > 2\,m_e$ is considered first. As discussed in Chapter 16.1 the effective electron mass is always larger than m_γ in a plasma [119–121], so in this region it is also true that $m_X > m_\gamma$. Hence in this region there is no resonance and the effective mixing parameter relaxes to the vacuum value, that is $\chi_{eff} \sim \chi$.

In this region the pair-coalescence process dominates, as it has one less power of α than the other two processes. In fact it is shown in [3] that the pair-annihilation and Compton-like processes can be ignored to an accuracy of more than 10 %, which is more than adequate for hidden-photon constraints.

The general expression [122, 123] for the process $P + Q \to R + S$ is given by

$$n_P\, n_Q\, \langle \sigma v_{M\ddot{o}l} \rangle \equiv \int dn_P\, dn_Q\, \sigma\, v_{M\ddot{o}l} \equiv \int \frac{g_P\, dp_P^3}{(2\pi)^3} f_P \int \frac{g_Q\, dp_Q^3}{(2\pi)^3} f_Q\, \sigma\, v_{M\ddot{o}l} \,, \quad (15.6)$$

[18] This contrasts with the solar-lifetime experiment, where electrons are not in thermal equilibrium and the number densities used in the calculation are given by the solar model.

where g is the number of physical degrees of freedom and f is the Fermi/Bose-distribution function. Due to the high temperatures involved, Boltzmann statistics can be used to a good approximation for all particles. With this assumption the expression simplifies to [123]

$$\frac{n_P\, n_Q}{n_\gamma}\,\langle \sigma v_{M\ddot{o}l}\rangle \sim \frac{g_P g_Q}{g_\gamma}\frac{1}{32\pi^2\zeta(3)T^2}\int_{s_0}^{\infty}(s-s_0)\,ds\sqrt{s}\;\sigma\,(s)\,K_1\left(\frac{\sqrt{s}}{T}\right)\,, \quad (15.7)$$

where $s_0 = (m_P + m_Q)^2$, and K_1 is the modified Bessel function of the second kind.

The leading-order cross section for the coalescence process is given by

$$\sigma_{\text{coalescence}} = 4\pi\alpha^2\chi^2\sqrt{s-4m_e^2}\left(1+\frac{2\,m_e^2}{m_X^2}\right)\delta\left(s-m_X^2\right), \quad (15.8)$$

which leads to

$$\frac{n_e^2}{n_\gamma}\,\langle \sigma_{\text{coalescence}} v_{M\ddot{o}l}\rangle \sim \frac{\chi^2\alpha}{4\zeta\,(3)\,T^2}K_1\left(\frac{m_X}{T}\right)\left(m_X^2+2\,m_e^2\right)\sqrt{m_X^2-4m_e^2}\,. \quad (15.9)$$

This is substituted into Equation (15.3).

A flat universe can also be assumed to a good approximation, which results in the following form of the Friedmann equation

$$H^2 = \frac{8\pi G\rho}{3}\,. \quad (15.10)$$

This is also substituted into Equation (15.3).

It can be numerically confirmed that the integral over T is dominated by the contribution at $T \sim m_X/3$, so

$$Y_X \sim \left(10^{17}\right)\chi^2\left(\frac{\text{GeV}}{m_X}\right)\left[\frac{1}{\sqrt{g_{eff}}\,h_{eff}}\frac{d\ln s}{d\ln T^3}\sqrt{1-\frac{4m_e^2}{m_X^2}}\;\right]_{T\sim\frac{m_X}{3}}. \quad (15.11)$$

It is important to note that in the region $T \sim m_X/3 > 2\,m_e$ there is an increase in the effective degrees of freedom g_{eff} and h_{eff}. These are accounted for by using the expressions given in [124].

Furthermore in this region there are generally temperature-related plasma mass corrections to the vacuum mass of the electron.[19] The effective electron mass can be written as $m_{e,eff}^2 - m_e^2 \sim \pi\alpha T^2$, where m_e is the electron vacuum

[19] Note that electrons are generally non-degenerate, so there are no significant corrections from μ_e.

mass. However production is dominated at $T \sim m_X/3$, so this correction is $\sim \alpha\, m_X^2$. Hence the phase space factor in Equation (15.11) gets a negligible correction $O(\alpha)$, and it is possible just to use m_e in Equation (15.11).

For $m_X > 2\, m_\mu$ there are extra production channels with other colliding fermion-antifermion pairs. Therefore the total hidden-photon abundance is approximately given by Equation (15.11) multiplied by a factor N_{eff} (Equation (11.14)).

The region $m_X \leq 2\, m_e$ is now considered. In this region it is possible for $m_X = m_\gamma$, and therefore for resonance to occur.

In calculating the hidden-photon abundance it will be simpler to reverse the order of integrations over particle number and temperature. This means performing the temperature integral first, and then taking the average of $\langle \sigma v_{M\ddot{o}l} \rangle$ second. Introducing the notation $\sigma = \chi_{eff}^2\, \widetilde{\sigma}$,

$$Y_X = \int_0^\infty \frac{\widetilde{\sigma}}{HTs} \frac{d\ln s}{d\ln T^3} \frac{\chi^2 m_X^4}{\left(m_X^2 - m_\gamma^2\right)^2 + (\omega D_\gamma)^2} dT\,. \tag{15.12}$$

Production is dominated by the resonance so the SM-photon mass can be expanded as follows,

$$m_\gamma^2 = m_X^2 + z\,(T - T_r)\ , \tag{15.13}$$

where

$$z = \left.\frac{dm_\gamma^2}{dT}\right|_{T\,=\,T_r}\ . \tag{15.14}$$

Hence

$$Y_X \sim \left[\frac{\chi^2 m_X^2}{HTs} \frac{d\ln s}{d\ln T^3}\, \widetilde{\sigma}\right]\Bigg|_{T\,=\,T_r} \int_0^\infty \frac{dT}{z^2\,(T - T_r)^2 + (\omega D_\gamma)^2}\,. \tag{15.15}$$

The temperature integral is given by

$$\int_0^\infty \frac{dT}{z^2\,(T - T_r)^2 + (\omega D_\gamma)^2} \sim \frac{\pi}{\omega D_\gamma z}\ . \tag{15.16}$$

The next step uses the expression [122, 123] for the per-unit-volume scattering rate for a particle P and a particle Q colliding,

$$\frac{dN}{dV dt} = \sigma\, v_{M\ddot{o}l}\, n_P\, n_Q\,, \tag{15.17}$$

The two energetically allowed processes both have one final-state hidden photon plus one SM particle. The final-state SM particle is produced with an approximately thermal spectrum, and production is only efficient for masses $\ll T$.

Hence the SM particle is produced with approximately the spectrum of a massless SM photon. Hence in Equation (15.17) it is possible to set $1/dt = \Gamma_\gamma$. Furthermore dN/dV can be taken as the produced number density of produced hidden photons. Therefore

$$\int dn_P\, dn_Q\, \frac{\widetilde{\sigma}\, v_{M\ddot{o}l}}{\omega D_\gamma} = \int dn_X \frac{\Gamma_\gamma}{\omega D_\gamma} = \frac{\zeta(2)\, n_\gamma}{\zeta(3)\, T}\,, \tag{15.18}$$

where $\Gamma_\gamma \left(1 - e^{-\omega/T}\right) = D_\gamma$, $m_\gamma, m_X \ll T$ have been used. The details of the cross section have dropped out. The important physical effect is therefore the resonance. Overall

$$Y_X \sim \left[\chi^2 \pi \times \frac{\zeta(2)}{\zeta(3)} \times \frac{m_\gamma^2\, m_X^2\, Y_A}{Hz\, T^2} \times \frac{d\ln s}{d\ln T^3}\right]\Bigg|_{T\,=\,T_r}\,. \tag{15.19}$$

Finally using the SM-photon mass $m_\gamma^2 = (2/3)\alpha\pi T^2$ and the resonance condition,

$$Y_X \sim 1.3 \times 10^{17} \chi^2 \left(\frac{\mathrm{GeV}}{m_X}\right) \frac{1}{\sqrt{g_{eff}}\; h_{eff}} \frac{d\ln s}{d\ln T^3}\,. \tag{15.20}$$

It should be briefly noted that there are again plasma deviations to the electron mass in the region $m_X \leq 2\, m_e$. However this is not important as the details of the cross section have dropped out of the final abundance in Equation (15.20), and therefore so have the specific details of the electron mass.

The current density of hidden photons can be found by using the conservation of entropy per comoving volume,

$$\Omega_2 h^2 = 2.82 \times 10^8 \left(\frac{m_X}{\mathrm{GeV}}\right) Y_X\,. \tag{15.21}$$

Hidden-photon constraints can now be produced. The region $m_X \leq 2\, m_\mu$ is considered first. The upper boundary in Figure 27 is obtained by insisting that the lifetime of the X_P is $\gtrsim$ the age of the universe $t_0 \sim 4.3 \times 10^{17}$ seconds $\sim 6.4 \times 10^{32}\,(\mathrm{eV})^{-1}$. For most of this time the universe was, to a very good approximation, a vacuum. Therefore it is possible to set $m_\gamma \sim 0$. Hence the decay rates for the hidden photon are given by Equations (8.1) and (8.4). The upper boundary is shown as the dashed-red curve in Figure 27.

The lower boundary is obtained by demanding that the flux of SM photons given off by hidden-photon decay is less than the total gamma-ray flux. This observed flux is approximately proportional $\omega^{1.3}$, where ω is the SM-photon

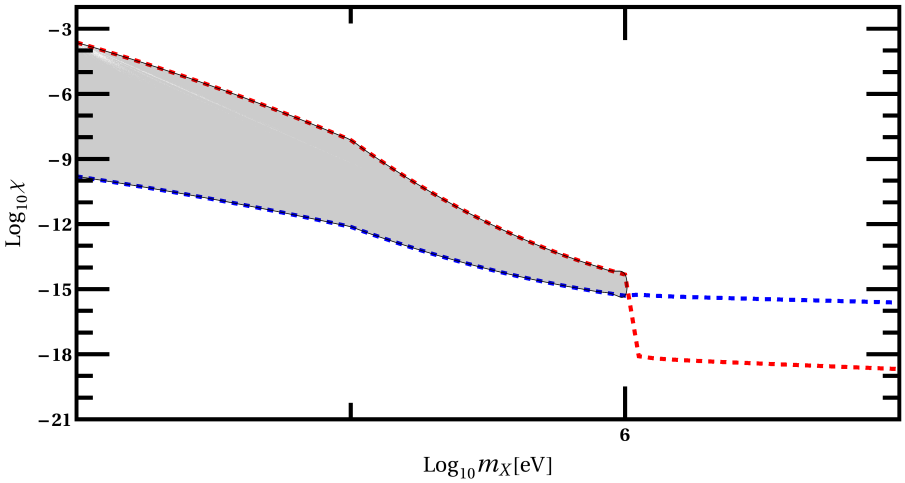

Figure 27: Constraints from the Intergalactic-Diffuse-Photon-Background (IDPB) experiment for the non-KK model. The dashed-red curve is an upper boundary. It is obtained by insisting that the hidden photon can survive until the present day. There is a spike at $m_X \sim 2\,m_e$ due to the $X \to e^+ + e^-$ decay channel becoming energetically available. The dashed-blue curve is a lower boundary. It is obtained by insisting that the hidden-photon contribution to the IDPB is large enough to be observable. In the region $m_X > 2\,m_e$ the red upper boundary descends below the blue lower boundary, so this region is not constrained. The constrained region is shaded.

frequency. Data exists roughly in the region $10\,\text{keV} \lesssim \omega \lesssim 100$ GeV, and leads to the relationship [3, 125]

$$\Gamma_{X\to\gamma+\gamma+\gamma} \times m_X^{-1} \times \left(1.5\times 10^{51}\right)\left(\frac{\omega}{\text{GeV}}\right)^{1.3}\left(\Omega_X h^2\right) \gtrsim 1\,, \qquad (15.22)$$

where for the hidden-photon loop decay $\omega \sim m_X/3$.

Note that for $m_X > 2\,m_\mu$ there are extra channels which contribute to the loop decay, which include other SM fermions in the loop. Therefore the total decay rate for the loop process is approximately given by Equation (8.1) multiplied by a factor N_{eff} (Equation (11.14)).

The hidden-photon relic density (Ωh^2) is given by Equations (15.11), (15.20), and (15.21). The lower boundary is shown as the blue curve in Figure 27.

In the region $2\,m_e < m_X \leq 2\,m_\mu$ the stronger decay channel $X \to e^+ + e^-$

becomes available, causing the hidden-photon lifetime to decrease sharply. This causes the upper boundary to descend sharply, actually making it go below the lower boundary. Hence this region is not constrained.

In the region $m_X > 2\,m_\mu$ the same result is obtained. The extra tree-level decays of the form $m_X \to f^+ + f^-$ still dominate over the loop-level decay $X \to \gamma + \gamma + \gamma$, the upper boundary remains below the lower boundary, and no constraints are obtained. Hence there are no constraints for the whole region $m_X > 2\,m_e$.

15.2 IDPB constraints for the KK model

For the IDPB experiment the KK-model constraints are slightly unusual. Normally the total hidden-photon effect is obtained by summing over KK modes. However KK modes of different masses m_k actually contribute to the IDPB at different frequencies $\omega \sim m_k/3$.

The physical discussion is simpler if different numbers of extra dimensions n are considered separately. The first considered case is $n = 1$. For each value of m there is a whole range of KK mode masses $30\,\text{keV} \lesssim m \leq m_k \lesssim 100$ GeV, where the lower and upper mass limits are set by the IDPB data [3]. Each different value of m_k actually constrains a different range of χ. Note that in the $n = 1$ case the constraint for a KK mode with mass m_k is simply the non-KK constraint with $m_X \to m_k$. Hence the constraint for each KK mode is simply given by Figure 27, except with $m_X \to m_k$. It is again found that no constraints are obtained for $m_k > 2\,m_e$, as the upper bound descends below the lower bound.

Therefore the highest excluded value of χ (for a particular value of m) is given by the highest excluded value which is excluded by any KK mode with $m \leq m_k \leq 2\,m_e$. This always comes from the lowest mass KK mode ($m = m_k$) because this has the largest lifetime. Furthermore the lowest excluded value of χ (for a particular value of m) is given by the lowest excluded value which is excluded by any KK mode with $m \leq m_k \leq 2\,m_e$. This always comes from the highest KK mode which actually produces constraints ($m_k = 2\,m_e$) because this makes the largest contribution to the IDPB. Therefore for any m the constrained region is given by $\chi_{min}(m_k = 2\,m_e) \leq \chi \leq \chi_{max}(m_k = m)$. The total KK

constraint for $n = 1$ (as a function of m) is therefore shown as the red curve in Figure 29.

For $n > 1$ it is necessary to account for the degeneracy of KK modes with the same mass m_k. This is simply the degeneracy of an n-dimensional harmonic oscillator,

$$g_k = \binom{n+k-1}{k} . \tag{15.23}$$

The hidden-photon contribution to the IDPB (for a given m_k) must be multiplied by this degeneracy. Note that the degeneracy does not affect the lifetime of the KK modes. Hence only the lower boundary but not the upper boundary are affected.

In Figure 28 the constraints for each value of m_k are plotted for $n = 2$ and the lowest value of $m = 30$ keV. Again it is found that no constraints are obtained for $m_k > 2\,m_e$, and therefore also for $m > 2\,m_e$. Therefore the constrained region is given by $\chi_{min}(m_k = 2\,m_e) \leq \chi(m = 30\,\mathrm{meV}) \leq \chi_{max}(m_k = m = 30\,\mathrm{meV})$. For $n = 2$ this process can be repeated for all $30\,\mathrm{meV} \leq m \leq 2\,m_e$, leading to the orange curve in Figure 29.

The same method can be repeated for larger n. Once again it is found that no constraints are obtained for $m_k > 2\,m_e$, and also for $m > 2\,m_e$. Note that this means that no constraints are produced for $n = 5, 6$ (see Table 1). The constraints for $n = 3$ and $n = 4$ are shown as the brown and green curves respectively in Figure 29.

15.3 Summary of Chapter 15

Hidden photons can be produced in the early universe. If these particles survive to the present day then the the decay process $X \to \gamma + \gamma + \gamma$ contributes to the Intergalactic Diffuse Photon Background (IDPB). A constraint is obtained by imposing that the hidden-photon contribution is larger than the experimentally-observed value.

In order to contribute to constraints the hidden photon needs to survive for the lifetime of the universe t_0, and this results in an upper boundary for constraints.

In the non-KK model constraints are only obtained in the region $m_X \leq 2\,m_e$.

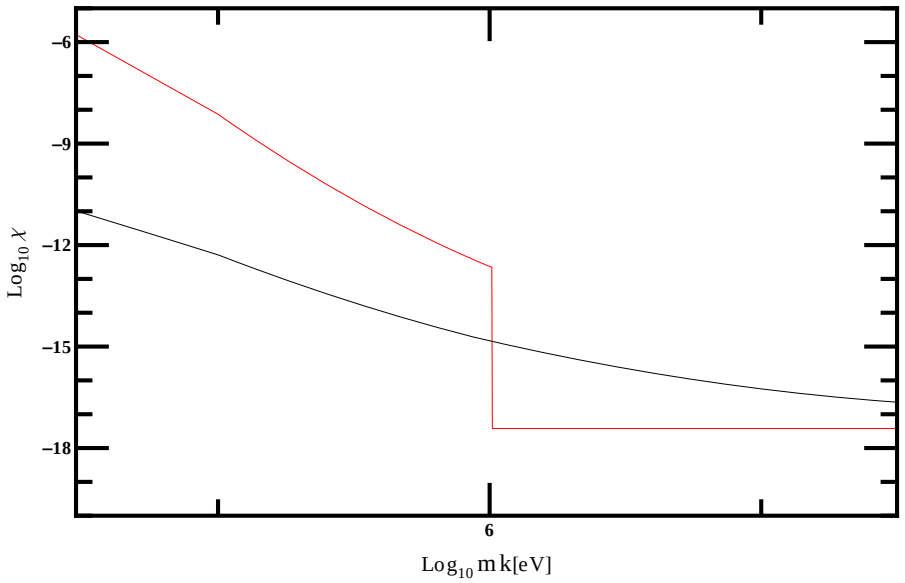

Figure 28: Constraints from the Intergalactic-Diffuse-Photon-Background (IDPB) experiment for the KK model in $n = 2$ extra dimensions with $m = 30$ keV and variable m_k. The upper boundary (red) is from the lifetime of the KK modes. The lower boundary (black) comes from the contribution of all KK modes with m_k to the IDPB. For $m_k > 2\,m_e$ the upper boundary goes below the lower boundary and no constraints are obtained. Therefore the constrained region is given by $\chi_{min}(m_k = 2\,m_e) \leq \chi(m = 30\,\text{keV}) \leq \chi_{max}(m_k = m)$. For $n = 2$ this process can be repeated for all $30\,\text{meV} \leq m \leq 2\,m_e$, leading to the orange curve in Figure 29.

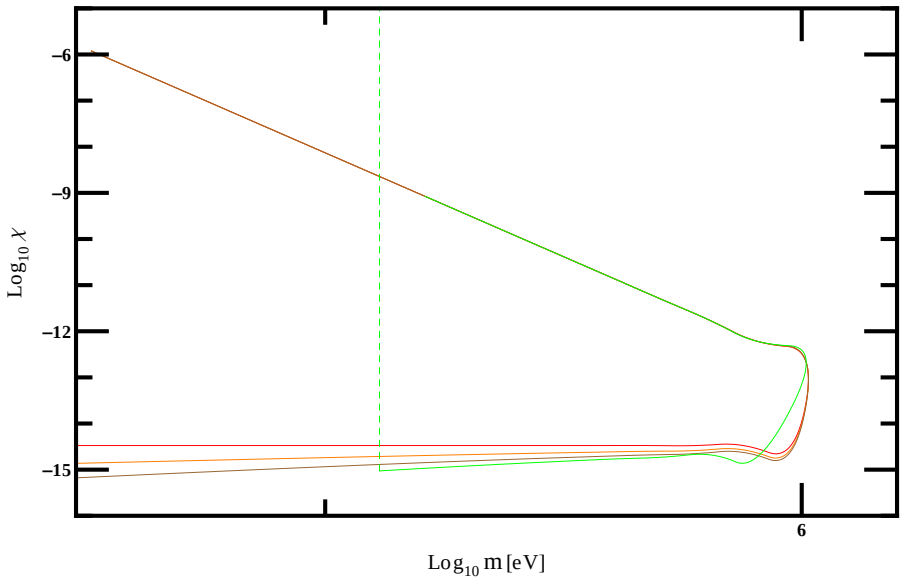

Figure 29: IDPB constraints for the KK model. There are no constraints for $m > 2\,m_e$, because these KK modes decay too quickly (see Chapter 15.1), and therefore no constraints are produced for $n = 5, 6$ (see Table 1). The plotted curves are for $n = 1$ (red), $n = 2$ (orange), $n = 3$ (brown), and $n = 4$ (green) extra dimensions.

For $m_X > 2\,m_e$ the tree-level decay $X \to e^+ + e^-$ becomes available and dramatically decreases the hidden-photon lifetime. Therefore if χ is large enough for the hidden photon to be observed then the lifetime is too small. Conversely if χ is small enough for the hidden photon to survive until the present day, then the coupling is too weak for observation. Hence the region $m_X > 2\,m_e$ is not constrained.

In the KK model no summation over KK modes takes place, because KK modes with different masses m_k contribute to the IDPB at different frequencies. This means that, for a given value of m, different values of m_k actually constrain different values of χ. No constraints are obtained for $m_k > 2\,m_e$, and therefore no constraints are obtained for $m > 2\,m_e$. This occurs for the same reason that no constraints are obtained for $m_X > 2\,m_e$ in the non-KK model. This means that in the KK model constraints are only obtained for $n = 1, ..., 4$, but not $n = 5, 6$. For any given n, m, the constrained region is given by

$\chi_{min}(m_k = 2\,m_e) \leq \chi(m) \leq \chi_{max}(m_k = m)$.

16 SN1987a energy-loss constraints

The basic principle is that the hidden-photon model should respect neutrino energy-loss observations from the supernova explosion. Neutrinos are observed to be emitted over a period of 5-10 seconds at a luminosity of $\sim 10^{53}\,\mathrm{erg\,s^{-1}}$. If the hidden-photon luminosity is too large, that is similar to the neutrino luminosity, then the SN cools too quickly. This conflicts with observation and constrains the hidden photon [14, 38].

16.1 SN1987a constraints for the non-KK model

SN1987a is a Type-II supernova. A core of a massive burned-out star collapses until it reaches a density $\sim (6-10)\times 10^{14}\,\mathrm{g\,cm^{-3}}$, temperature $T_{SN} \sim 30$ MeV, and radius ~ 10 km [126–130]. The core then explodes and emits a burst of neutrinos with luminosity $\sim 10^{53}\,\mathrm{erg\,s^{-1}}$ for around 5-10 seconds [131, 132].

A simple stellar model is assumed. The core is homogeneous, with values of the macroscopic quantities described above. Outside the core exists an approximate vacuum. If a particle escapes from the core and into the vacuum then energy loss occurs.

In contrast with the solar and HB-lifetime experiment (see Chapter 12.1), it is now possible for non-local energy transfer to occur without disturbance to the stellar model. Therefore it is now necessary to account properly for hidden-photon reabsorption. As explained in Chapter 8.1 this leads to constraints with an upper boundary, as can be seen from Figures 31 and 34.

The original calculation is performed for emission of axions [14]. This is then modified for emission of hidden photons [38].

An outline of the derivation of the existing constraint will be presented. However this existing method will be modified in several ways.

First, the constraint from [14, 38] assumes that the electron mass is given by its vacuum value. However in the supernova electrons are highly degenerate with $\mu_e \gg m_e$, where μ_e is the electron chemical potential. Hence it is necessary to account for large corrections to the electron mass.

Second, the effects of hidden-photon scattering will be included.[20]

[20] This work only considers scattering effects in the free-streaming limit. The trapping limit

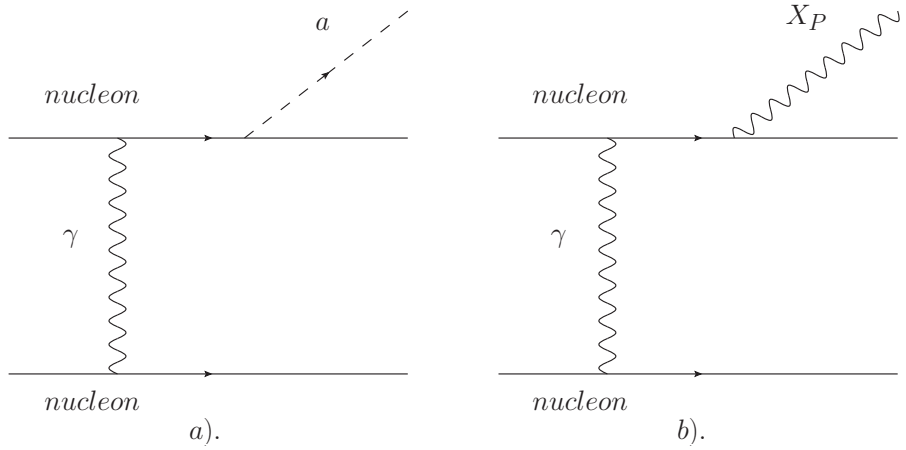

Figure 30: Feynman diagrams for hidden-photon production in SN1987a. The dominant contribution for axion (denoted a) production in SN1987a comes from nucleon-nucleon-axion bremsstrahlung [14, 134], and a schematic Feynman diagram is shown in a). This is modified for hidden-photon emission by substituting the axion with a hidden photon [38], resulting in diagram b).

It should further be observed that the constraint published in [14, 38] does not decay as expected in the limit $m_X \to 0$, but instead saturates. It could be argued that this is not a significant problem, since in this region constraints from other experiments dominate anyway. However the method will be modified to get the proper low-mass decay. This will be achieved in the same way as in the solar-lifetime constraints, by considering the effective coupling for plasma conditions χ_{eff} (see Equation (12.13)).

The dominant contribution for hidden-photon production comes from nucleon-nucleon-axion bremsstrahlung [14, 134]. The luminosity is first calculated for axions, and then modified for hidden photons, as shown in Figure 30.

The calculation of the luminosity of axions is presented in [14]. Rederiving this luminosity is beyond the scope of this work. Instead the calculation is outlined and final result is quoted.

The schematic Feynman diagram for the axion process is shown in Figure 30 a). At the temperature and density of the core, nucleons are nonrelativistic

is considered in [133], but the effect on constraints is minimal.

and nondegenerate [14]. The differential luminosity is found to be [14, 135, 136]

$$\frac{dL_a}{d\omega} = n^2_{\text{nucleon}} \langle \sigma_a v_{M\ddot{o}l} \rangle V \sim \frac{1}{T_{SN}} \times \left(1.7 \times 10^{72}\,\text{erg}\,\text{s}^{-1}\right) g^2\,, \tag{16.1}$$

where $v_{M\ddot{o}l}$ is the relative speed of the colliding particles, the brackets $\langle .....\rangle$ indicate both the thermal and spin average, and V is the core volume. The label g actually represents three different couplings for the three combinations of scattering nucleon; g_{ann}, g_{anp}, g_{app}.

This result can be modified for hidden-photon emission. First it is necessary to multiply by the suppression factor m_p/T_{SN}, where m_p is the proton mass. This accounts for the different nature of spins of the emitted particles [38].

Second it is necessary to make a replacement of the couplings. The final propagating hidden photon should be in the propagation eigenstate X_P. From Equation (10.4) the X_P couples to any electromagnetic current with strength $\sim \chi e$, so the coupling replacement $g \to \chi e$ is made. The schematic Feynman diagram for the bremsstrahlung process is now given by Figure 30 b). Therefore

$$\frac{dL_X}{d\omega} = n^2_{\text{nucleon}} \langle \sigma_X\, v_{M\ddot{o}l} \rangle V \sim \frac{1}{T_{SN}} \times \left(6 \times 10^{69}\,\text{erg}\,\text{s}^{-1}\right) \chi^2\,. \tag{16.2}$$

A Boltzmann suppression factor $e^{-\omega/T_{SN}}$ for thermal production is now included. This leads to proper high-mass decay of the constraint.

It is necessary to account for hidden-photon reabsorption. For the moment only decay and not scattering is considered. Furthermore only the vacuum electron mass is used. This reproduces the published constraint [14, 38]. The supernova has energies $\sim T_{SN} \sim 30\,\text{MeV} < 2\,m_\mu$, so it is possible to ignore decays to $\mu^+ + \mu^-$ or higher-mass fermions. The only important decay is to $e^+ + e^-$. The mean free path is therefore given by Equations (8.2) and (8.4).

Equation (16.2) is then multiplied by the escape factor e^{-l/l_0}, where $l \sim 10$ km is the core radius. Strictly speaking it is necessary to account for the SN radial coordinate, which would produce an integration factor $\sim r^2\, dr\, e^{-(l-r)/l_0}$. However this makes very little numerical difference.

The final luminosity is given by integrating over hidden-photon energies,

$$L_X = \int_{m_X}^{\infty} d\omega\, \frac{1}{T_{SN}} (6 \times 10^{69}) \chi^2 e^{-\frac{\omega}{T_{SN}}} e^{-\frac{l}{l_0}}\,\text{erg}\,\text{s}^{-1}\,. \tag{16.3}$$

Imposing that this is larger than the neutrino luminosity $\sim 10^{53}\,\text{erg}\,\text{s}^{-1}$ reproduces the constraint published in [38]. This is shown as the black curve in Figure

31.

The existing method is now modified. First hidden-photon scattering is included, by again considering Equation (15.17). dN/dV is the number density of produced hidden photons. These are produced with an approximately thermal spectrum, and production is only efficient for $m_X \ll T_{SN}$. Hence the number density is given by

$$\begin{aligned} n_X &\sim \int_{m_X}^{\infty} d^3p_X \frac{g_X}{e^{\frac{E_X}{T_{SN}}} - 1} \sim \int_0^{\infty} d^3E_X \frac{g_X}{e^{\frac{E_X}{T_{SN}}} - 1} \\ &= 2g_X\zeta(2)\, T_{SN}^3 \sim 6.6\, T_{SN}^3 \,, \end{aligned} \tag{16.4}$$

where $g_X = 2$ is the number of (approximately massless) hidden-photon degrees of freedom.

Therefore Equation (15.17) can be rearranged as

$$\Gamma_{\text{scattering}} = \frac{\sigma\, v_{M\ddot{o}l}\, n_{\text{nucleon}}^2}{n_X} \,. \tag{16.5}$$

Comparing this to Equation (16.2) gives

$$\Gamma_{\text{scattering}} \sim \left(\frac{1}{n_X V}\right) \frac{dL_X}{d\omega} \sim 0.9\,\chi^2\,\text{keV} \,. \tag{16.6}$$

The mean free path for scattering is *not* calculated using Equation (8.2). This is because the scattering rate is calculated in the lab frame and not the CM frame of the hidden photon, so that the Lorentz factor is not necessary. The mean free path is instead given by

$$l_{0,\,\text{scattering}} = \frac{1}{(\Gamma_{\text{scattering}}/\text{eV})} \times \left(2 \times 10^{-7}\text{metres}\right) \,, \tag{16.7}$$

where the conversion factor from eV^{-1} to metres has been included.

The proper plasma value for the electron mass will now be included. In the supernova environment electrons are highly degenerate [137]. In this limit the effective electron mass is given by $m_{e,eff} = (\sqrt{3}\, m_\gamma)/2$ [121]. An expression for m_γ is therefore necessary. For highly-degenerate electrons this is given by [107, 109]

$$m_\gamma^2 = \frac{2\alpha\, p_F^2}{\pi v_F} \left[1 - \frac{(1 - v_F^2)}{2v_F} \ln\left(\frac{1 + v_F}{1 - v_F}\right)\right] \,, \tag{16.8}$$

where n_e is the electron density, $E_F = p_F^2 + m_e^2$, $v_F = p_F/E_F$, and $p_F = \left(3\,\pi^2\, n_e\right)^{1/3}$. The number density of electrons is approximately half that of

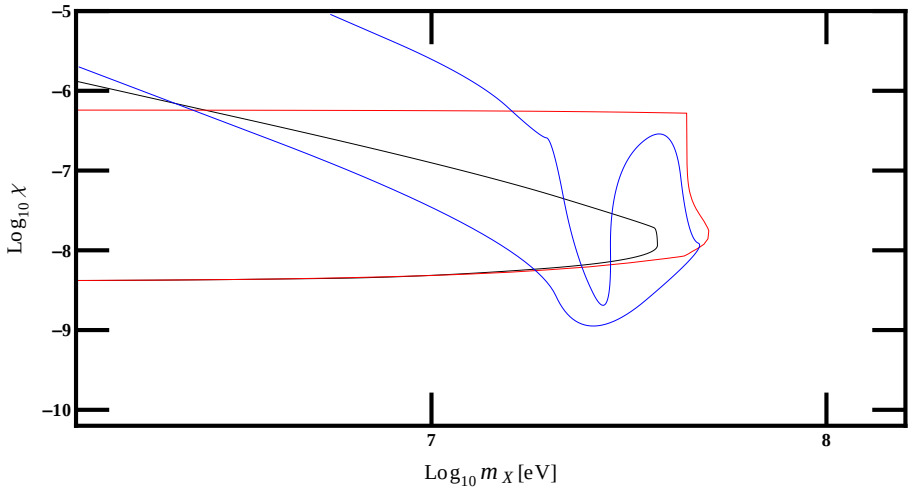

Figure 31: Constraints for the non-KK model from SN1987a energy-loss considerations. The excluded regions are obtained by imposing that the hidden-photon luminosity is larger than that of neutrinos. If this occurs then the supernova cools too quickly, and the extended $(5-10$ seconds) emission of neutrinos would not be observed [14, 38]. Note the presence of an upper boundary for each constraint. This comes from the escape probability factor associated with hidden-photon escape from the supernova core (see Chapter 8.1). The black curve is a reproduction of the published constraint [14, 38]. The method is then modified to account for the increase of the effective electron mass within the supernova and also to account for hidden-photon reabsorption through scattering, producing the red curve. The method is then modified again, with the vacuum kinetic-mixing parameter χ being replaced with the plasma value of the mixing parameter χ_{eff} (see Equation (12.13)). This produces a constraint which decays properly in the limit $m_X \to 0$. There are uncertainties in this constraint associated with uncertainties in the SM-photon mass m_γ, which are shown in Figure 33. The blue curve in the present figure accounts for these uncertainties and is the most conservative form of the constraint.

nucleons. The core is mostly iron with nuclear charge $Z \sim 26$, and mass number $A \sim 56$. The core density $\sim (6-10) \times 10^{14}\,\mathrm{g\,cm^{-3}}$. Taking a mean density of $\rho \sim 8 \times 10^{14}\,\mathrm{g\,cm^{-3}}$ leads to $n_e \sim (1/2)(Z/A) \sim 1.8 \times 10^{24}\,(\mathrm{eV})^3$. Overall $m_\gamma \sim 25.6$ MeV, and $m_{e,eff} \sim 22.1$ MeV.

The mean free path for decay to $e^+ + e^-$ is now given by Equations (8.2) and (8.4), only with $m_e \to m_{e,eff}$.

For masses $m_X > 2\,m_\mu$ there are decays to higher-mass SM particles. There could also be plasma-mass corrections to these other SM particles. For example there could be an increase to the μ^- mass, which would affect the decay $X \to \mu^+ + \mu^-$. However muons are non-degenerate in the supernova, so $\mu_\mu \ll m_\mu$ and there are no significant mass corrections from the chemical potential. Furthermore $T_{SN} \lesssim m_\mu$, so there are no significant mass corrections from temperature. Hence it is possible to assume a vacuum value for the muon mass to a very good approximation. The same applies to all other SM particles with masses $\gtrsim m_\mu$.

In the non-KK model it will be found that constraints actually die off for $m_X \gtrsim 2\,m_\mu$ (see Figures 31 and 33), so extra high-mass decay channels are not important. This is not true in the KK model, where it is necessary to sum over KK modes with $m_k \gtrsim 2\,m_\mu$.

It should be noted that the decay $X \to \gamma + \gamma + \gamma$ also becomes available for $m_X > 3\,m_\gamma$. However this decay is of course suppressed by $O(\alpha^3)$ relative to both $e^+ + e^-$ decay and scattering, and is therefore negligible.

The total mean free path is given by

$$\frac{1}{l_{0,\,\mathrm{total}}} = \frac{1}{l_{0,\,\mathrm{scattering}}} + \frac{1}{l_{0,\,X \to e^+ + e^-}}\,, \tag{16.9}$$

where the only contribution for $m_X \leq 2\,m_{e,eff}$ is from scattering. Substituting this into Equation (16.3) gives the red curve in Figure 31.

The method is now modified to account for proper low-mass decay of the constraint. This is achieved by going back to the original bremsstrahlung process for axions shown in Figure 30 a). In the constraint published in [14, 38] this process is modified for hidden-photon emission by substituting the axion with a hidden-photon propagation eigenstate X_P, giving the diagram in Figure

This substitution process can actually be broken down into an equivalent two-stage process. First the axion is replaced with a SM-photon interaction

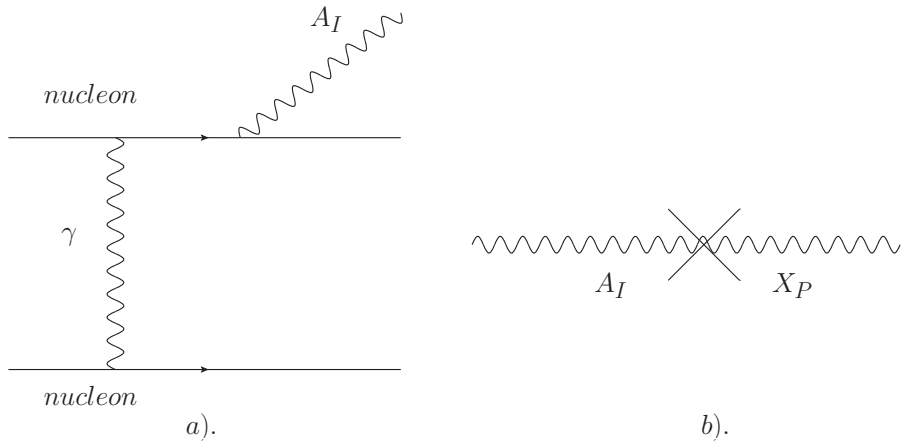

Figure 32: The bremsstrahlung emission of hidden photons (also depicted in Figure 30) can be broken down into two stages. First a SM-photon interaction eigenstate A_I is emitted, as in a). Then this oscillates into a hidden-photon propagation eigenstate X_P, as shown in b). The X_P can generally propagate significant distances, and can sometimes escape from the supernova and contribute to energy loss.

eigenstate A_I, which couples to SM electromagnetic currents with strength e. The emission rate is then multiplied by a suppression factor m_p/T_{SN} to account for the different nature of spins of the emitted particles, and the coupling replacement $g \to e$ is made. This gives the emission rate for A_I bremsstrahlung. The schematic Feynman diagram for this process is shown in Figure 32 a).

A hidden-photon propagation eigenstate X_P can then be produced by the oscillation process $A_I \to X_P$, which is shown in Figure 32 b). For correspondence with the constraint published in [14, 38], the oscillation probability should be set to χ^2. However this neglects resonance effects caused by the plasmon mass m_γ. Once these resonance effects are taken into account, then the oscillation probability is in fact χ^2_{eff} (Equation (12.13)) with $m_\gamma \sim 25.6$ MeV.

Therefore the calculation is repeated with the replacement $\chi \to \chi_{eff}$. The hidden-photon effect now decays as a power law for low masses, and therefore so does the constraint. This is shown as the green curve in Figure 33. Note the resonance spike at $m_X \sim m_\gamma$.

This curve has to be treated with caution. The resonance spike is quite

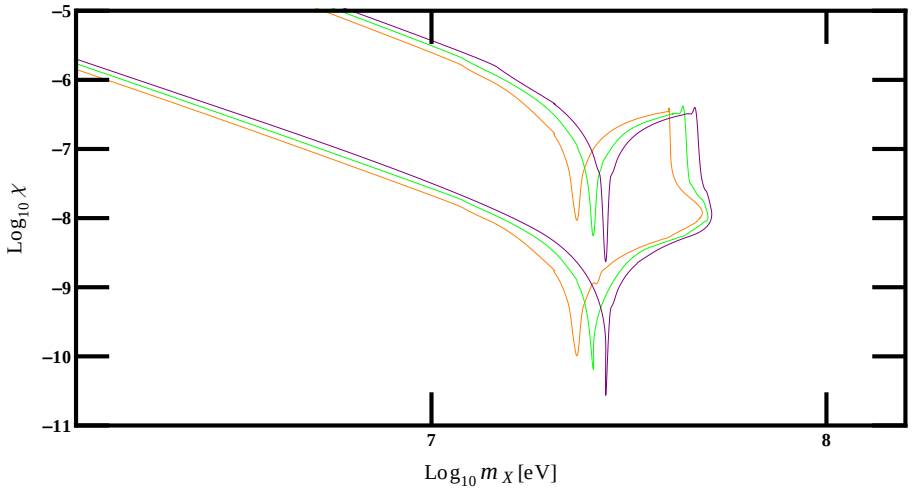

Figure 33: Non-KK constraints from SN1987a energy-loss considerations, which include the effective mixing parameter χ_{eff}. These three curves account for uncertainties in the SM-photon mass. The orange curve assumes the lowest value of $m_\gamma = 23.2$ MeV, the green curve uses the mean value of $m_\gamma = 25.6$ MeV, and the purple curve uses the largest value of $m_\gamma = 27.5$ MeV. These curves all cover slightly different regions of parameter space. A conservative constraint is obtained by taking just the common region. This is shown as the blue curve in Figure 31.

pronounced, and this suggests that the constraint is very strong at the resonance of $m_X \sim m_\gamma$. However there are actually uncertainties associated with the value of m_γ. The major uncertainty comes from the supernova density ρ. The green curve is calculated by assuming a mean value of $\rho = 8 \times 10^{14}\,\mathrm{g\,cm^{-3}}$, which leads to $m_\gamma \sim 25.6$ MeV and $m_{e,eff} \sim 22.1$ MeV. However the supernova model actually assumes a range of densities $\rho = (6 - 10) \times 10^{14}\,\mathrm{g\,cm^{-3}}$, which results in a range $m_\gamma \sim (23.2 - 27.5)$ MeV, and a range $m_{e,eff} = (20.1 - 23.9)$ MeV. Therefore the constraint for the lowest values of m_γ and $m_{e,eff}$ is shown as the orange curve in Figure 33, the constraint with the mean value of of m_γ and $m_{e,eff}$ is shown as the green curve, and the constraint for the highest values of m_γ and $m_{e,eff}$ is shown as the purple curve.

A conservative constraint is therefore produced from the region which is excluded by all three curves. This final, conservative constraint is shown as the blue curve in Figure 31, and also as the green region in the summary Figure 1.

16.2 SN1987a energy-loss constraints for the KK model

The method from Chapter 16.1, which uses the plasma-modified kinetic mixing χ_{eff} (Equation (12.13)), is used. The KK-model constraint is obtained by summing over KK modes in the usual manner.

In the KK model it is necessary to sum over KK modes with masses $m_k \gtrsim 2\,m_\mu$, and therefore to account for extra high-mass decay channels. The decay rate for these channels is given by Equations (11.14) and (11.15).

This is a real-production experiment, with hidden photons produced thermally. Hence the production of very high-mass KK modes is exponentially suppressed and the total hidden-photon effect is always UV finite (see Chapter 6.1). Hence there is no need to introduce an UV cutoff $M_c = aM_*$, and constraints have no uncertainties from the parameter a.

The final constraints are shown in Figure 34.[21] The different curves are for different numbers of extra dimensions; $n = 1$ (red), $n = 2$ (orange), $n = 3$

[21] Note that, as in the model non-KK model, there are uncertainties associated with m_γ. However in the KK model these uncertainties produce a negligible numerical modification to constraints and therefore can be ignored to a very good approximation.

(brown), $n = 4$ (green), $n = 5$ (blue), and $n = 6$ (purple). Constraints are only produced for the range of m stated in Table 1.

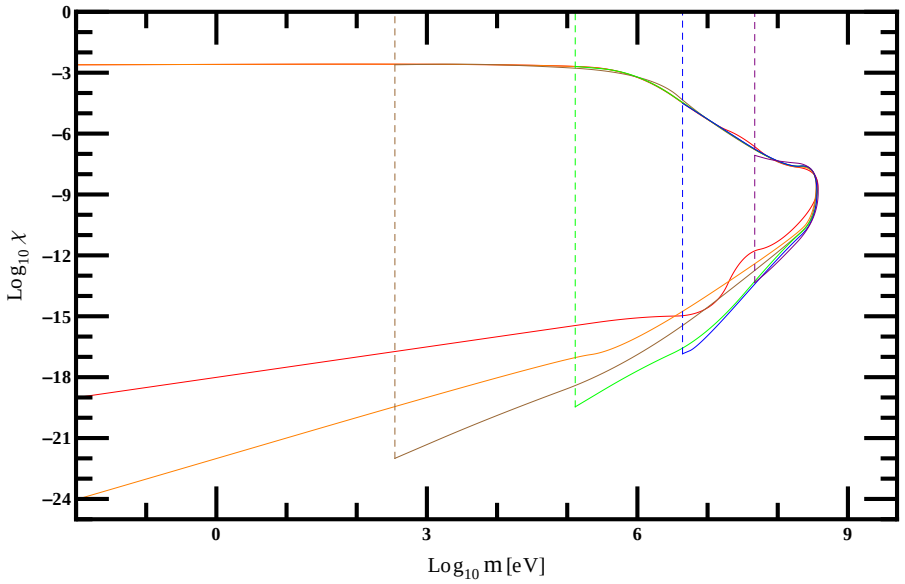

Figure 34: Constraints for the KK model from SN1987a energy-loss considerations. The different curves are for different numbers of extra dimensions; $n = 1$ (red), $n = 2$ (orange), $n = 3$ (brown), $n = 4$ (green), $n = 5$ (blue), and $n = 6$ (purple). Constraints are only produced for the range of m stated in Table 1. This is a real-production experiment, with hidden photons produced thermally. Hence the production of very high-mass KK modes is exponentially suppressed and the total hidden-photon effect is always UV finite (see Chapter 6.1). Hence there is no need to introduce an UV cutoff $M_c = aM_*$, and constraints have no uncertainties from the parameter a.

16.3 Summary of Chapter 16

Hidden photons can be produced in the SN1987a event. On escape these hidden photons contribute to energy loss. If the hidden-photon effect is larger than that of neutrinos then the supernova cools too quickly, in contradiction with observations. This constrains the hidden photon.

The existing constraint [14, 38] for the non-KK model is reproduced. This

constraint is then modified to account for the proper plasma value of the electron mass, and also to account for hidden-photon scattering within the supernova.

Furthermore the effects of the plasma-modified kinetic mixing χ_{eff} are included. This results in a proper low-mass decay for the constraint. It also produces a resonance spike for $m_X \sim m_\gamma$. There are uncertainties associated with this spike which come from uncertainties in m_γ. These uncertainties are accounted for, producing a conservative constraint. This final constraint is shown in the blue curve in Figure 33.

KK constraints are produced by summing over KK modes. These are shown in Figure 34. This is a real-production experiment, with hidden photons produced thermally. Hence the production of very high-mass KK modes is exponentially suppressed and the total hidden-photon effect is always UV finite (see Chapter 6.1). Hence there is no need to introduce an UV cutoff $M_c = aM_*$, and constraints have no uncertainties from the parameter a.

17 Summary and Conclusions

This work combines the minimal-hidden-photon model with the paradigm of Large Extra Dimensions (LED).

This is a toy model, and therefore simple assumptions are generally made. For example it is assumed that the hidden photon is the only hidden-sector particle. This is denoted the "minimal" hidden-photon model. An extension of this work is to investigate a non-minimal hidden-photon model. The most obvious such extension is simply the inclusion of a single hidden fermion.

Furthermore simple assumptions are made about the bulk geometry. It is assumed that the brane corresponds to the visible $(3 + 1)$-dimensional world, and all extra dimensions are transverse to the brane. It is further assumed that the bulk geometry could be factorised into brane $\times$ extra dimensions, and that the extra dimensions could themselves be individually factorised. Finally it is assumed that the extra dimensions are toroidally compactified and are all of the same length.

The model has two mass parameters m and M_*, where m is both the mass of the lowest KK mode and the mass separation of KK modes, and M_* is the proper higher-dimensional Planck scale. There exist lower limits on both of these mass parameters. Table-top gravitational constraints impose $m \gtrsim 10$ meV [45, 46]. It is also imposed that $M_* \gtrsim 1$ TeV for agreement with current experimental data. However these two mass parameters are not independent, but are related by

$$M_{pl}^2 = M_*^{2+n} \left(\frac{2\pi}{m}\right)^n , \tag{17.1}$$

where n is the number of extra dimensions and M_{pl} is the 4-dimensional Planck mass. Hence for any given number of extra dimensions n, the lower limit from only one of either m or M_* is effective. For $n = 1, 2$ the effective lower limit comes from the parameter m. For $n = 3, ..., 6$ the effective lower limit comes from the higher-dimensional Planck scale M_*. Constraints are only produced for allowed values of m, which are shown in Table 1.

The hidden-photon Lagrangian is then extended to n extra dimensions. The presence of the brane breaks higher-dimensional Lorentz invariance, and therefore higher-dimensional Lorentz-breaking and brane-localising hidden-photon

terms are generally allowed. However in this work it is assumed that these terms are negligible in comparison with the higher-dimensional Lorentz-preserving hidden-photon kinetic term. An important extension of this work is the proper treatment of these neglected terms. This may significantly alter the phenomenology of the model.

A 4-dimensional Lagrangian is obtained by integrating out the extra dimensions. The SM photon is confined to the brane, and therefore does not gain a tower of KK modes. This is in accordance with experiment. The hidden photon and graviton are allowed to propagate throughout the bulk, and therefore gain a tower of KK modes.

In this scenario the hidden-photon KK modes automatically become massive, and therefore physically observable. These masses emerge naturally from the geometry, without the need for an additional Higgs or Stueckelberg mass term. Such a Higgs or Stueckelberg mass term is not considered, but this is a good candidate for further work.

The total hidden-photon effect is obtained by summing over KK modes. This generally includes contributions from arbitrarily-high-mass modes, which could potentially cause UV divergences. This possibility is investigated.

It is found that real-production experiments always contain an experimentally-imposed upper limit for the mass of KK modes. Hence the total hidden-photon effect does not receive contributions from arbitrarily-high-mass modes and is always UV finite.

However virtual-production experiments contain no such upper limit for KK modes. Naïvely attempting to sum up to a KK number of $k = \infty$ generally produces UV divergences. The theory can be saved by introducing an UV cutoff for the mass of KK modes. This is justified because the theory is essentially an effective theory, and is only expected to hold up to a certain mass scale. The UV cutoff should be similar to M_*. However it may deviate from M_* due to some unknown high-energy physical factors which are not explicitly present in the low-energy-effective theory. Therefore the UV cutoff is set as $M_c = aM_*$, where a is an uncertainty parameter. M_c should be within an order of magnitude or so of M_*, and a is therefore allowed to vary in the range $0.1 - 10$.

However there exists a more serious issue with virtual-production experi-

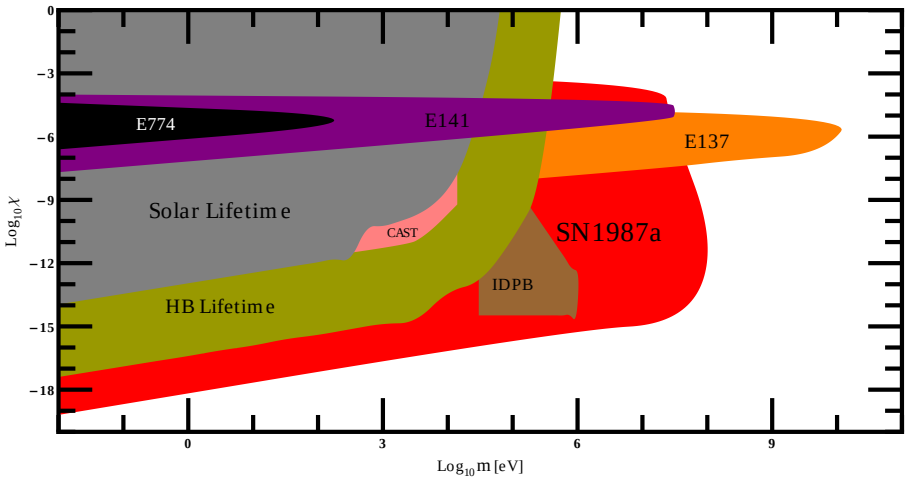

Figure 35: Summary plot for KK constraints with $n = 1$ extra dimensions. For $n = 1$, $m \leq 10$ meV is already experimentally excluded (see Table 1), so constraints are only produced for $m \geq 10$ meV. The red constraint is from energy loss in SN1987a. The brown constraint is from the Intergalactic-Diffuse-Photon-Background (IDPB) experiment. The dark-green constraint is from HB-lifetime considerations. The pink constraint is from the CERN Axion Solar Telescope (CAST) experiment. The grey constraint is from solar-lifetime considerations. The orange (E137), purple (E141), and black (E774) constraints are from fixed-target experiments.

ments. It is necessary for the effective perturbation parameter to be $\ll 1$ in order for the perturbative treatment to be valid. This imposes an upper boundary on constrained values of χ. It is found that if χ is large enough such that the hidden photon could be observed, the effective perturbation parameter becomes so large that the perturbative treatment breaks down. Hence the present method does not produce any constraints from virtual-production experiments.

Constraints for the KK model are summarised in Figures 35 - 40. These apply only for the allowed values of m, which are shown in Table 1.

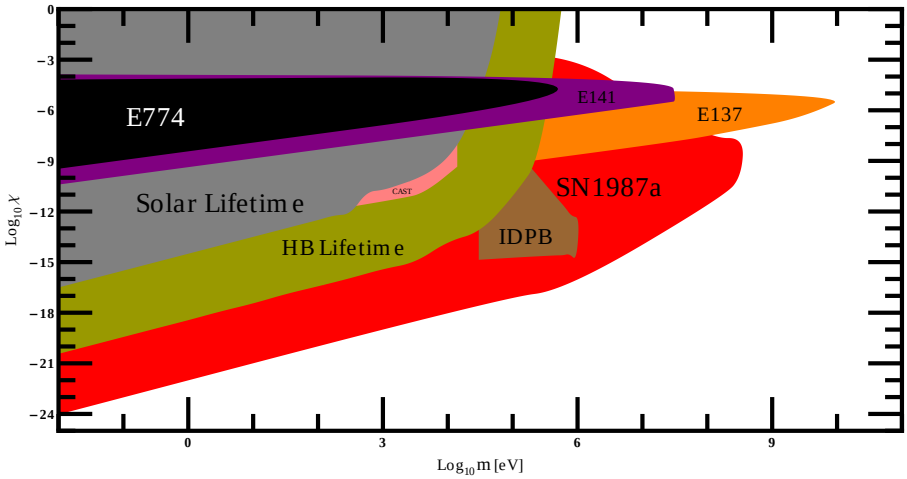

Figure 36: Summary plot for KK constraints with $n = 2$ extra dimensions. For $n = 2$, $m \leq 10$ meV is already experimentally excluded (see Table 1), so constraints are only produced for $m \geq 10$ meV. The red constraint is from energy loss in SN1987a. The brown constraint is from the Intergalactic-Diffuse-Photon-Background (IDPB) experiment. The dark-green constraint is from HB-lifetime considerations. The pink constraint is from the CERN Axion Solar Telescope (CAST) experiment. The grey constraint is from solar-lifetime considerations. The orange (E137), purple (E141), and black (E774) constraints are from fixed-target experiments.

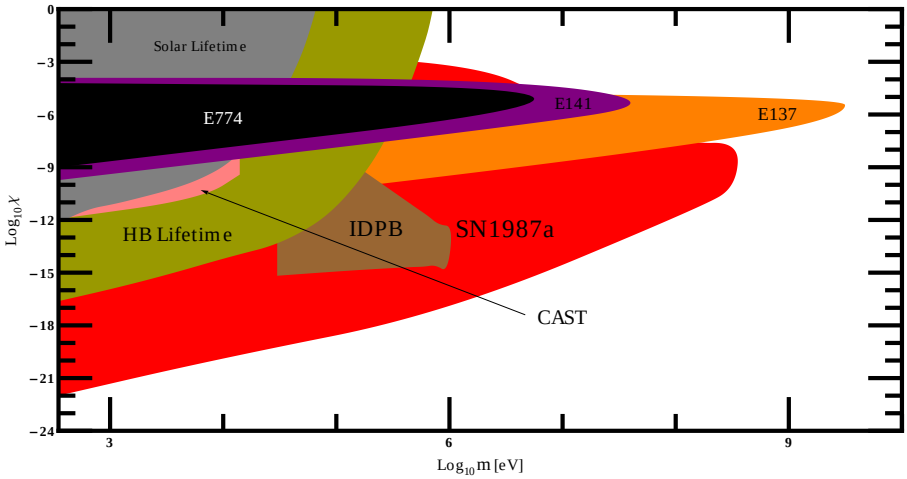

Figure 37: Summary plot for KK constraints with $n = 3$ extra dimensions. For $n = 3$, $m \leq 0.35$ keV is already experimentally excluded (see Table 1), so constraints are only produced for $m \geq 0.35$ keV. The red constraint is from energy loss in SN1987a. The brown constraint is from the Intergalactic-Diffuse-Photon-Background (IDPB) experiment. The dark-green constraint is from HB-lifetime considerations. The pink constraint is from the CERN Axion Solar Telescope (CAST) experiment. The grey constraint is from solar-lifetime considerations. The orange (E137), purple (E141), and black (E774) constraints are from fixed-target experiments.

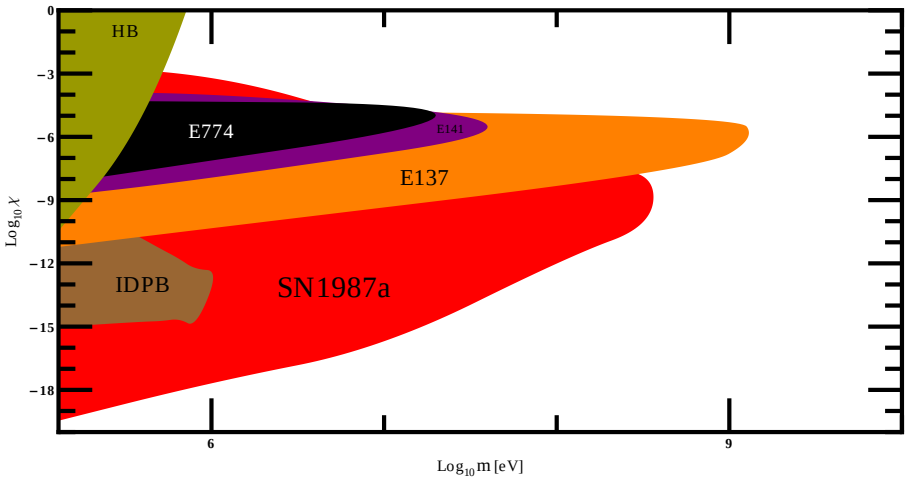

Figure 38: Summary plot for KK constraints with $n = 4$ extra dimensions. For $n = 4$, $m \leq 0.13$ MeV is already experimentally excluded (see Table 1), so constraints are only produced for $m \geq 0.13$ MeV. The red constraint is from energy loss in SN1987a. The brown constraint is from the Intergalactic-Diffuse-Photon-Background (IDPB) experiment. The dark-green constraint is from HB-lifetime considerations. The orange (E137), purple (E141), and black (E774) constraints are from fixed-target experiments. For $n = 4$ no constraints are produced from the solar-lifetime or CAST experiments, because the energy scales of these experiments ($\lesssim 0.1$ MeV) are too low.

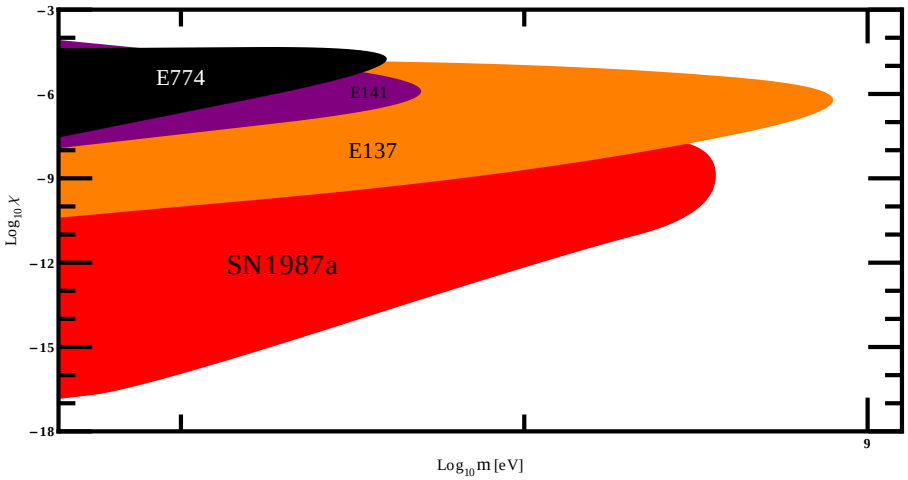

Figure 39: Summary plot for KK constraints with $n = 5$ extra dimensions. For $n = 5$, $m \leq 4.4$ MeV is already experimentally excluded (see Table 1), so constraints are only produced for $m \geq 4.4$ MeV. The red constraint is from energy loss in SN1987a. The brown constraint is from the Intergalactic-Diffuse-Photon-Background (IDPB) experiment. The orange (E137), purple (E141), and black (E774) constraints are from fixed-target experiments. For $n = 5$ no constraints are produced from the solar-lifetime, HB-lifetime, CAST, or IDPB experiments, because the energy scales of these experiments ($\lesssim 1$ MeV) are too low.

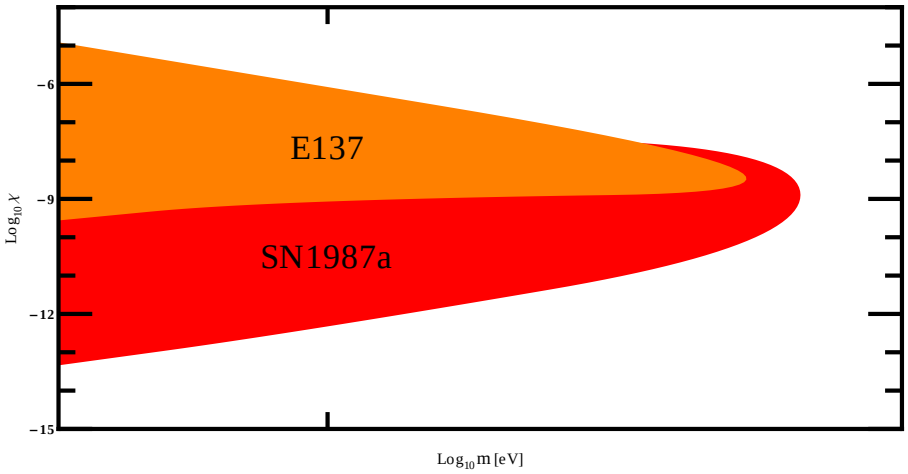

Figure 40: Summary plot for KK constraints with $n = 6$ extra dimensions. For $n = 6$, $m \leq 47$ MeV is already experimentally excluded (see Table 1), so constraints are only produced for $m \geq 47$ MeV. The red constraint is from energy loss in SN1987a. The brown constraint is from the Intergalactic-Diffuse-Photon-Background (IDPB) experiment. For $n = 6$ no constraints are produced from the solar-lifetime, HB-lifetime, CAST, IDPB, E141, or E774 experiments.

A $X \to \gamma + \gamma + \gamma$ rate from electron loop for $m_X \gtrsim 2\,m_e$

The decay rate for $Z \to +\gamma + \gamma + \gamma$ is taken from [138–141],

$$\Gamma_{Z\to\gamma+\gamma+\gamma} = \alpha^3 \alpha_Z \left(3 \sum_q Q_q^3 v_q + \sum_l Q_l v_l \right)^2 \times \frac{M_Z}{72\pi^3} \times N\,, \tag{A.1}$$

where

$$N = 200\zeta_5 - 8\pi^2\zeta_3 + (7/15)\pi^4 - 128\zeta_3 + (41/3)\pi^2 - 124 \sim 15\,, \tag{A.2}$$

$\alpha_Z = \alpha/(\sin^2\theta_W \cos^2\theta_W)$, q represents quark channels, l represents lepton channels, and Q is the fractional electric charge in units of e.

This can be transformed into the electron loop contribution to the decay rate for $X \to \gamma + \gamma + \gamma$ in the region $m_X \gtrsim 2\,m_e$. First the extra quark and lepton decay channels are ignored. Then the replacement $\alpha_Z \to \chi^2\alpha$ must be made, in order to account for the different coupling strengths of the Z boson and the hidden photon.

The Z coupling to the electron has a vector part given by $(1/2)\bar{\psi}\,\gamma^\mu\,\psi\,g_z\,v_e$, plus an axial part. Note that v_e gives the vector charge in units of the vector coupling constant g_z. The hidden photon decay only has a vector part. Comparing the weak neutral current to the electromagnetic one it can be seen that the replacement $(1/2)v_e \to Q_e = 1$, or $v_e \to 2$, must be made. Overall this gives the decay rate in Equation (8.1).

B Contribution to $X \to \gamma + \gamma + \gamma$ from high-mass SM particles

The dominant contribution to the loop decay $X \to \gamma + \gamma + \gamma$ occurs when an electron is in the loop. The Feynman diagram for this process is shown in Figure 4. The rate for this process is given by Equation (8.1).

There are also contributions to the loop decay $X \to \gamma + \gamma + \gamma$ from a SM fermion f^-, which has $m_f > m_e$. The decay rate for these extra contributions is given by

$$\begin{aligned} \Gamma_{X\to\gamma+\gamma+\gamma} &\sim \frac{17\alpha^4\chi^2 m_X^9}{11664000\,\pi^3\,m_f^8}, && m_X \lesssim m_f, \\ &\sim (2.5\times 10^{-2})\chi^2\alpha^4 m_X, && m_X \gtrsim m_f\,. \end{aligned} \tag{B.1}$$

In the region $m_X \lesssim m_f$ the loop contribution for the fermion f is always smaller than the contribution from the electron loop. This can be seen by comparing Equations (8.1) and (B.1), and noting that $m_f > m_e$. However in the region $m_X \gtrsim m_f$ the contribution from the fermion f is actually very similar to the one from the electron loop. However in this region the loop decay is highly suppressed by tree-level decays of the form $X \to e^+ + e^-$ and $X \to f^+ + f^-$ etc. Hence these extra f-loop contributions are always irrelevant.

At electroweak energies there are also contributions with W and Z bosons in the loop. However these are of a similar order of magnitude to the extra fermionic contributions [141]. In this region the loop decay is again highly suppressed relative to tree-level decays, so these extra boson-loop contributions are again irrelevant.

C Decay rate for $X \to \gamma + G$ in the non-KK model

This section calculates the rate for a hidden photon with mass m_X to decay to a SM photon with mass m_γ and a graviton with mass m_G.

The interaction Lagrangian is given by [61]

$$\mathcal{L} = -\frac{\chi G_{\mu\nu}}{2\sqrt{2}M_{pl}}\Big(- \eta^{\mu\nu}F_{\rho\sigma}X^{\rho\sigma} + 4F^{\mu}{}_{\sigma}X^{\nu\sigma}\Big)\,. \tag{C.1}$$

The Feynman amplitude is given by taking the functional derivative with respect to the graviton field,

$$\begin{aligned}\frac{\delta\mathcal{L}}{\delta G_{ij}(k_G)} &= -\frac{\chi\delta^i_\mu\delta^j_\nu}{2\sqrt{2}M_{pl}}\Big(- \eta^{\mu\nu}F_{\rho\sigma}X^{\rho\sigma} + 4F^{\mu}{}_{\sigma}X^{\nu\sigma}\Big)\\ &= -\frac{\chi}{2\sqrt{2}M_{pl}}\Big(- 2\eta^{ij}(\partial_\rho A_\sigma\partial^\rho X^\sigma - \partial_\sigma A_\rho\partial^\rho X^\sigma)\\ &\quad + 4(\partial^i A_\sigma\partial^j X^\sigma - \partial^\sigma A_i\partial^j X^\sigma - \partial^i A_\sigma\partial^\sigma S^j + \partial_\sigma A^i\partial^\sigma S^j)\Big)\,,\end{aligned} \tag{C.2}$$

followed by the SM-photon field,

$$\begin{aligned}\frac{\delta\mathcal{L}}{\delta G_{ij}(k_G)\delta A_k(k_\gamma)} = -\frac{i\chi}{2\sqrt{2}M_{pl}}\Big[&-2\eta_{ij}(k_{\gamma\rho}\delta^k_\sigma\partial^\rho X^\sigma - k_{\gamma\sigma}\delta^k_\rho\partial^\rho X^\sigma)\\ &+ 4\Big(k^i_\gamma\delta^k_\sigma(\partial^j X^\sigma - \partial^\sigma S^j) + k_{\gamma\sigma}\eta^{ik}(\partial^\sigma S^j - \partial^j X^\sigma)\Big)\Big]\,,\end{aligned} \tag{C.3}$$

and finally the hidden-photon field,

$$\begin{aligned}M^{ijkl} &= \frac{\delta\mathcal{L}}{\delta G_{ij}(k_G)\delta A_k(k_\gamma)\delta X_l(k_X)}\\ &= \frac{-\chi}{\sqrt{2}M_{pl}}\Big(\eta^{ij}(k_\gamma.k_X\eta^{kl} - k^l_\gamma k^k_X) + 2k^i_\gamma(k^k_X\eta^{lj} - k^j_X\eta^{lk}) + 2\eta^{ik}(k^l_\gamma k^j_X - 2(k_\gamma\cdot k_X)\eta^{jl})\Big)\,.\end{aligned} \tag{C.4}$$

All external particles are on-shell, so it is necessary to multiply by the polarization tensors $\epsilon^{ij}(k_G)$, $\epsilon^k(k_\gamma)$, $\epsilon^l(k_X)$. These polarization tensors also contain spin indices, which are not written explicitly.

The amplitude is now squared, the initial and final states are summed over. This uses the completeness relations $\sum_{\text{spins}}\epsilon^*_\mu\epsilon_\nu = \eta_{\mu\nu}$, $\sum_{\text{spins}}\epsilon^*_{\mu\nu}\epsilon_{\rho\sigma} = B_{\mu\nu\rho\sigma}$, where [61]

$$\begin{aligned}B_{\mu\nu\rho\sigma}(p) &= \left(\eta_{\mu\rho} - \frac{p_\mu p_\rho}{m_G^2}\right)\left(\eta_{\nu\sigma} - \frac{p_\nu\, p_\sigma}{m_G^2}\right)\\ &+ \left(\eta_{\mu\sigma} - \frac{p_\mu\, p_\sigma}{m_G^2}\right)\left(\eta_{\nu\rho} - \frac{p_\nu\, p_\rho}{m_G^2}\right) - \frac{2}{3}\left(\eta_{\mu\nu} - \frac{p_\mu\, p_\nu}{m_G^2}\right)\left(\eta_{\rho\sigma} - \frac{p_\rho p_\sigma}{m_G^2}\right)\,.\end{aligned} \tag{C.5}$$

The squared amplitude which is averaged over initial spins and summed over final spins is denoted as $\overline{|M|^2}$. This is given by

$$\begin{aligned}\overline{|M|^2} &= M_{ijkl} M_{wxyz} \left(\frac{1}{n_s}\right) \sum_{\text{spins}} (\epsilon^{*ij}\epsilon^{wx})(\epsilon^{*k}\epsilon^{y})(\epsilon^{*l}\epsilon^{z}) \\ &= M_{ijkl} M_{wxyz} \left(\frac{1}{n_s}\right) B^{ijwx}(k_G)\, \eta^{ky}\, \eta^{lz}\,, \end{aligned} \tag{C.6}$$

where $n_s = 3$ is the number of initial spins. Note that the massless hidden photon has 2 spin degrees of freedom, but does not decay.

The calculation is performed in the rest frame of the decaying hidden photon. It is immediately possible to write down the following relations

$$\begin{aligned} &k_X \cdot k_X = m_X^2,\ \ k_\gamma \cdot k_\gamma = m_\gamma^2,\ \ k_G \cdot k_G = m_G^2, k_X \cdot k_\gamma = m_X\, E_\gamma, \\ &k_X \cdot k_G = m_k\, E_G,\ \ k_X \cdot k_G = E_X E_G - |\vec{k}_X||\vec{k}_G| \cos\theta\,. \end{aligned} \tag{C.7}$$

E_G is given by

$$\begin{aligned} k_\gamma^2 &= m_\gamma^2 = (k_X - k_G)^2 \\ &= k_X^2 + k_G^2 - 2\, k_X \cdot k_G \\ &= m_X^2 + m_G^2 - 2\, m_X E_G \\ \to E_G &= \frac{m_X^2 + m_G^2 - m_\gamma^2}{2\, m_X}\,. \end{aligned} \tag{C.8}$$

E_γ is solved in a similar fashion.

A general expression for the decay rate is given by [91]

$$\Gamma = \int \frac{1}{m_X} \left(\frac{d^3\vec{k}_\gamma}{(2\pi)^3}\frac{1}{E_\gamma}\right) \left(\frac{d^3\vec{k}_G}{(2\pi)^3}\frac{1}{E_G}\right) \times \overline{|M|^2} \times (2\pi)^4 \delta^4(k_X - k_\gamma - k_G)\,. \tag{C.9}$$

where in the rest frame of the decaying hidden photon $k_X = (m_X, 0)$, $k_\gamma = (E_\gamma, \vec{k}_\gamma)$, $k_G = (E_G, \vec{k}_G)$. Integrating over $\vec{k}_G$ enforces $\vec{k}_\gamma = \vec{k}_G$,

$$\Gamma = \int \frac{1}{32\pi^2 m_X} \left(\frac{d^3\vec{k}_\gamma}{E_\gamma\, E_G}\right) \overline{|M|^2}\ \delta(m_X - E_\gamma - E_G)\,. \tag{C.10}$$

Transforming to spherical-polar coordinates

$$\begin{aligned} d^3\vec{k}_\gamma &= d|\vec{k}_\gamma||\vec{k}_\gamma|^2 \times 2\pi \times d(\cos\theta) \\ &= E_\gamma\, dE_\gamma |\vec{k}_\gamma| \times 2\pi \times d(\cos\theta)\,, \end{aligned} \tag{C.11}$$

where θ is the angle between the vectors $\vec{k}_X$ and $\vec{k}_G$. Finally,

$$\Gamma(X \to \gamma + G) = \int_0^\pi \frac{1}{16\pi m_X} \frac{|\vec{k}_\gamma|}{E_G} \ \overline{|M|^2} \ d(\cos\theta)\,. \tag{C.12}$$

This is the rate for a hidden photon with mass m_X to decay to a graviton with mass m_G plus a SM photon. This decay is proportional to $1/M_{pl}^2$ and is therefore highly suppressed.

Setting $m_X = 0$ and $m_G = 0$,

$$\Gamma(X \to \gamma + G)\Big|_{m_G=0, m_\gamma=0} = \frac{\chi^2 m_X^2}{12\pi M_{pl}^2}\,. \tag{C.13}$$

D High-mass decay in atomic spectra

In Chapter 9.1.3 it is shown that the hidden-photon effect decays as a power law as $m_X \to \infty$ (see Equation (9.28)). However this result may be slightly naïve, since it assumes a pointlike nucleus (see Equation (9.1)). It is conceivable that the inclusion of finite-nuclear-size effects might substantially modify the high-mass hidden-photon effect. The true decay could possible be a modified power law or even exponential form. This modification would occur for hidden-photon mass scales $\gtrsim 1/r_{\text{nucleus}}$. In atomic hydrogen this corresponds to $m_X \gtrsim 1/r_p \sim$ 200 MeV. It is therefore necessary to investigate the effects of finite-nuclear size on constraints.

The non-KK model is considered first.

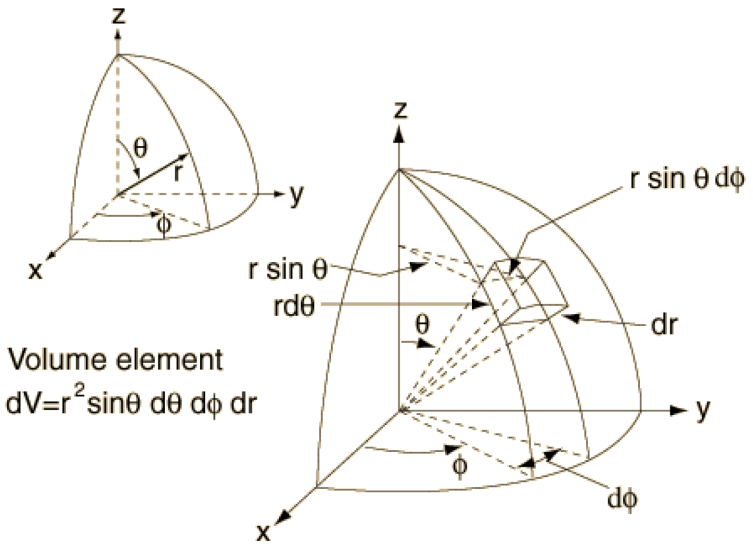

Figure 41: Charge element of a homogeneous spherical nucleus, with volume $r^2\, dr\, \sin\theta\, d\theta\, d\phi$. The figure is reproduced from [142].

The considered transition is the $2\,s_{1/2} - 2\,p_{1/2}$ Lamb shift in atomic hydrogen. However this time the nucleus is modelled as an homogeneous sphere of charge with radius r_p. The atom has spherical symmetry, so it is possible to work in spherical-polar coordinates.

The potential is calculated at a point $(0, 0, \rho)$. A charge element located at $(r\sin\theta\cos\phi, r\sin\theta\sin\phi, r\cos\theta)$ is considered, as shown in Figure 41. This

element has volume $r^2\,dr\,\sin\theta\,d\theta\,d\phi$ and charge

$$\delta Q = \left(\frac{3}{4\pi r_p^3}\right) r^2\,dr\,\sin\theta\,d\theta\,d\phi\,. \tag{D.1}$$

The distance between the charge element and the point $(0,0,\rho)$ is

$$d = \sqrt{r^2 - 2r\rho\cos\theta + \rho^2}\,. \tag{D.2}$$

The potential at $(0,0,\rho)$ due to this element is therefore given by

$$\delta V = -\left(\frac{3}{4\pi r_p^3}\right) r^2\,dr\,\sin\theta\,d\theta\,d\phi \times \frac{\alpha}{d}(1+\chi^2 e^{-m_X d})\,. \tag{D.3}$$

The total potential at $(0,0,\rho)$ is given by summing over all elements within the sphere. Because of spherical symmetry this gives the total potential at any distance ρ from the centre of the nucleus,

$$V(\rho) = -\int_0^{r_p}\int_0^{\pi}\left(\frac{3}{2r_p^3}\right) r^2\,dr\,\sin\theta\,d\theta \times \frac{\alpha}{d}(1+\chi^2 e^{-m_X d})\,. \tag{D.4}$$

Note that there are different expressions for the potential in the regions $\rho < r_p$ and $\rho > r_p$.

The hidden-photon effect is calculated in 1^{st}-order perturbation theory using Equation (9.2). A constraint is imposed by imposing that this is larger than the uncertainty $2\,\widetilde{\Delta M} = 2\times 10^{-10}$ eV, where $\widetilde{\Delta M}$ is defined by Equation (9.6). This is plotted as the green curve in Figure 42. For comparison the constraint that assumes a pointlike nucleus is plotted as the black curve.

The high-mass behaviours of both constraints are almost identical. Hence finite-nuclear-size effects do not significantly modify the high-mass hidden-photon effect. This result generalises straightforwardly to other transitions in atomic spectra.

For the non-KK model this result is actually not very significant. This is because in the high-mass region $m_X \gtrsim 1/r_p \sim 200$ MeV constraints have already died off to to $\chi \gtrsim 0.1$ (see for example Figure 6). In this region the perturbative treatment of χ has broken down anyway, and constraints are not very meaningful.

However the KK model is very different. There are now contributions from KK modes with masses $\gtrsim 200$ MeV, so the precise high-mass behaviour of the hidden photon becomes physically important. Therefore the total hidden-photon effect in the KK model is straightforwardly obtained by calculating the

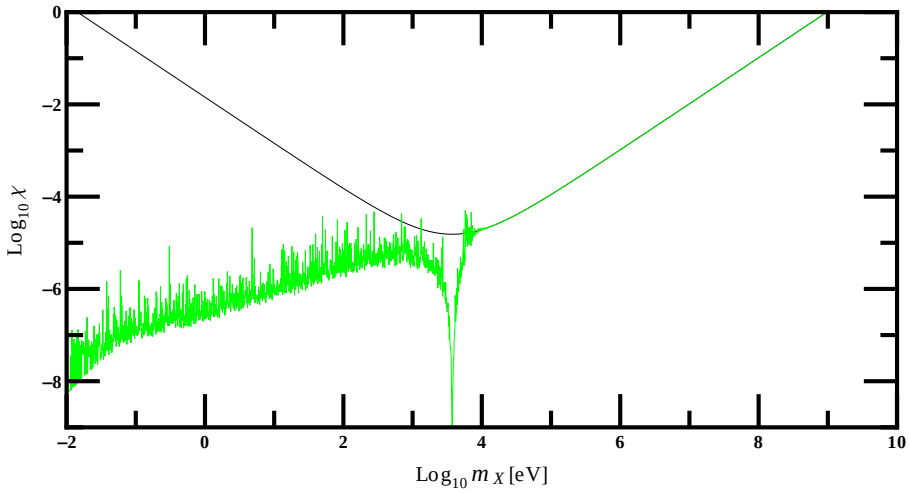

Figure 42: Non-KK constraints from the $2\,s_{1/2} - 2\,p_{1/2}$ transition in atomic hydrogen. The black curve assumes a pointlike nucleus, whereas the green curve models the nucleus as a homogeneous sphere of charge with radius equal to the proton radius $r_p \sim 1/(200\,\mathrm{MeV})$. The high-mass decays for both cases are almost identical, indicating that finite-nuclear-size effects do not substantially modify high-mass hidden-photon effects. There is an irrelevant modification to low-mass effects, and this is discussed in Appendix D.1.

the contribution of an individual KK mode in perturbation theory (see Equation (9.2)), using a pointlike nucleus (see Equation (9.1)), and summing over the contributions from each KK mode using Equation (6.1).

D.1 Low-mass behaviour with finite-nuclear-size effects

The low-mass behaviour of the two constraints in Figure 42 is different.

First consider the constraints with a pointlike nucleus. From Equation (9.1), the perturbation to the potential becomes an exact Coulomb law in the limit $m_X \to 0$. The 0^{th}-order energies (given by $E^{D,R}_{n,j}$ in Equation (9.3)) for the $2\,s_{1/2}$ and $2\,p_{1/2}$ states are identical for a perfect Coulomb law, so the perturbation given by Equation (9.2) is zero. Hence the hidden-photon effect dies off in the limit $m_X \to 0$, and so does the hidden-photon constraint (the black curve).

However if a spherical distribution of nuclear charge is assumed then the

perturbation given by Equation (9.2) includes the effects of finite-nuclear size. This is a contribution to the Lamb shift (given by $L_{n,l,j}$ in Equation (9.3)), which separates the states $2\,s_{1/s}$ and $2\,p_{1/2}$. Hence the hidden-photon effect does not die off in the limit $m_X \to 0$, and neither does the constraint (the green curve). However the only physically important thing is the high-mass hidden-photon behaviour, so this is not a serious issue.

E Theoretical uncertainty for $2\,s_{1/2}-2\,p_{1/2}$ in true muonium

No proper theoretical calculation for this transition has been done. This section produces a rough estimate for the theoretical uncertainty of this transition.

The leading-order contribution to the Lamb shift is proportional to the mass of the orbiting particle m_o. Therefore an approximate value of this transition is obtained by scaling the atomic-hydrogen value up by a factor $\sim m_\mu/m_e$ to get ~ 1 GHz.

The dominant contribution to the uncertainty in the atomic hydrogen case comes from finite-nuclear-size effects. These are absent in true muonium. A naïve estimate of the uncertainty in true muonium can therefore be obtained by subtracting the finite-nuclear-size contribution from the atomic hydrogen value (see for example [70]), and scaling it up by m_μ/m_e to get ~ 200 kHz.

However this naïve estimate is inadequate. The reduced mass of the system is now larger, so that hadronic and muonic vacuum-polarization contributions are now much more important. These effects must receive more careful treatment. To leading order [143]

$$E_{VP} \propto \left(\frac{m_o}{m_e}\right)^2 m_o\,. \tag{E.1}$$

The vacuum polarization contribution from atomic hydrogen must therefore be scaled up by a factor $(m_\mu/m_e)^3$, which causes a much larger contribution of $\sim$ 0.1 GHz. This can be taken as the theoretical uncertainty.

F Muonic-hydrogen anomaly

The recent measurement [64] of the $2\,s_{1/2}^{F=1} - 2\,p_{3/2}^{F=2}$ Lamb shift in muonic hydrogen deviates by more than $5\,\sigma$ from theoretical calculations combined with atomic-spectral measurements of the proton radius.

It is tempting to speculate that this deviation is due to a hidden photon [144]. This chapter briefly investigates if such an interpretation is possible.

The first observation is that the addition of the hidden photon increases the binding energy of the s-state compared to the p-state. This makes the Lamb-shift in muonic hydrogen more negative, in line with the observed effect.

This motivates a fit using the Lamb shift in ordinary and muonic hydrogen to fit the proton radius and the kinetic-mixing parameter of the hidden photon. The strategy as outlined in Chapter 9.1.2 can be used, just including the proton radius as an additional parameter. The transitions involved are Lamb shifts (that is transitions between states with the same principal quantum number n), so changes in α are a subdominant effect (see Chapter 9.1.3). Therefore α can be treated as a constant.

The hidden-photon contribution to the Lamb shift is already given in Equation (9.9). The muonic-hydrogen contribution is given by the replacement $m_e \to m_\mu$. The leading-order dependence of the Lamb shift on the proton radius is given in Equation (9.7).

Unfortunately the required values for χ^2 are smaller than zero and since χ is a real parameter this rules out a hidden-photon explanation. The reason for this is quite simple. From Equations (9.7) and (9.9) it can be seen that, from the perspective of the ($n = 2$) Lamb shifts, a modification Δr_p^2 is equivalent to a non-vanishing χ^2 for

$$\Delta r_p^2 = -6\chi^2 \frac{a_o^4\, m_X^2}{(1 + a_o\, m_X)^4}\,, \tag{F.1}$$

where $a_o = 1/(\alpha m_o)$ is the Bohr radius of the orbiting particle. This means that a non-vanishing $\chi^2 > 0$ effectively means measuring a smaller proton radius in the Lamb-shift measurement. Both the ordinary-hydrogen and the muonic-hydrogen measurements are affected in the same direction. It can easily be checked that the effect is actually always bigger for larger a_o. In other words if there is a non-vanishing $\chi^2 > 0$ then the observed proton radius in the Lamb

shift of ordinary hydrogen should be even smaller than the one observed in muonic hydrogen. This is exactly the opposite of what is observed in [64].

It is also possible to form a constraint using the same two measurements, independent of electron-scattering determinations of the proton radius. However the two measurements are not consistent with each other, so the uncertainty must be inflated similar to Equation (9.6). M_1 is taken as the $2\,s_{1/2} - 2\,p_{1/2}$ Lamb shift in atomic hydrogen. There is an experimental uncertainty of 3 kHz [67] and theoretical uncertainty of 6 kHz [68], leading to $\delta M_1 = 3 \times 10^{-11}$ eV and $\widetilde{\Delta M_1} = 10^{-10}$ eV. The δM_i are calculated using the CODATA [62] mean value for the proton radius of $r_p = 0.8768$ fm. M_2 is taken as the $2\,s_{1/2}^{F=1} - 2\,p_{3/2}^{F=2}$ Lamb shift in muonic hydrogen. Using the experimental and theoretical values from Chapter 9.1.4 gives $\delta M_2 = -3.11 \times 10^{-4}$ eV and $\widetilde{\Delta M_2} = 6 \times 10^{-4}$ eV. The corresponding constraint is shown as the solid-blue curve in Figure 8.

G Fixed-target derivations

G.1 Cross section for fixed-target experiments

It is necessary to solve for the minimum momentum transfer $t_{r,min} = -q^2_{min}$, and the maximum transfer $t_{r,max} = -q^2_{max}$.

First four-momentum conservation is applied $P_f = P_i + (p - p' - l) = P_i - q$ (see Figure 13 a).), where the metric $(+,-,-,-)$ is used,

$$\begin{aligned} & P_f^2 = M_i^2 = M_i^2 + q^2 - 2\,M_i q^0\,, \\ & \rightarrow -2\,M_i q^0 + q_0^2 - |\vec{q}|^2 = 0 \\ & \rightarrow q^0 = M_i \pm \sqrt{M_i^2 + |\vec{q}|^2}\,. \end{aligned} \tag{G.1}$$

In bremsstrahlung the target nucleus is assumed to be much heavier than other energy/mass scales in the problem, so $M_i^2 \gg |\vec{q}|^2$. Hence

$$q^0 \sim -\frac{1}{2}\frac{|\vec{q}|^2}{M_i^2} \sim 0\,. \tag{G.2}$$

A second application of four-momentum conservation can be made by using the Weizsäcker-Williams approximation (see Figure 13 b)), $p' = (q + p - l)$. Hence

$$m_e^2 = q^2 + (p-l)^2 + 2q\cdot(p-l)\,. \tag{G.3}$$

It is necessary to solve for the three terms on the right hand side of this equation.

For the first term Equation (G.2) is used to get

$$q^2 \sim -|\vec{q}|^2\,. \tag{G.4}$$

The second term is given by

$$(p-l)^2 = m_e^2 + m_X^2 - 2p\cdot l\,, \tag{G.5}$$

where

$$p\cdot l = xE_0^2 - |\vec{p}||\vec{l}|\cos\theta_X\,. \tag{G.6}$$

The energies involved are much larger than the masses, so the following approximations apply,

$$\begin{aligned} |\vec{p}| &= \sqrt{E_0^2 - m_e^2} \sim E_0\left(1 - \frac{1}{2}\frac{m_e^2}{E_0^2}\right)\,, \\ |\vec{l}| &= \sqrt{x^2E_0^2 - m_X^2} \sim xE_0\left(1 - \frac{1}{2}\frac{m_X^2}{x^2E_0^2}\right)\,. \end{aligned} \tag{G.7}$$

Substituting these into Equation (G.6) and using small-angle approximation[22] for θ_X

$$p \cdot l \sim \frac{x\, E_0^2\, \theta_X^2}{2} + \frac{1}{2} x\, m_e^2 + \frac{1}{2} \frac{m_X^2}{x} \,. \tag{G.8}$$

The third term in Equation (G.3) can be approximated by using Equation (G.2),[23]

$$2q \cdot (p - l) \sim -2|\vec{q}||(\vec{p} - \vec{l})| \cos\theta_{qpl} \,. \tag{G.9}$$

$|(\vec{p} - \vec{l})|$ is calculated by considering the invariant

$$\begin{aligned} (p-l)^2 &= ((1-x)E_0)^2 - |\vec{p} - \vec{l}|^2 = m_e^2 + m_X^2 - 2(p \cdot l) \\ &\sim m_e^2 + m_X^2 - xE_0^2\theta_X^2 - xm_e^2 - \frac{m_X^2}{x} \,, \end{aligned} \tag{G.10}$$

where Equation (G.8) has been used. Using m_e, $m_X \ll E_0$, and the small-angle approximation for θ_X, it is possible to neglect all terms on the right hand side of Equation (G.10) to get

$$|\vec{p} - \vec{l}| \sim (1-x)E_0 \,. \tag{G.11}$$

Substituting Equations (G.4), (G.8), (G.9), and (G.11) into Equation (G.3),

$$m_e^2 = -|\vec{q}|^2 + m_e^2 + m_X^2 - xE_0^2\theta_X^2 - xm_e^2 - \frac{m_X^2}{x} - 2|\vec{q}|(1-x)E_0 \cos\theta_{qpl} \,. \tag{G.12}$$

There are two terms in Equation (G.12) which involve $|\vec{q}|$; one quadratic in $|\vec{q}|$, and one linear. A lower bound on $|\vec{q}|$ can be obtained by observing what happens when $|\vec{q}|$ becomes small. This happens when the quadratic term in Equation (G.12) becomes negligible in comparison with the linear term, that is

$$|\vec{q}| \ll 2\,(1-x)E_0 \,, \tag{G.13}$$

which holds for all $\cos\theta_{qpl}$. Hence

$$|\vec{q}| \sim \frac{U}{2(1-x)E_0 \cos\theta_{qpl}} \,, \tag{G.14}$$

where

$$U(x, \theta_X) = xE_0^2\theta_X^2 + m_X^2 \frac{(1-x)}{x} + xm_e^2 \,. \tag{G.15}$$

[22] It will soon be shows that the small-angle approximation is valid, and that the whole procedure is self consistent.

[23] Note that θ_{qpl} is *not* θ_X, but the angle between the three-momenta $\vec{q}$ and $(\vec{p} - \vec{l})$.

Equation (G.14) is clearly minimised when $\cos\theta_{qpl} = 1$. Hence

$$t_{r,min} = -q^2_{min} \sim |\vec{q}|^2_{min} \sim \left(\frac{U}{2E_0(1-x)}\right)^2 , \tag{G.16}$$

where Equation (G.2) has been used again. Equation (G.16) is used to calculate the cross section in Equation (11.3). It is further shown in [38, 95, 96] that $t_{r,max} \sim m_X^2$.

Equation (G.16) can be used to derive a cutoff value for $(1-x)$, which is denoted $(1-x_{c1})$. For $(1-x) \gtrsim (1-x_{c1})$ there is negligible production of hidden photons. Production shuts down below $t_{r,min}$, and this occurs when the approximation Equation (G.13) breaks down. Hence the infrared cutoff applies when $|\vec{q}| \sim (1-x)E_0$. Substituting this into Equation (G.16) gives

$$(1-x_{c1}) \sim \frac{m_X^2}{E_0^2} , \tag{G.17}$$

where the approximations $\theta_X \ll 1$, $m_e \ll m_X$, and $x \sim 1$ have been used.

Using the Weizsäcker-Williams approximation the differential cross section can now be written in the form [38, 95–97]

$$\frac{d\sigma}{dx\, d\cos\theta_X} = (8\alpha^3\chi^2 f\beta)\left[\frac{2-2x+x^2}{2U^2} + \frac{(1-x)^2 m_X^2}{U^4}\left(m_X^2 - \frac{Ux}{1-x}\right)\right] , \tag{G.18}$$

where $\beta = \sqrt{1-m_X^2/E_0^2}$, and f is the flux factor in Equation (11.4).

The factor $\cos\theta_X$ can be replaced using the small-angle approximation. Hence $d\cos\theta_X \sim (1/2)\, d\theta_X^2$. Then using the chain rule $d\theta_X^2 = (d\theta_X^2)/(dU)\, dU$, the Equation (G.18) can be integrated over U. The first term in Equation (G.18) then evaluates to

$$\sim \frac{1}{xE_0^2}\left[\frac{1}{U(x,\theta_X=0)} - \frac{1}{U(x,\theta=\theta_{cut})}\right] , \tag{G.19}$$

where θ_{cut} is the upper limit on the θ_X integration. It is not possible to naïvely take $\theta_{cut} = \pi$, since small-angle approximations for θ_X have been used. However it will soon be shown that $\theta_{cut} \lesssim 1$ provides the correct result, so this is not a significant issue.[24]

[24] A more mathematically-rigorous calculation could be done without making any small-angle approximations. However the physical result would be the same. However it would still be found that production is dominated at small angles, and that the last term in Equation (G.19) is negligible.

The function $U(x, \theta_X)$ in Equation (G.15) must be examined more carefully. The approximations $E_0 \gg m_X, m_e$ can be enforced, and apply at all points in constraints (see Figure 15), giving $U(x, \theta_X = \theta_{cut} \sim 1) \gg U(x, \theta_X = 0)$.[25] Hence the last term in Equation (G.19) can be dropped. Physically this means that the production of hidden photons happens almost entirely at $\theta_X = 0$. Therefore it can be assumed to a good approximation that produced hidden photons are colinear with the original electron beam. This will be confirmed later with an explicit calculation of θ_{cut}.

The inverse factor of $U(x, \theta_X = 0)$ in Equation (G.19) is important. It contains the infrared-divergence structure which provides the main contribution to the cross section.

The same method is used to integrate the remaining two terms in Equation (G.18). However the last stage uses the approximation

$$\frac{1}{U(x, \theta_X = 0)^n} \sim \frac{1}{U(x, \theta_X = 0)} \left(\frac{x}{(1-x)\, m_X^2} \right)^{(n-1)} . \tag{G.20}$$

This is valid since only one inverse power of $U(x, \theta_X = 0)$ is necessary to include the physically important infrared-divergence structure. For the remaining inverse factors of U the approximation $m_X \gg m_e$ can be used, which gives $U(x, \theta_X = 0) \sim m_X^2 (1-x)/x$.

Finally,

$$\frac{d\sigma}{dx} = (8\alpha^3 \chi^2 f \beta) \left(m_X^2 \frac{(1-x)}{x} + m_e^2 x \right)^{-1} \times \left(1 - x + \frac{x^2}{3} \right) , \tag{G.21}$$

where the factor $U(x, \theta_X = 0)^{-1} = \left(m_X^2 (1-x)/x + m_e^2 x \right)^{-1}$ contains the infrared divergence. Physically this divergence comes from of a soft final-state electron. That occurs when $x \sim 1$ and the hidden photon has taken almost all of energy from the original beam electron. Here the factor of m_X^2 in the denominator of Equation (G.21) becomes less important. The differential cross section is no longer suppressed by the large m_X^2 term, and this region provides the major contribution to the total cross section. This divergence happens when $m_X^2 (1 - x_{c2})/x_{c2} \sim m_e^2\, x_{c2}$, where x_{c2} is a second infrared cutoff. Solving this gives

$$(1 - x_{c2}) \sim \frac{m_e^2}{m_X^2} . \tag{G.22}$$

[25] Note that $\theta_{cut} = 1$ is the largest value allowed by the small-angle approximation.

Noting that $m_e \ll m_X \ll E_0$, the two infrared cutoffs (G.17) and (G.22) indicate that the deviation between x and 1 is small. This justifies the often applied approximation $x \sim 1$.

It is now possible to derive an explicit expression for θ_{cut}. From Equation (G.19) it can be seen that production shuts off for θ_{cut} such that $U(x, \theta_X = \theta_{cut}) \sim U(x, \theta_X = 0)$. For larger angles the inverse U term dies off and does not contribute. Solving this condition gives

$$\theta_{X,\,\mathrm{cut}} \sim \frac{m_X}{E_0}\sqrt{\frac{1-x}{x}}\,. \tag{G.23}$$

The typical median value of $(1-x)$ is given by

$$\overline{(1-x)} = \sqrt{\max\left((1-x_{c1}),(1-x_{c2})\right)} = \max\left(m_X/E_0,\, m_e/m_X\right). \tag{G.24}$$

Therefore overall,

$$\theta_{X,\,\mathrm{cut},\,\mathrm{max}} \sim \max\left(\frac{\sqrt{m_X m_e}}{E_0}, \left(\frac{m_X}{E_0}\right)^{\frac{3}{2}}\right). \tag{G.25}$$

In Appendix G.2 it will be shown that the characteristic angle of the decay products with respect to hidden photon is $\sim m_X/(xE_0) \sim m_X/E_0$ (the full expression is given by Equation (G.28)), where the approximation $x \sim 1$ has again been used.

It is now possible to prove that, in the non-KK model, the hidden-photon angle is always negligible. Using $m_e \ll m_X \ll E_0$ and Equation (G.25) it can be seen that the angle of the hidden photon with respect to the electron beam is parametrically smaller than the angle of the decay products with respect to the hidden photon ($\sim m_X/E_0$). This confirms that a colinear hidden photon can be assumed to a good approximation.

The KK model is slightly more complicated. From Equation (G.25) the first possible value of $\theta_{X,\mathrm{cut},\mathrm{max}} \sim \sqrt{m_k m_e}/E_0 \leq \sqrt{m_e/E_0} \ll 1$, so the small-angle approximation is still valid. However the second value $\sim (m_k/E_0)^{3/2}$ becomes $O(1)$ for the highest mass KK modes. Hence the small-angle approximation for the hidden-photon angle breaks down. However this angle is still $\leq$ the angle of the decay products $\sim m_k/E_0$, so the total angle of the decay products is modified by a factor ≤ 2. Hence there is little modification to the kinematic cuts in Appendix G.2.

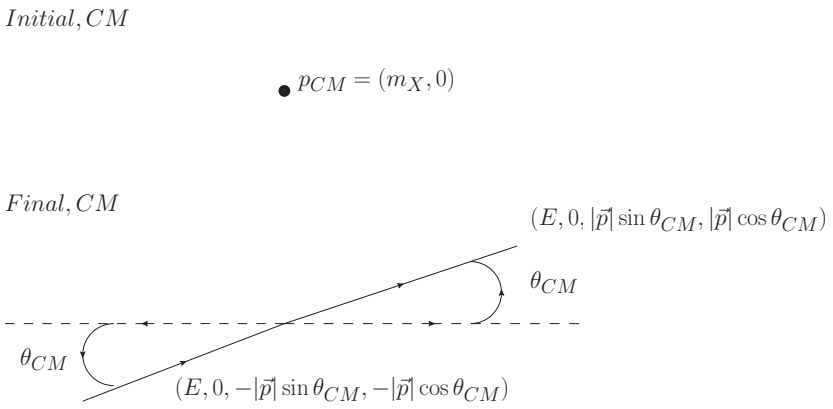

Figure 43: Geometry of $X \to e^+ + e^-$ decay in the CM frame.

G.2 Kinematic cuts for fixed-target experiments

It is necessary to derive expressions for the energies and angles of the e^+e^- pair in the lab frame.

The motion is initially analysed in the centre-of-mass (CM) frame. The initial four-momentum of the hidden photon is $p_{CM,X} = (m_X, 0)$.

Without loss of generality the initial-beam electron can be taken to be moving along the z-axis. Hence all initial motion is symmetric about the z-axis. The small hidden-photon angle with respect to the z-axis can be neglected. Hence the final-state decays also exhibit this symmetry. Therefore it can be assumed without loss of generality that the decay only happens in the $y - z$ plane. This situation is shown in Figure 43.

The products have four-momenta $p_{CM} = (E, 0, \pm|\vec{p}| \sin\theta_{CM}, \pm|\vec{p}| \cos\theta_{CM})$, with $E = m_X/2$. The products have identical mass so their energies and angles are the same, and the four-momenta can be swapped by sending $|\vec{p}| \longleftrightarrow -|\vec{p}|$.

The motion is now analysed in the lab frame. The lab frame moves in the z-direction with a velocity $v = -\sqrt{1 - \gamma^{-2}}$ with respect to the CM frame, where $\gamma = (xE_0)/m_X$. Hence the Lorentz transformation is given by

$$\Lambda(v) = \begin{pmatrix} \gamma & 0 & 0 & v\gamma \\ 0 & 1 & 0 & 0 \\ 0 & 0 & 1 & 0 \\ v\gamma & 0 & 0 & \gamma \end{pmatrix}. \tag{G.26}$$

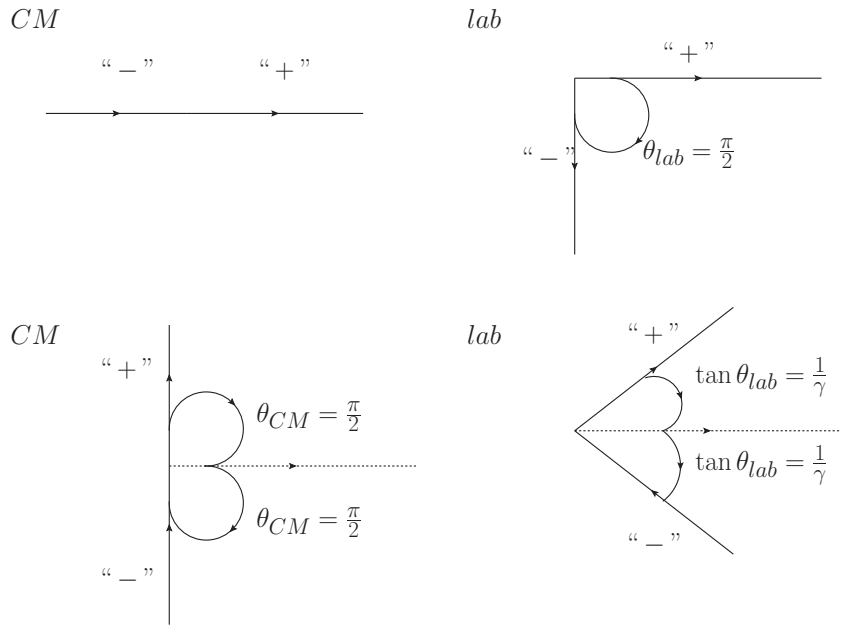

Figure 44: Range of angles for the e^+e^- pair in the E137 and E774 fixed-target experiments.

Applying this Lorentz transformation to the four-momenta gives $E_{lab} = \gamma(E \pm v|\vec{p}|\cos\theta_{CM})$. Using the approximation $m_e \ll m_X$ gives $|\vec{p}| \sim E = m_X/2$. Further $\gamma = (xE_0)/m \gg 1 \rightarrow v \sim 1$. Hence

$$E_{lab} \sim \frac{xE_0}{2}(1 \pm \cos\theta_{CM})\,. \tag{G.27}$$

Applying the same approximations as above,

$$\tan\theta_{lab} = \frac{p_y}{p_z} = \pm\frac{1}{\gamma}\sqrt{\frac{1 \mp \cos\theta_{CM}}{1 \pm \cos\theta_{CM}}}\,. \tag{G.28}$$

It is now possible to apply the necessary energy and momentum cuts. These must be tailored to the individual experiments.

The strongest constraint is from E137 at SLAC [98]. This involves sending $\sim 2{\times}10^{21}$ electrons with an initial-beam energy of $E_0 = 20$ GeV at an aluminium ($Z = 13$, $A = 27$) target. The target is of multiple radiation lengths (as with all of the considered experiments), but the shielded region in this case is a hill of length $l \sim 200$ metres.[26] This is followed by a vacuum region ~ 200 metres.

[26]Note that it is not really important to distinguish between the actually target and shielded

This gives the distance from the target to the detector as $L \sim 400$ metres. This is followed by a detector with radius $r = 3$ metres. No candidate events are observed, and the constraint is formed by assuming a background of ~ 10 events.

Here the detector is an electromagnetic shower counter. This can detect electrons, positrons, or photons. As explained in Chapter 11.1 the production of SM photons is negligible, so the detected signal consists of electrons and positrons.

The kinematics of these particles can now be considered. Note that in the electromagnetic shower counter there is a symmetry between the electron and positron particles, as both of these particles can be detected. Hence the "+" in Equations (G.27) and (G.28) is just a dummy label which can apply to either the electron or positron. In particular note that "+" does not necessarily mean positron, and the "-" does not necessarily mean electron.

In region $0 \leq \theta_{CM} \leq \pi/2$ the "+" travels in the positive z direction in the CM frame. The region $\pi/2 \leq \theta_{CM} \leq \pi$ is simply where the "+" particle travels backwards in the CM frame and the "-" travels forward in the CM frame. Hence the (dummy) labels "+" and "-" have simply been swapped, but the physical situation is the same. Therefore it is possible to analyse the whole decay by just considering the region $0 \leq \theta_{CM} \leq \pi/2$.

It is not necessary to consider negative θ_{CM}, since energies and angles of decay are dependent on $\cos\theta_{CM}$, which is symmetric in θ_{CM}. This is of course because the decay is, to a good approximation, symmetric about the z-axis.

The range of possible angles of particles in the lab and CM frames should briefly be noted.

- $\theta_{CM} \to 0$. In the CM frame the "+" particle is emitted directly forward and the "-" particle directly backwards. In the lab frame $\theta_{+,\,lab} \to 0$ and $\theta_{-,lab} \to \pi/2$. Hence the "+" particle is emitted directly forwards in the

region. All considered experiments use thick targets (of multiple radiation length), so most production happens in the first radiation length. Therefore the the rest of the target acts like a shield. Hence the important quantity is the total length of the target plus the shielded region, which is denoted "l". If the hidden-photon decays in this region then it can not be detected.

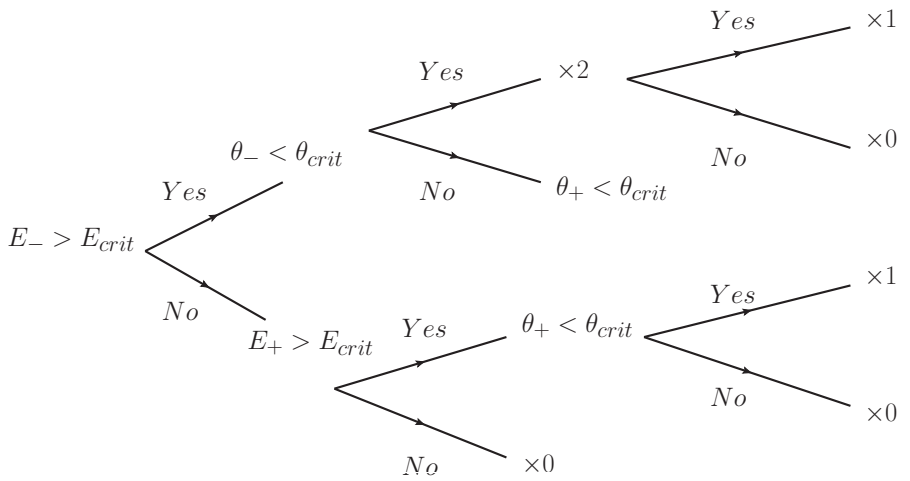

Figure 45: Decision tree for the kinematic cuts for the E137 and E774 fixed-target experiments.

lab frame and the "-" particle is emitted at a right angle.

- $\theta_{CM} \to \pi/2$. In the CM frame the "+" and "-" particles are both emitted at right angles. In the lab frame the particles are both emitted at angles with equal magnitudes, which are less than $\pi/2$.

This is demonstrated in Figure 44. It can be seen that in the lab frame no particles are emitted backwards, and in fact are emitted at worst at right angles. Hence only the magnitude, but not the direction, of the emitted particles must be considered.

Equation (G.28) shows that, in the region $0 \leq \theta_{CM} \leq \pi/2$, the "+" particle always has an angle with magnitude less than or equal to that of the "-" particle. Hence if the "-" particle has an acceptable angle, then the "+" particle does so automatically. Furthermore Equation (G.27) shows that $E_+ \geq E_-$. Hence if the "-" particle has a high enough energy to be detected, the "+" particle does so automatically.

$E_{crit} = 0.1 \times E_0$ as the minimum energy for a detected particle. Also $\tan(\theta_{crit}) = r/(L-z)$, where r is the radius of the detector. This is the angle of acceptance for a hidden photon which decays at a given z. The kinematic cuts are then applied via the decision tree in Figure 45.

In the CM frame the decay is symmetric in θ_{CM}. Hence angles are distributed with a uniform probability distribution. The probability of a given decay lying in the angular region $\theta_{CM} \to \theta_{CM} + d\theta_{CM}$ is therefore equal to $\frac{1}{(\pi/2)} d\theta_{CM}$. Equation (11.7) is multiplied by this factor.

Finally Equation (11.7) is integrated over $0 \leq \theta_{CM} \leq \pi/2$, $0 \leq x \leq 1$, and $l \leq z \leq L$ to get the black curve in Figure 15. Constraints are only obtained for $m_X > 2\,m_e$, for which the decay $X \to e^+ + e^-$ is energetically possible.

The next fixed-target experiment is E774 at SLAC [99]. This uses 0.52×10^{10} electrons with $E_0 = 275$ GeV, and a tungsten ($Z = 74$, $A = 184$) target. The target-plus-shielding length is $l \sim 0.3$ metres, the target-detector distance is $L \sim 7.55$ metres, and the detector radius is $r \sim 0.3$ metres. The background is ~ 17 events.

The detector is again a general electromagnetic calorimeter, meaning that either a positron or electron can be detected, as long as it has energy $\geq E_{crit} = 0.1\,E_0 = 27.5$ GeV. Again it is found that SM-photon events are negligible. Because the final detection method here is the same as in the E137, it is possible to apply the same decision tree for kinematic cuts (Figure 45), with the new values of E_{crit} and θ_{crit}. The final constraint is shown as the blue curve in Figure 15.

The final fixed-target experiment is E141 at SLAC [100]. Here 2×10^{15} electrons with $E_0 = 9$ GeV are fired at a tungsten ($X = 74$, $A = 184$) target. The target-plus-shielding length is $l \sim 0.22$ metres, the target-detector distance is $L \sim 35$ metres, and the detector radius is $r \sim 0.075$ metres. The background is ~ 1000 events.

Here the kinematic cuts are slightly different and much simpler. This is because the only detected final state is the positron. The detection symmetry between the electron and positron is therefore broken. The label "+" is now attached just to just the positron, and the label "-" to the electron. It is now necessary to account for the whole region $0 \leq \theta_{CM} \leq \pi$, as the regions $0 \leq \theta_{CM}$ and $\pi/2 \leq \theta_{CM} \leq \pi$ are not physically equivalent. The latter region is where the positron travels backwards in the CM frame. However there is still symmetry about the z-axis, so negative values of θ_{CM} do not need to be taken into account. The cuts impose that the hidden photon only gives a non-

zero contribution for $\theta_{+,\,lab} \leq \theta_{crit}$. Furthermore it is imposed that the hidden photon only gives a non-zero contribution for $E_{+,\,lab} \geq E_{crit} = 0.5\,E_0$, as these are the only experimentally-detected energies.

Finally Equation (11.7) is multiplied by the probability element $(1/\pi)\,d\theta_{CM}$ and integrated over the range $0 \leq \theta_{CM} \leq \pi$, $0 < x < 1$ and $l \leq z \leq L$ to get the final constraint. This is shown as the red curve in Figure 15.

References

[1] N. Arkani-Hamed, S. Dimopoulos, and G. R. Dvali, Phys. Lett. **B429**, 263 (1998), arXiv:hep-ph/9803315.

[2] N. Arkani-Hamed, S. Dimopoulos, and G. Dvali, Phys.Rev. **D59**, 086004 (1999), arXiv:hep-ph/9807344.

[3] J. Redondo and M. Postma, Journal of Cosmology and Astroparticle Physics **2009**, 005 (2009).

[4] M. Pospelov, Phys. Rev. **D80**, 095002 (2009), arXiv:0811.1030.

[5] J. Redondo, private communication.

[6] J. Jaeckel and A. Ringwald, Annual Review of Nuclear and Particle Science **60**, 405 (2010), arXiv:1002.0329.

[7] S. G. Karshenboim, Phys. Rev. Lett. **104**, 220406 (2010), arXiv:1005.4859.

[8] S. G. Karshenboim, Phys. Rev. D **82**, 073003 (2010), arXiv:1005.4872.

[9] R. D. Peccei and H. R. Quinn, Phys. Rev. Lett. **38**, 1440 (1977).

[10] B. Holdom, Phys. Lett. **57** (1986).

[11] F. Brummer, J. Jaeckel, and V. V. Khoze, JHEP **0906**, 037 (2009), arXiv:0905.0633.

[12] B. Batell and T. Gherghetta, Phys.Rev. **D73**, 045016 (2006), arXiv:hep-ph/0512356.

[13] M. Gluck, S. Rakshit, and E. Reya, Phys. Rev. **D76**, 091701 (2007), arXiv:hep-ph/0703140.

[14] M. S. Turner, Phys. Rev. Lett. **60**, 1797 (1988).

[15] L.B.Okun, Sov. Phys **56**, 502 (1982).

[16] B. Holdom, Physics Letters B **166**, 196 (1986).

[17] K. R. Dienes, C. Kolda, and J. March-Russell, Nuclear Physics B **492**, 104 (1997).

[18] S. A. Abel, M. D. Goodsell, J. Jaeckel, V. V. Khoze, and A. Ringwald, JHEP **07**, 124 (2008), arXiv:0803.1449.

[19] M. Goodsell, J. Jaeckel, J. Redondo, and A. Ringwald, JHEP **11**, 027 (2009), arXiv:0909.0515.

[20] A. Mirizzi, J. Redondo, and G. Sigl, JCAP **0903**, 026 (2009), arXiv:0901.0014.

[21] G. Ruoso *et al.*, Zeitschrift fr Physik C Particles and Fields **56**, 505 (1992), 10.1007/BF01474722.

[22] R. Cameron *et al.*, Phys.Rev. **D47**, 3707 (1993).

[23] M. Ahlers, H. Gies, J. Jaeckel, J. Redondo, and A. Ringwald, Phys.Rev. **D76**, 115005 (2007), arXiv:0706.2836.

[24] GammeV (T-969) Collaboration, A. S. Chou *et al.*, Phys.Rev.Lett. **100**, 080402 (2008), arXiv:0710.3783.

[25] A. Afanasev *et al.*, Phys.Rev.Lett. **101**, 120401 (2008), arXiv:0806.2631.

[26] M. Fouche *et al.*, Phys.Rev. **D78**, 032013 (2008), arXiv:0808.2800.

[27] ALPS collaboration, K. Ehret *et al.*, Nucl.Instrum.Meth. **A612**, 83 (2009), arXiv:0905.4159.

[28] A. S. Goldhaber and M. M. Nieto, Rev. Mod. Phys. **82**, 939 (2010).

[29] J. Redondo, p. 23 (2008), arXiv:0810.3200.

[30] J. Jaeckel, J. Redondo, and A. Ringwald, Phys. Rev. Lett. **101**, 131801 (2008), arXiv:0804.4157.

[31] V. Simha and G. Steigman, JCAP **0806**, 016 (2008), arXiv:0803.3465, * Brief entry *.

[32] J. Jaeckel, Phys. Rev. Lett. **103**, 080402 (2009), arXiv:0904.1547.

[33] J. A. Frieman, S. Dimopoulos, and M. S. Turner, Phys. Rev. D **36**, 2201 (1987).

[34] G. G. Raffelt and D. S. P. Dearborn, Phys. Rev. D **37**, 549 (1988).

[35] J. Redondo, JCAP **0807**, 008 (2008), arXiv:0801.1527.

[36] V. Popov, Tr. J. of Physics **23**, 943 (1999).

[37] E. W. Kolb and R. J. Scherrer, Phys. Rev. D **25**, 1481 (1982).

[38] J. D. Bjorken, R. Essig, P. Schuster, and N. Toro, Phys. Rev. **D80**, 075018 (2009), arXiv:0906.0580.

[39] A. Konaka *et al.*, Phys. Rev. Lett. **57**, 659 (1986).

[40] S. Andreas, C. Niebuhr, and A. Ringwald, (2012), arXiv:1209.6083.

[41] M. Davier and H. N. Ngoc, Physics Letters B **229**, 150 .

[42] BABAR Collaboration, B. Aubert *et al.*, (2009), arXiv:0902.2176, 17 pages, 11 postscript figures, submitted to Aspen-2009.

[43] S. Giovannella and the Kloe-2 Collaboration, Journal of Physics: Conference Series **335**, 012067 (2011).

[44] D. Feldman, Z. Liu, and P. Nath, Phys.Rev.Lett. **97**, 021801 (2006), arXiv:hep-ph/0603039.

[45] E. Adelberger, B. R. Heckel, and A. Nelson, Ann.Rev.Nucl.Part.Sci. **53**, 77 (2003), arXiv:hep-ph/0307284.

[46] C. D. Hoyle *et al.*, Phys. Rev. **D70**, 042004 (2004), arXiv:hep-ph/0405262.

[47] M. Pospelov, A. Ritz, and M. B. Voloshin, Phys. Lett. **B662**, 53 (2008), arXiv:0711.4866.

[48] N. Arkani-Hamed, D. P. Finkbeiner, T. R. Slatyer, and N. Weiner, Phys. Rev. **D79**, 015014 (2009), arXiv:0810.0713.

[49] A. Ibarra, A. Ringwald, and C. Weniger, JCAP **0901**, 003 (2009), arXiv:0809.3196.

[50] J. Hamann, S. Hannestad, G. G. Raffelt, and Y. Y. Y. Wong, JCAP **0708**, 021 (2007), arXiv:0705.0440.

[51] J. Redondo, (2008), arXiv:0805.3112.

[52] J. Polchinski, Phys. Rev. Lett. **75**, 4724 (1995), arXiv:hep-th/9510017.

[53] L. Randall and R. Sundrum, Phys. Rev. Lett. **83**, 3370 (1999).

[54] L. Randall and R. Sundrum, Phys. Rev. Lett. **83**, 4690 (1999).

[55] K. L. McDonald and D. E. Morrissey, JHEP **1102**, 087 (2011), arXiv:1010.5999.

[56] A. Ferapontov, (2011), arXiv:1109.1187.

[57] The Torus and Supertoroid, http://paulbourke.net/geometry/torus/.

[58] G. D. Kribs, p. 633 (2006), arXiv:hep-ph/0605325.

[59] H.-C. Cheng, (2010), arXiv:1003.1162.

[60] R. Maldonado, private communication.

[61] T. Han, J. D. Lykken, and R.-J. Zhang, Phys.Rev. **D59**, 105006 (1999), arXiv:hep-ph/9811350.

[62] P. J. Mohr, B. N. Taylor, and D. B. Newell, Codata recommended values of the fundamental physical constants: 2006, 2007.

[63] A. van Wijngaarden, J. Kwela, and G. W. F. Drake, Phys. Rev. A **43**, 3325 (1991).

[64] R. Pohl *et al.*, Nature **466**, 213 (2010).

[65] P. G. Blunden and I. Sick, Phys. Rev. C **72**, 057601 (2005).

[66] M. I. Eides, H. Grotch, and V. A. Shelyuto, Phys. Rept. **342**, 63 (2001), arXiv:hep-ph/0002158.

[67] C. Schwob *et al.*, Phys. Rev. Lett. **82**, 4960 (1999).

[68] G. G. Simon, C. Schmitt, F. Borkowski, and V. H. Walther, Nucl. Phys. **A333**, 381 (1980).

[69] M. Fischer *et al.*, Phys. Rev. Lett. **92**, 230802 (2004).

[70] F. Biraben, The European Physics Journal - Special Topics **172**, 109 (2009), arXiv:0809.2985v1.

[71] B. de Beauvoir *et al.*, Phys. Rev. Lett. **78**, 440 (1997).

[72] D. Mueller *et al.*, EPL (Europhysics Letters) **5**, 503 (1988).

[73] W. R. Johnson and G. Soff, Atomic Data and Nuclear Data Tables **33**, 405 (1985).

[74] K. P. Jungmann, (2004), arXiv:nucl-ex/0404013.

[75] D. Hagena *et al.*, Phys. Rev. Lett. **71**, 2887 (1993).

[76] R. Ley *et al.*, Hyperfine Interactions **89**, 327 (1994), 10.1007/BF02064517.

[77] R. Ley, Applied Surface Science **194**, 301 (2002).

[78] K. Jungmann, Hyperfine Interactions **127**, 189 (1999).

[79] S. J. Brodsky and R. F. Lebed, Phys. Rev. Lett. **102**, 213401 (2009), arXiv:0904.2225.

[80] K. Pachucki, Phys. Rev. A **53**, 2092 (1996).

[81] K. Pachucki, Phys. Rev. A **60**, 3593 (1999).

[82] E. Borie, Phys. Rev. A **71**, 032508 (2005).

[83] A. P. Martynenko, Phys. Rev. A **71**, 022506 (2005).

[84] A. P. Martynenko, Physics of Atomic Nuclei **71**, 125 (2008).

[85] J. Marton, Nuclear Physics A **790**, 328c (2007), Few-Body Problems in Physics - FB 18, 18th International IUPAP Conference on Few-Body Problems in Physics.

[86] W.-M. Yao *et al.*, Journal of Physics G **33**, 1+ (2006).

[87] M. A. et. al., Hyperfine Interactions **118**, 59 (1999).

[88] Muon (g-2) Collaboration, G. W. Bennett *et al.*, Phys. Rev. D **73**, 072003 (2006).

[89] K. Hagiwara, A. D. Martin, D. Nomura, and T. Teubner, Phys. Lett. **B649**, 173 (2007), arXiv:hep-ph/0611102.

[90] M. Endo, K. Hamaguchi, and G. Mishima, (2012), arXiv:1209.2558.

[91] M. E. Peskin and D. V. Schroeder, *An Introduction To Quantum Field Theory (Frontiers in Physics)* (Westview Press, 1995).

[92] D. Hanneke, S. Fogwell, and G. Gabrielse, Physical Review Letters **100**, 120801 (2008), arXiv:0801.1134.

[93] T. Aoyama, M. Hayakawa, T. Kinoshita, and M. Nio, Phys. Rev. **D77**, 053012 (2008), arXiv:0712.2607.

[94] T. Aoyama, M. Hayakawa, T. Kinoshita, and M. Nio, Phys.Rev.Lett. **109**, 111807 (2012), arXiv:1205.5368.

[95] K. J. Kim and Y.-S. Tsai, Phys. Rev. D **8**, 3109 (1973).

[96] Y.-S. Tsai, Rev. Mod. Phys. **46**, 815 (1974).

[97] Y. S. Tsai, Phys. Rev. D **34**, 1326 (1986).

[98] J. D. Bjorken *et al.*, Phys. Rev. D **38**, 3375 (1988).

[99] A. Bross *et al.*, Phys. Rev. Lett. **67**, 2942 (1991).

[100] E. M. Riordan *et al.*, Phys. Rev. Lett. **59**, 755 (1987).

[101] Particle Data Group, C. Amsler *et al.*, Phys.Lett. **B667**, 1 (2008).

[102] D. A. Dicus, E. W. Kolb, H. J. Lubatti, and V. L. Teplitz, Phys. Rev. D **19**, 1522 (1979).

[103] J. N. Bahcall, A. M. Serenelli, and S. Basu, Astrophys.J. **621**, L85 (2005), arXiv:astro-ph/0412440.

[104] G. G. Raffelt and G. D. Starkman, Phys. Rev. D **40**, 942 (1989).

[105] D. Dearborn, G. Raffelt, P. Salati, J. Silk, and A. Bouquet, **354**, 568 (1990).

[106] V. V. Popov and O. V. Vasil'ev, EPL (Europhysics Letters) **15**, 7 (1991).

[107] E. Braaten and D. Segel, Phys.Rev. **D48**, 1478 (1993), arXiv:hep-ph/9302213.

[108] T. Altherr, E. Petitgirard, and T. R. Gaztelurrutia, Astroparticle Physics **1**, 289 (1993).

[109] G. G. Raffelt, *Stars as Laboratories for Fundamental Physics: The Astrophysics of Neutrinos, Axions, and Other Weakly Interacting Particles* (Chicago Univ. Press, Chicago, IL, 1996).

[110] H. A. Weldon, Phys. Rev. D **28**, 2007 (1983).

[111] E. Braaten, **392**, 70 (1992).

[112] P. J. Brussaard and H. C. van de Hulst, Rev. Mod. Phys. **34**, 507 (1962).

[113] CAST Collaboration, S. Andriamonje *et al.*, JCAP **0704**, 010 (2007), arXiv:hep-ex/0702006.

[114] P. Sikivie, Phys. Rev. Lett. **51**, 1415 (1983).

[115] K. van Bibber, P. M. McIntyre, D. E. Morris, and G. G. Raffelt, Phys. Rev. D **39**, 2089 (1989).

[116] CAST Collaboration, K. Zioutas *et al.*, Phys. Rev. Lett. **94**, 121301 (2005).

[117] J. Redondo and M. Postma, JCAP **0902**, 005 (2009), arXiv:0811.0326.

[118] T. Altherr and U. Kraemmer, Astroparticle Physics **1**, 133 (1992).

[119] V. V. Klimov, Sov. J. Nucl. Phys. **33**, 934 (1981).

[120] H. A. Weldon, Phys. Rev. D **26**, 2789 (1982).

[121] E. Braaten, Phys. Rev. Lett. **66**, 1655 (1991).

[122] L. Landau and E. Lifshits, *The Classical Theory of Fields*, Course of Theoretical Physics No. v. 2 (Butterworth-Heinemann, 1975).

[123] P. Gondolo and G. Gelmini, Nuclear Physics B **360**, 145 (1991).

[124] T. S. Coleman and M. Roos, Phys.Rev. **D68**, 027702 (2003), arXiv:astro-ph/0304281.

[125] H. Yüksel and M. D. Kistler, Phys. Rev. D **78**, 023502 (2008).

[126] A. Burrows and J. M. Lattimer, **307**, 178 (1986).

[127] W. D. Arnett, **263**, L55 (1982).

[128] W. HILLEBRANDT, Annals of the New York Academy of Sciences **422**, 197 (1984).

[129] H. Bethe, G. Brown, J. Applegate, and J. Lattimer, Nuclear Physics A **324**, 487 (1979).

[130] J. Lattimer, C. Pethick, D. Ravenhall, and D. Lamb, Nuclear Physics A **432**, 646 (1985).

[131] K. Hirata *et al.*, Phys. Rev. Lett. **58**, 1490 (1987).

[132] R. M. Bionta *et al.*, Phys. Rev. Lett. **58**, 1494 (1987).

[133] J. B. Dent, F. Ferrer, and L. M. Krauss, (2012), arXiv:1201.2683.

[134] G. Raffelt and D. Seckel, Phys. Rev. Lett. **60**, 1793 (1988).

[135] N. Iwamoto, Phys. Rev. Lett. **53**, 1198 (1984).

[136] A. Pantziris and K. Kang, Phys. Rev. D **33**, 3509 (1986).

[137] R. Barbieri and R. N. Mohapatra, Phys. Rev. D **39**, 1229 (1989).

[138] K. E. Baier, V.N. and V. Fadin, Sov. J. Nucl. Phys. **31:3**, 364 (1980).

[139] J. van der Bij and E. N. Glover, Nucl.Phys. **B313**, 237 (1989).

[140] e. a. E.W.N.Glover, Proc. workshop on z physics at lep1, vol. 2, Geneva, 1989, CERN, CERN, Coordinated and supervised by G. Altarelli.

[141] E. W. N. Glover and A. G. Morgan, Zeitschrift fur Physik C Particles and Fields **60**, 175 (1993).

[142] Hyperphysics, http://hyperphysics.phy-astr.gsu.edu/hbase/hframe.html.

[143] J. L. Friar, J. Martorell, and D. W. L. Sprung, Phys. Rev. A **59**, 4061 (1999).

[144] A. Falkowski, RESONAANCES blog, http://resonaances.blogspot.com/.